Chem Soc Rev

Unique Physicochemical Properties of Two-dimensional Light Absorbers Facilitating Photocatalysis

Journal:	*Chemical Society Reviews*
Manuscript ID	CS-REV-05-2018-000396.R1
Article Type:	Review Article
Date Submitted by the Author:	12-Jul-2018
Complete List of Authors:	Wang, Lianzhou; ARC Centre of Excellence for Functional Nanomaterials, The University of Queensland Liu, Gang; Chinese Academy of Sciences, Institute of Metal Research Cheng, Hui-Ming; Institute of Metal Research, CAS, Advanced Carbon Divisioin, SYNL; Tsinghua-Berkeley Shenzhen Institute, Zhen, Chao; Chinese Academy of Sciences, Institute of Metal Research Kang , Yuyang ; Shenyang National Laboratory for Materials Science, Institute of Metal Research, Chinese Academy of Sciences, 72 Wenhua Road, Shenyang 110016, China

Unique Physicochemical Properties of Two-dimensional Light Absorbers Faciliating Photocatalysis

Gang Liu[†],[1,2] Chao Zhen[†],[1] Yuyang Kang,[1,2] Lianzhou Wang*,[3] Hui-Ming Cheng*[1,4]

[1] Shenyang National Laboratory for Materials Science, Institute of Metal Research, Chinese Academy of Sciences, 72 Wenhua Road, Shenyang 110016, China

[2] School of Materials Science and Engineering, University of Science and Technology of China, 72 Wenhua Road, Shenyang 110016, China

[3] Nanomaterials Centre, School of Chemical Engineering and AIBN, The University of Queensland, St Lucia, Brisbane, QLD 4072, Australia

[4] Tsinghua-Berkeley Shenzhen Institute, Tsinghua University, 1001 Xueyuan Road, Shenzhen 518055, China

[†]These authors were equal major contributors to this work.

E-mail: l.wang@uq.edu.au (LZW); cheng@imr.ac.cn (HMC)

Abstract

The emergence of two-dimensional (2D) materials with a large lateral size and extremely small thickness has significantly changed the development of many research areas by producing a variety of unusual physicochemical properties. Semiconductor photocatalysis is intrinsically controlled by the multiple interactions of light-matter, light absorber-cocatalyst and molecular/ionic-matter that can be highly dependent on the geometric features of the light absorber. In this review, we focus on the unique structures and unusual physicochemical properties of 2D semiconducting light absorbers and their roles in facilitating photocatalysis. In particular, we highlight structure-property relationships considering unique electronic structure, optical absorption, spatial separation of the charge carriers, structural advantages as a host of active guests, and the strain-modulated band structures of the 2D light absorbers. The representative progress of a number of 2D light absorbers with the structural/compositional features of nonporous, porous, heteroatoms/defects modification and manufactured hybrid structures for photocatalysis are discussed in details. We conclude with a discussion of some key challenges and future directions for the development of 2D photocatalysts for efficient solar energy conversion.

1. Introduction

The sustainable development of modern society inevitably requires increasing dependence on renewable energy supplies. Solar energy as the largest renewable energy source has been considered the ultimate solution to this need. Solar energy can be realized by many ways including solar-to-thermal, solar-to-electrical, solar-to-biomass, and solar-to-chemical conversions. Among them, solar-to-chemical conversion based on photocatalysis represents an amazing way to produce solar fuels or high-value chemicals by inducing important redox reactions at ambient temperature[1]. Solar-driven photocatalytic water splitting to produce hydrogen is considered the key reaction in closing the loop on carbon emission by providing clean feedstock hydrogen and has been pursued since the 1970s.[2] Over 10% solar-to-hydrogen (STH) energy conversion for solar-driven photocatalytic water splitting[3] is required to economically compete with the currently dominant industrial hydrogen production technology, namely steam reforming from hydrocarbons. As a result of long-term intensive research, photocatalytic overall water splitting has seen very encouraging progress including over 1% STH[4], an apparent quantum yield (AQY) record of 71% at 254 nm[5], and overall water splitting beyond 600 nm with the particulate photocatalysts[6]. All these achievements indicate a bright future for solar-driven water splitting, yet there is still a long way to go before reaching the goal of ~10% STH efficiency.

A typical photocatalyst for the solar generation of hydrogen usually consists of a light absorber and a co-catalyst, and sometimes an electron mediator or a passivation

layer in order to simultaneously meet requirements of all three basic steps (light absorption, separation and transport of photogenerated charge carriers, and catalysis) of photocatalysis[7]. The realization of the 10% STH by photocatalysis depends on both the availability of suitable materials as the building blocks of photocatalysts and the ability to integrate these materials. In the past four decades, a large number of light absorbers have been established by changing the compositions and crystal structures. An increasing number of co-catalysts, most of which are derived from electrocatalysts for the hydrogen evolution and oxygen evolution reactions, have substantially improved the catalysis reactions, in particular water splitting without apparent back reactions. Equally important, driven by the rapid development of nanoscience and nanotechnology, rational control of the photocatalyst components in terms of their size and morphology (shape), crystallinity, defect and dopant also provide flexible platforms to facilitate the integrations of the particles. Reducing the particle size of the bulk materials in one-direction leads to the formation of attractive 2D materials with a thickness of one atom or one unit cell[8-22], and these have been intensively explored in a large variety of research fields[12, 14, 23-32]. Besides the geometric features of large basal size and small thickness, 2D materials possess unique physicochemical properties in terms of electronic structure (for example, the transition from an indirect to a direct bandgap, and from metallic to semiconducting), optical absorption, carrier transport, sorption of molecules and ions, reactive sites, etc. These properties make 2D materials promising as the active components of solar-driven photocatalysis systems. To this end, many 2D materials in addition to graphene[11, 33-104] have already

been used to construct various photocatalysts and photoelectrodes that do significantly boost solar energy conversion efficiency and/or exhibit some distinct features.

To rationally construct high-efficiency photocatalytic conversion systems with 2D materials as building blocks, it is important to understand the underlying correlations between the physicochemical properties of "2D" light absorbing materials and the basic steps of photocatalysis by critically reviewing the state-of-the-art progresses in 2D based photocatalysts. To our knowledge, there is no such a comprehensive review focusing on this aspect, though some reviews have given excellent summaries of the progress in the synthesis of various 2D materials and their related photocatalytic performance[85, 105-117]. In this review, we will first present a brief introduction to the fundamentals of photocatalysis including principles, material challenges, and the motivations for pursuing 2D photocatalysts. Then, the unique properties of 2D materials as light absorbers will be summarized to demonstrate the advantages and drawbacks of using them as light absorbers for photocatalysis. Based on a deep understanding, representative progress in using 2D materials as the light absorbers of photocatalysts will be discussed and compared with their bulk counterparts. Finally, the concluding remarks will address the key challenges in the field and propose a developing map of 2D materials based photocatalysts for more efficient solar energy utilization.

2. Fundamental aspects of photocatalysis

2.1. General principles of photocatalysis

Many important reviews have summarized the general principles of photocatalysis

from different aspects,[118-123] so that we shall give only a very brief introduction in order to help readers readily understand the necessity of using the 2D materials in the construction of solar-driven photocatalysts.

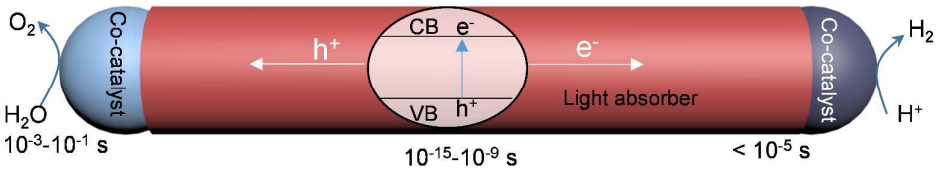

Figure 1. Schematic of photocatalytic water splitting occurring on a photocatalyst consisting of a light absorber and co-catalysts for the hydrogen and oxygen evolution reactions. Time scale of each step is also given.

Photocatalysis can be simply described as a process in which photo-generated electrons and holes induce targeted redox reactions on the light absorbers and/or co-catalysts loaded on it. Photocatalysis, consists of three distinct steps: 1) light absorption, 2) separation and transport of the photo-generated charge carriers in the bulk, and 3) catalysis on the surface of the light absorber and/or co-catalyst, as illustrated in **Figure 1**. How to realize this efficiently is very challenging, both thermodynamically and kinetically. The difficulties lie in at least the following aspects: 1) the maximum harvesting of solar energy (particularly visible light) to generate sufficient energetic electrons and holes; 2) a high mobility and long diffusion length of the photo-generated electrons and holes to suppress bulk recombination; 3) a sufficiently strong redox power of photo-generated electrons and holes to induce reactions, particularly water oxidation that requires four electrons; 4) abundant surface sites for the forward targeted reactions instead of the back reactions (like the

reaction between H_2 and O_2 to produce H_2O). Each of these four topics represents an important research direction. Moreover, the three steps span a huge time-scale from 10^{-15} to 10^{-1} s.

What's more challenging are the inherent conflicts between the requirements for three key steps. There are at least three factors involved here: 1) increasing the light absorption range (reduced bandgaps) normally leads to a lower reductive ability of the photo-generated electrons and/or a lower oxidation ability of the photo-generated holes;[124] 2) the much lower mobility of the holes than electrons in most semiconductors,[125] does not favor the rate-determining water oxidation reactions [126], 3) the mismatch between the random distributions of reductive and oxidative reaction sites and the desired migration of the electrons and holes in different directions[127].

The strong underlying conflicts associated with photophysical processes, electronic properties and catalysis principles make the realization of high-efficiency photocatalysis very challenging. To address the challenges, it is of critical importance to precisely control each basic step based on a comprehensive understanding of photocatalysis and structure-property relationship. In this review, we will highlight the important roles of "2D" structures as light absorbers on each step of the photocatalysis and hope to shed light on the rational design of better photocatalytic materials for improved solar energy conversion.

2.2. Challenges from the materials aspect and the advantages of 2D structures as light absorbers

As mentioned in the previous section, photocatalysis is an extremely complex process

involving multiple interactions of light with the material, adsorbate with the catalyst surface, and the photo-generated charge carriers with the adsorbate. Materials provide the platforms for manipulating these interactions by changing their compositions, crystal structures, particle size, morphology (shape), crystallinity, defect and dopant concentrations, and the integration of different components into hybrid structures. Although the ability to prepare, modify and integrate various photocatalytic materials has been well developed, there are many challenges to be addressed from the viewpoint of materials science as detailed below.

Research on extending the absorption range of photocatalysts to capture all visible light of the solar spectrum has continued for the past two decades[128-131]. Based on the sum of the theoretical 1.23 V for water splitting and the overpotential requirement of several hundred millivolts for hydrogen evolution reaction (HER) and oxygen evolution reaction (OER), the appropriate bandgap of solar-driven semiconducting photocatalysts is considered to be between 1.6 and 2 eV. Considering the requirement of the long-term stability of photocatalysts in an aqueous solution under light irradiation, metal oxides clearly stand out compared to the less stable metal sulfides, nitrides and halides. However, most stable metal oxides with appropriate band edges for water splitting suffer from wide bandgaps and find it difficult to capture visible light due to the very deep position of the O 2*p* dominant valence band maximum. Although narrowing the bandgap by introducing different electronic structure modifiers (dopants, defects, disorder and stress) is a general and widely used strategy for increasing visible light absorption, the challenges associated with this are not only

the difficulty in realizing a homogeneous distribution of the modifiers in the materials,[126, 132-135] but also the increased number of concomitant recombination centers for the photo-generated charge carriers in the materials[136].

The effectiveness of using layer structures to facilitate the diffusion of active modifiers from the surface to the bulk of materials through the interlayer spaces to obtain a homogeneous distribution has been validated in many layer photocatalysts including $Cs_{0.68}Ti_{1.83}O_4$,[132] $CsTaWO_6$[137] and g-C_3N_4[134, 135]. Compared to the mother materials, these homogeneously modified layer photocatalysts show an extraordinary band-to-band redshift of the whole absorption edge. However, the layer photocatalysts usually have a relatively low intrinsic activity due to the large energy barriers existing between layers that are maintained by weak interactions like van der Waals force and electrostatic attraction. One typical example is polymeric carbon nitride (widely described as g-C_3N_4 in the literature) with weak interlayer van der Waals force and abundant hydrogen bonds in the covalent bonding dominated intralayer framework shown in **Figure 2**[138]. The theoretical potential barriers across the local regions containing van der Waals force and hydrogen bonds are as large as 33.2 and 7.9 eV, respectively. Thus, the photo-generated charge carriers are highly localized in each melon strand as marked by the green and red angles in **Figure 2b,** resulting in a very low probability of inducing photocatalysis reactions. Innovative strategies are important to solve the challenges associated with layer structures that are also commonly used as the parent structures to produce other 2D materials. Therefore, the straightforward strategy is to produce ultrathin and/or porous sheets of layered

materials to give full exposure of each layer to the reactants. This is the first challenge to be highlighted in the development of 2D materials for efficient photocatalysis.

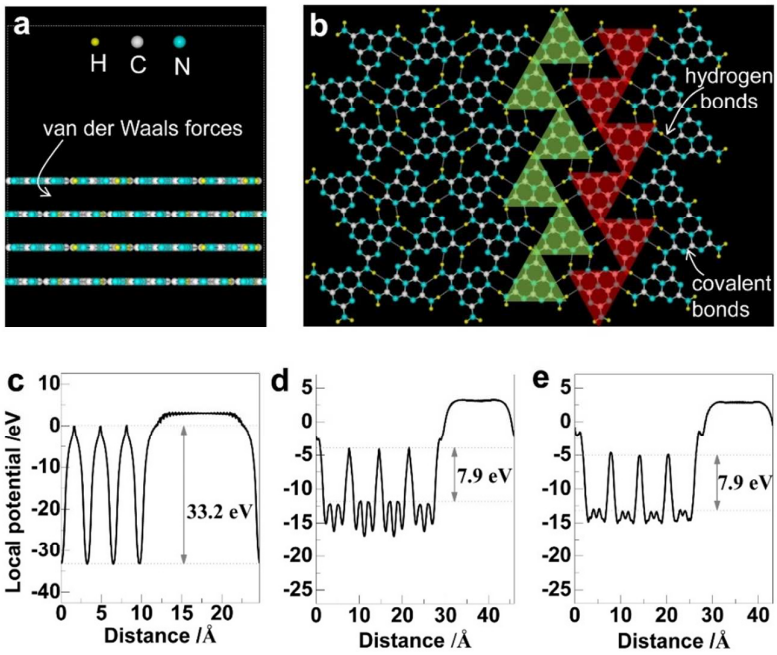

Figure 2 Atomic structures and electrostatic potentials of layer carbon nitride with hydrogen bonds. (**a**) Side and (**b**) top view of the atomic structure of layer carbon nitride. H, C and N atoms are denoted by small yellow, large white and light blue balls, respectively. Two nearest neighbor melon strands in the basal plane of monolayer carbon nitride are marked by solid green and red triangles in (**b**). The calculated electrostatic potentials along the direction perpendicular to (**c**) and the two directions parallel to (**d** and **e**) in the basal plane of the layer carbon nitride. Reproduced with permission from ref. 138. Copyright 2016, John Wiley and Sons.

Another challenge concerning the bandgap narrowing of the light absorber of a photocatalyst is to increase light absorption while maintaining the strong redox power of the photo-generated charge carriers. It is difficult to address this problem with a

photocatalyst containing a single light absorber, although loading suitable co-catalysts on it can improve the reaction kinetics, to some extent. To solve this problem, a Z-scheme photocatalytic system has been designed that uses two light absorbers and an electron-mediator to mimic the natural photosynthesis process. This design is effective not only in capturing large portion of the solar spectrum but also in maintaining the strong redox powers of the charge carriers[139]. For Z-scheme photocatalysts, efficient communication between the two light absorbers using the mediator or directly at their interface is essential for promoting photocatalysis. The advantageous features such as very large surface area and strong interfacial contact, which can be obtained by using 2D light absorbers, is therefore crucial for the construction of efficient Z-scheme photocatalysts. There is no doubt that 2D materials have an outstanding advantages in enabling intimate interfacial contact.

The separation and transport of photo-generated electrons and holes to reach the surface of light absorbers is crucial for the subsequent transfer of charge carriers in catalysis reactions. This process is intrinsically controlled by both the crystal structures and compositions of the materials, and is sensitive to the crystallinity, shape, exposed facets, defects, interfacial properties etc. The result of the much larger effective mass of valence band holes than conduction band electrons in most metal oxide photocatalysts limits the separation and transport of charge carriers[125, 140]. In clear contrast, the significance of the small effective mass of both electrons and holes for charge separation is clearly indicated by the excellent photovoltaic performance of organic-inorganic hybrid perovskite iodides [141]. Unfortunately, there is only limited

room to substantially change the effective masses of the charge carriers in most photocatalyst materials by introducing common electronic structure modifiers. One favorable factor is the surface upward band bending of the n-type metal oxides, which can partially regulate the transport behaviors of photo-generated electrons and holes by accelerating the holes and slowing the electrons in the charge depletion layer of the oxides in contact with the co-catalyst or solution. Moreover, surface band bending can be changed by controlling the concentration of free carriers, exposure of different facets, and also the size and shape of the particles[142]. On the other hand, controlling the distances that the charge carriers travel from bulk to surface along different directions provides another way of regulating the transport behaviors of the carriers. In a word, with the prerequisite of a smaller mass of electrons than holes, controlling surface band bending and distances along the transport directions of electrons and holes from bulk to surface by changing the morphology and size (for example, being 2D) of photocatalyst particles can create new ways to overcome the mobility mismatch between electrons and holes.

Catalysis reactions on the photocatalyst surface induced by photo-generated electrons and holes are controlled not only by the properties of the light absorber and co-catalyst but also by the spatial distribution of reductive and oxidative co-catalysts on the absorber. Surface atoms with different coordination numbers and surface defects sensitively affect the chemical states of sorbates on both the light absorber and the co-catalyst. Selective loading of the reductive and oxidative co-catalysts of the light absorber can significantly improve photocatalytic activity as already

demonstrated for faceted photocatalysts[127, 143, 144]. However, this facet dependent selective loading can only be used for a limited number of light absorbers. Other innovative strategies like using ferroelectric field[145] and anisotropic shape (for example, 2D sheets[146]) of materials have been developed to control the selective loading of co-catalysts.

Surface atomic structures of photocatalysts intrinsically determine the sorption behaviors of reactants/products and also the abundance and distribution of surface states. The complexity of the surface atomic structures of particles of conventional light absorbers and co-catalysts makes the rational design and construction of photocatalysts difficult to achieve. The origin of this complexity is the presence of many different micro-facets and also defects on them. The selective exposure of some specific facets with favorable features, which has been actively pursued in the last decade,[143, 147] represents an important way of simplifying the surface atomic structures of the light absorbers. Despite the rapid development of various faceted photocatalysts, the flexibility of synthesizing photocatalysts with a large percentage of the desired facets is still quite limited. Alternative strategies for controlling surface atomic structures are desirable. From this aspect, atomic or unit-cell thick 2D materials with a large basal surface have desirable uniform surface atomic structures for photocatalysis.

3. Unique physicochemical properties of 2D light absorbers

Ultrathin 2D materials show many unprecedented optical, electric, magnetic properties as a consequence of the confinement of electrons in two dimensions. The

large lateral size but atomic or unit-cell thickness offers them a high specific surface area, a fast rate of production of photo-carriers under a low photon flux density and active surface atoms，and a short migration distance for the photo-carriers. These fascinating features of 2D materials favor photocatalysis by changing light absorption, carrier transportation and separation, and surface catalytic reactions, and these will be discussed in the following sections.

3.1 Electronic structures

According to the particle-in-a-box model, the reduction of the dimensionality of a semiconductor particle leads to an increase in the degree of the quantization along the confined direction. The electronic band structure becomes sparser with respect to the density of states (DOS) along the confined direction of motion. By reducing the structure from three dimensions to two, the DOS changes from a continuous square-root dependence on E to a step-like dependence (**Figure 3**)[148]. The relationships of the DOS [N(E)] with E in bulk and 2D semiconductors have been given by:

$$N(E)_{bulk} = \frac{\sqrt{2}m^{*\frac{3}{2}}E^{\frac{1}{2}}}{\pi^2\hbar^3} \quad (1)$$

$$N(E)_{2-D} = \frac{nm^*}{\pi\hbar^2} : n = 1, 2, 3 \quad (2)$$

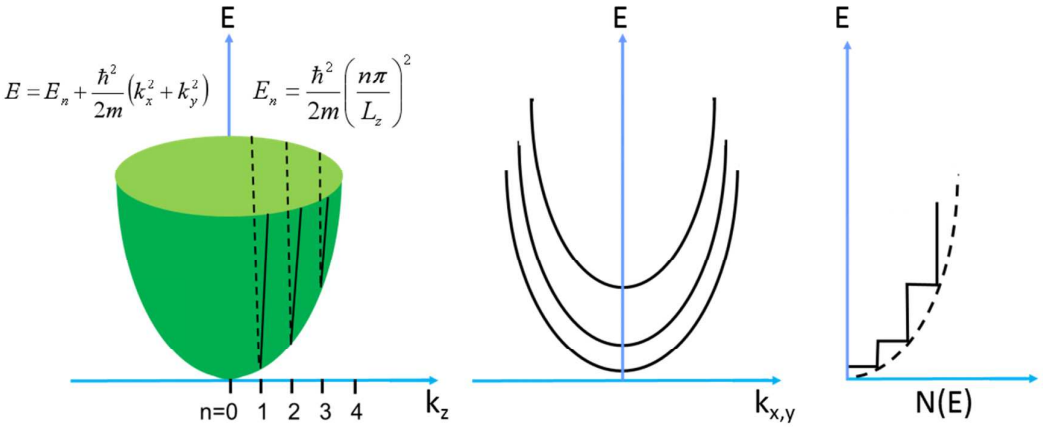

Figure 3. Schematic of a parabolic energy band in the quantum limit. Two-dimensional bands in the $k_{x,\,y}$ plane give rise to a stepped cumulative density of states with increasing energy. Modified with permission from ref. 148. Copyright 1975, Springer Nature.

Some interesting things occur due to the spatial confinement. One is that the electron–hole binding energy increases with the degree of the confinement, which leads to an increased likelihood of exciton formation. An exciton is strongly analogous to a hydrogen atom, in which the positively charged carrier hole acts as the nucleus binding to the carrier electron. The Bohr radius of excitons in a bulk semiconductor has been simplified into the following equation:

$$a_B(n) = \frac{\hbar^2 \varepsilon}{\mu e^2} n^2 = 0.53 \frac{\varepsilon}{\mu / m_0} n^2 \text{ Å} \qquad (3)$$

Where, ε is the dielectric constant of the semiconductor, μ is the reduced effective mass of the exciton ($\frac{1}{\mu} = \frac{1}{m_e^*} + \frac{1}{m_h^*}$), n is the exciton quantum number, and m_0 is the free electron mass in vacuum[149]. The binding energy for ground state (n=1) excitons in a bulk semiconductor is written in the form as

$$E_b(n=1) = \frac{13.6\mu}{m_0\varepsilon^2}\ eV = \frac{\hbar^2}{2\mu a_B^2} \quad (4)$$

Taking CdTe (m_e^*=0.067m_0, m_h^*=0.5m_0) as an example, the reduced effective mass (μ) of exciton in CdTe is 0.0828m_0. As the dielectric constant of CdTe is known as 10.6, so the 3D bulk exciton binding energy is estimated to be 10.0 meV with a Bohr radius of 6.8 nm. Once the crystal dimension becomes smaller than the Bohr radius of an exciton in a bulk semiconductor, the exciton binding energy must increase along with the degree of quantization. When the thickness (L_z) of a 2D material becomes half the Bohr radius of an exciton in bulk, the exciton binding energy increases by a factor of four compared with that in bulk. The shift (ΔE_b) in the energy of excitons is proportional to $1/L_z^2$,[150] which is given approximately by

$$\Delta E_b = \frac{\hbar^2\pi^2}{2\mu L_Z^2} \quad (5)$$

The second feature of the spatial confinement and reduced dimensionality is an enlarged bandgap. The change (ΔE_g) in energy gap (E_g) is also proportional to $1/L_z^2$,[151] which is given approximately by

$$\Delta E_g = \frac{\hbar^2\pi^2}{2\mu L_Z^2} \quad (6)$$

The stronger the confinement, the larger the bandgap and energy of optical emission resulting from electron–hole recombination. According to the particle-in-a-box approximations, 3D confinement is stronger than 2D confinement, which in turn is stronger than 1D confinement. Consequently, the change in the bandgap energy (ΔE_g) in the nanostructures of a semiconductor is greatest in quantum dots, followed by quantum rods, quantum wires and finally quantum wells (**Figure 4a** and **b**)[152]. For a 2D material, the thinner the material becomes, the stronger is the

confinement effect. This leads to a larger bandgap and thus blue-shift of optical emission peak. As a consequence of the bandgap enlargement, the band edge positions separate in opposite direction. The ability to modify the electronic structure of semiconductors by controlling the dimensionality of the structure provides an additional variable to optimize the system.

Here we shall keep using CdSe as an example. Bulk CdSe is known to be inactive for photocatalytic H_2 evolution as its conduction band edge is lower than the redox potential of hydrogen production. In contrast, 2D CdSe nanoplatelets with a thickness smaller than the Bohr radius (~5.6 nm) exhibit a noticeable blue-shift in the optical absorption and photoluminescence spectra compared to the bulk (**Figure 4c**). The blue-shift of the absorption edge increases with the reduction of the number of monolayers in the nanoplates from 7 to 4, which leads to a remarkable upward shift of the conduction band edge[153]. Once the edge is higher than the potential of proton reduction, photocatalytic hydrogen evolution becomes possible[154, 155].

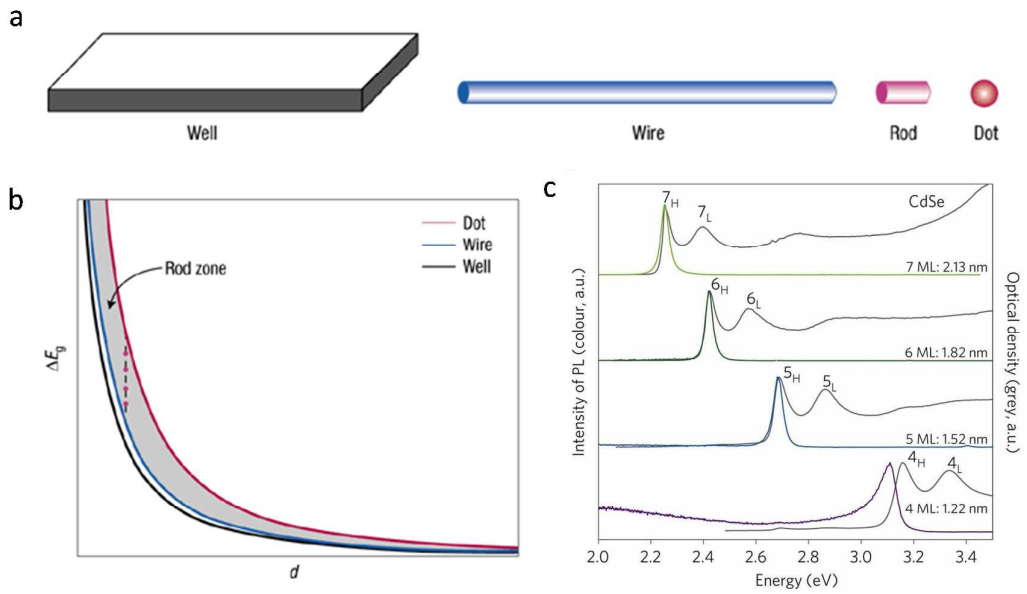

Figure 4. (a) Geometries of the different structures. (b) Plots of ΔE_g (the increase in the bandgap over the value for bulk material) against d (the thickness or diameter) for rectangular quantum wells, cylindrical quantum wires and spherical quantum dots obtained from particle-in-a-box approximations. The grey area between the dot and wire curves is the intermediate zone corresponding to quantum rods. Reproduced with permission from ref. 152. Copyright 2003, Springer Nature. (c) Emission and absorption spectra of CdSe nanoplatelets with different numbers of monolayers. Reproduced with permission from ref. 153. Copyright 2011, Springer Nature.

The third remarkable feature of 2D materials because of the confinement is the possible transition between an indirect and a direct bandgap. As an example, MoS_2 undergoes an indirect-to-direct bandgap transition when its thickness is reduced to a monolayer, as shown in **Figure 5a**[156, 157]. Reducing the number of layers in MoS_2 strengthens the confinement effect, which causes the increased indirect gap. The transition from the indirect to direct bandgap occurs in the monolayer. Such a

transition causes a more than 10^4-fold increase of the luminescence quantum yield observed in the monolayer (**Figure 5b**).[156]

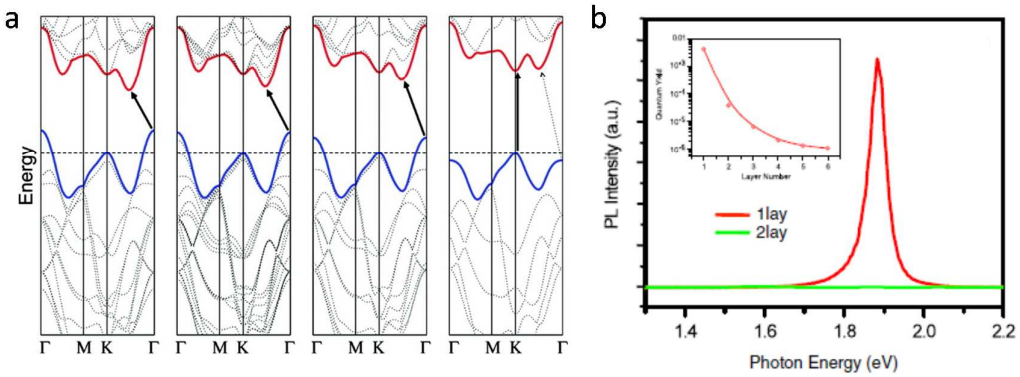

Figure 5. (a) Calculated band structures of bulk MoS_2, four-layer MoS_2, bilayer MoS_2 and monolayer MoS_2 from left to right. The solid arrows indicate the lowest energy transitions. Bulk MoS_2 is characterized by an indirect band gap. The direct excitonic transitions occur at high energies at the K point. With reduced layer thickness, the indirect band gap becomes larger, while the direct excitonic transition barely changes. Monolayer MoS_2 becomes a direct band gap semiconductor. Reproduced with permission from ref. 157. Copyright 2010, American Chemical Society. (b) PL spectra of mono- and bilayer MoS_2 samples in the photon energy range from 1.3 to 2.2 eV. Inset: PL quantum yield of thin layers (1-6 layers). Reproduced with permission from ref. 156. Copyright 2010, American Physical Society.

Another feature is that the atomically thin nanosheets typically possess a higher DOSs near the band edges compared to their bulk counterparts. This provides new opportunities to modify the electronic properties including the mobility and

concentration of carriers. Compared to the bulk, a three atoms thick SnS_2 monolayer has an increased bond length and structural distortions so that a much increased DOSs at valence band maximum is generated[158]. This feature is considered to improve the carrier mobility. The photocurrent generated from an electrode of monolayer SnS_2 under visible light is over 70 times larger than that of the bulk counterpart. Similar results were also seen in other semiconductors such as ZnSe, C_3N_4 and Bi_2WO_6 nanosheets with unit-cell thickness[159-161].

3.2 Optical absorption characteristics

The optical absorption characteristics of semiconductors are intrinsically determined by their band structures. As discussed in Section 3.1, the quantum confinement effect leads to an increase in the bandgap and thus a narrower absorption range for ultrathin 2D nanosheets. Meanwhile, the DOSs in the nanosheets appears to be a step-like distribution with energy so their absorption edge is also step-like. These steps originate from excitations from relatively discrete valence-band states (sub-band states) to discrete conduction-band states (**Figure 6d**). When the binding energies of the excitons are larger than the thermal energy (kT), sharp peaks with energies corresponding to confined excitons appear at each step (**Figure 6b**). Taking InAs with a large Bohr radium of ~34 nm as an example, a strong quantum confinement of carriers is readily obtained in quantum membrane thicknesses less than 20-nm. As a result of the interband transitions between the subbands of 2D InAs nano-membranes, stepwise absorption spectra can be observed at room temperature in such free-standing membranes with thicknesses ranging from 3 to 19 nm. Meanwhile, the

absorption edge has a gradual blue-shift with thickness decrease from 19 to ~3 nm (**Figure 6e**)[162].

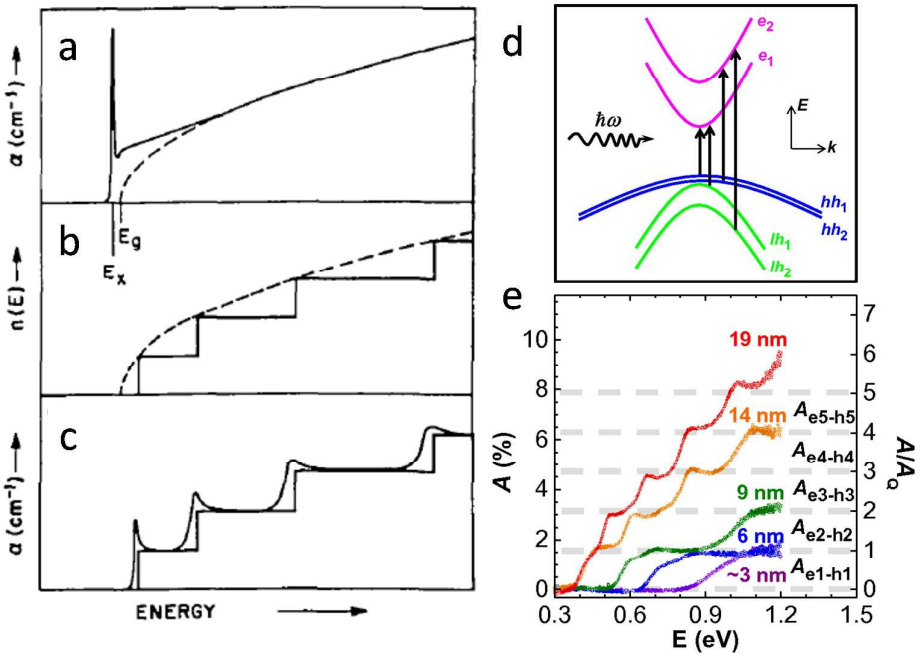

Figure 6. (a) Bulk GaAs band-edge absorption profile including exciton effects shown together with the bulk conduction band DOSs; (b) Comparison of the bulk and quantum limit (two-dimensional) DOSs of an energy band; (c) Schematic of absorption spectra for valence band to quantized conduction band transitions with and without exciton effects at each two-dimensional band edge; Reproduced with permission from ref. 148. Copyright 1975, Springer Nature. (d) Schematic of the qualitative band structure of a 2D InAs QM, with arrows indicating the allowed optical transitions between valence and conduction subbands; (e) Absorption spectra of InAs QMs with thickness of L_z ~ 3 nm, 6 nm, 9 nm, 14 nm, and 19 nm at room temperature, A_{en}-h_n represent the absorption from the corresponding interband transitions, e_n–hh_n and e_n–lh_n. Reproduced with permission from ref. 162. Copyright

2013, National Academy of Sciences.

The enlarged bandgap of 2D materials is favorable for inducing redox reactions because of the large driving force of the photogenerated charge carriers. However, in terms of solar light utilization, the large bandgap limits the capture of low-energy photons in sunlight. Band engineering by various electronic structure modifiers is highly important in producing a wider absorption range. As surface atoms in 2D nanomaterials become dominant, surface modifications could drastically change the electronic structure of the nanosheets to obtain the desired optical absorption.

3.3 Spatial separation of photogenerated charge carriers

One remarkable property of semiconductor nanosheets as photocatalyst is the effective spatial separation of photogenerated electrons and holes between the edges and basal surface of the nanosheets. As indicated in **Figure 7**, the photodeposition of Cu_2O and MnO_2 particles occurs selectively on the edges and surface of the lepidocrocite-type $Ti_{0.91}O_2$ nanosheets with a crystallographic thickness of 0.75 nm, respectively[146]. It is proposed that the electron moves in the 3d conduction band mainly consisting of the Ti^{4+} network in the 2D nanosheet and then reduces Cu^{2+} at the edge, while the hole exists in the 2p valence band mainly consisting of the O^{2-} surface and oxidizes Mn^{2+} on the surface. This phenomenon is also observed for the selective photodeposition of other products including Ag and Cu and is independent of the pH value of the reaction solutions (a lower pH simply reduces the reactivity), suggesting that the spatial separation of the charge carriers can be controlled by an

intrinsic feature of the 2D nanosheets.

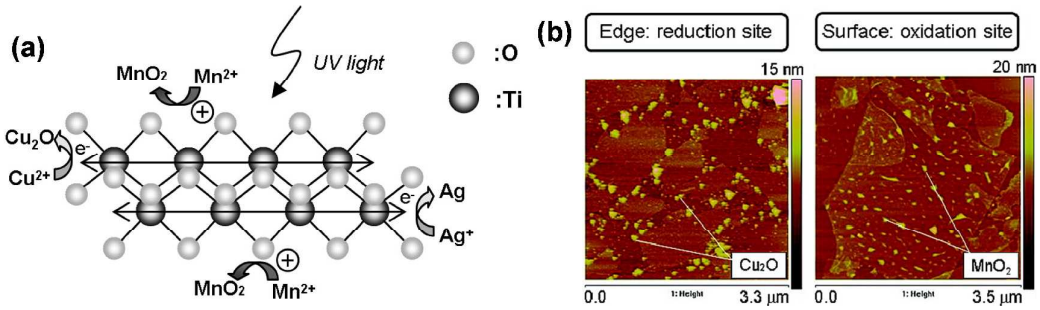

Figure 7. (a) Model of the movements of the photoproduced electron and hole in a TiO_x nanosheet with a lepidocrosite structure. The electron moves in the 3d CB consisting of the Ti^{4+} network in the nanosheet and then reduces Ag^+ and Cu^{2+} at the edge of the 2D sheets, while the hole exists in the 2p VB consisting of the O^{2-} surface and oxidizes Mn^{2+} on the flat surface. **(b)** AFM images of TiO_x nanosheets photodeposited under UV light (265 nm) illumination; nanosheets deposited with (left panel) Cu_2O and (right panel) MnO_2. Reproduced with permission from ref. 146. Copyright 2008, American Chemical Society.

Despite the obvious spatial separation of the reductive and oxidative sites on a $Ti_{0.91}O_2$ monolayer film, the results from individually dispersed nanosheets of calcium niobate are controversial. Based on TEM images, Compton *et al.* claimed the nanosheet edges as the reductive sites by monitoring the distribution of the photodeposited Pt nanoparticles on the $TBA_x[H_{1-x}Ca_2Nb_3O_{10}]$ (x = 0.15-0.20) nanosheets with a thickness of 1.16 nm and a lateral size of around 1.2 μm as a particulate photocatalyst[163]. It was proposed that dangling Nb-O-bonds at the edges

provide Pt nucleation sites that are absent from the surface of the nanosheets. However, TEM results from Ebina *et al.* seem to support the dominant distribution of Pt nanoparticles on the basal surface of the $Ca_2Nb_3O_{10}$ nanosheets after the photoreduction of $PtCl_6^{2-}$ at a high concentration (3 wt%) of $PtCl_6^{2-}$ ions[164], while a 0.1 wt% Pt-loaded nanosheet has Pt nanoclusters on the edges. This inconsistency might be caused by the following three factors. 1) The nucleation and growth of Pt (or other reductive products) nanoparticles on the ultrathin edges of individually dispersed nanosheets in solution, whose positions always change during the reaction, is very hard to control. In contrast, the edges of nanosheets immobilized in a monolayer film do not move during the photodeposition process, which may facilitate the nucleation and growth of the Pt nanoparticles. 2) Some oxygen vacancies on the basal surface of the nanosheets lead to the exposure of some metal atoms and thus provide additional pathways for the diffusion of the photogenerated electrons to reach the surface. 3) Some isolated Pt nanoparticles produced by the photochemical reaction of $PtCl_6^{2-}$ ions might be reloaded on the surface of the nanosheets. Based on a comprehensive analysis of the results, we tend to believe the first of these plays the dominant role. Future studies on the spatial distribution of the reductive and oxidative sites of the nanosheets, for instance edges vs flat surface, are required to clarify the origin of the inconsistency.

The spatial separation of reductive and oxidative sties has also been realized in some organic 2D materials that have emerged as a new class of attractive photocatalysts. Among them, carbon nitride polymer (g-C_3N_4), which was explored as

a visible light photocatalysts for the first time by Wang *et al* in 2009[165], has a graphite-like layer structure that allows the production of various ultrathin carbon nitride nanosheets. The dominant distribution of photodeposited Pt nanoparticles on the edges of the sheets suggests the edges are the reductive sites[40]. Compared to single-layer metal oxide nanosheets with metal cations and oxygen anions in alternate atomic layers, the single-layer carbon nitride nanosheet has its carbon cations and nitrogen anions in the same layer. Therefore, the mechanism of controlling its charge separation between the edges and basal surface should be different and deserves further study.

Although similar spatial separation of the photogenerated electrons and holes on different facets was also observed in photocatalysts, the driving force has been shown to be the difference in work function of the facets and thus surface band bending at different facets. Compared to the strategy of selective exposure of different facets to enable the spatial separation of the charge carriers, 2D structure design provides an alternative flexible way to induce spatial separation of the photo-generated charge carriers for improved photocatalytic activity.

3.4. Planner host of abundant guests

Owing to their geometric shape, charged surface, and abundant unsaturated surface atoms, 2D nanosheets have the outstanding advantage of being able to host some active guests to enrich or tailor their properties. Some typical progress is now reviewed to demonstrate such advantages.

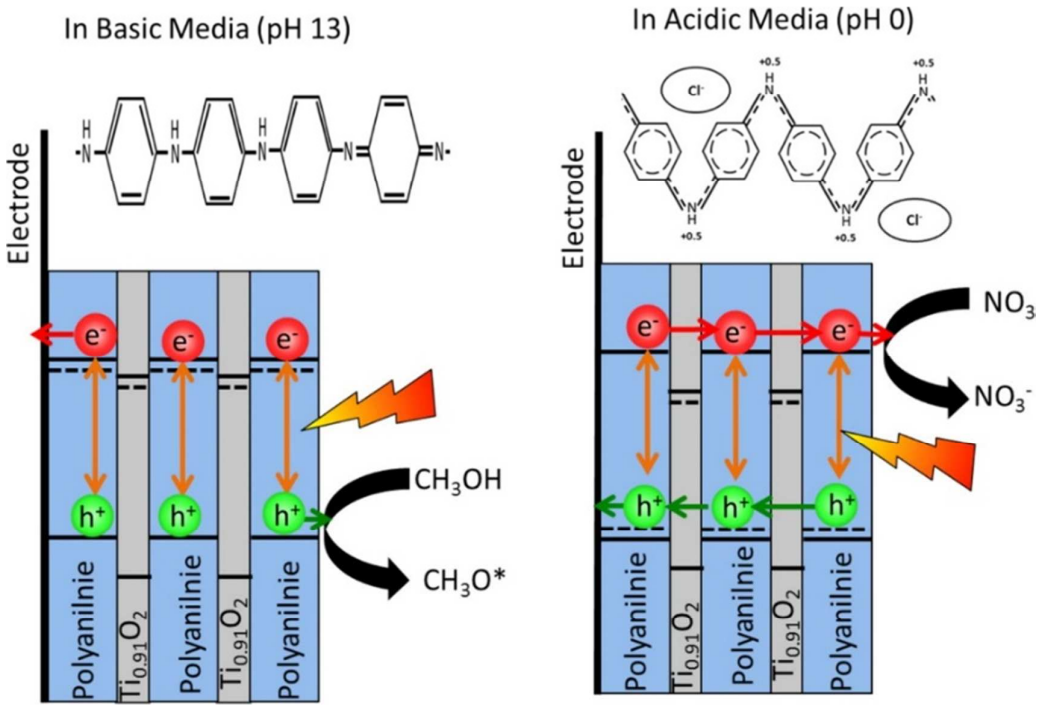

Figure 8. Scheme of multilayer thin films containing alternate conducting PANI and exfoliated $Ti_{0.91}O_2^{0.36-}$ nanosheets. Because of the significant structure changes in the PANI molecule under basic and acidic conditions, when used as photoelectrodes the multilayer films exhibit a unique n-type to p-type switchable electron transfer behavior under different pH conditions. Reproduced with permission from ref. 166. Copyright 2013, John Wiley and Sons.

For the assembly films of the nanosheets, the binders between them can play an additional role in changing the photo-response properties of the electrodes of the films. One interesting example demonstrated by Seger *et al.* is an n-type to p-type switchable photoelectrode assembled from alternating exfoliated $Ti_{0.91}O_2$ nanosheets and polyaniline (PANI) layers[166]. The behaviors of the photoelectrode are found to be very sensitive to the pH value of the electrolyte and give an anodic photocurrent in a

strong basic electrolyte and a cathodic photocurrent in a strong acidic electrolyte under light irradiation, as illustrated in **Figure 8**. This pH dependent photocurrent property is intrinsically related to the changed structure of PANI under different pH conditions. PANI acts as an n-type semiconductor in basic conditions while acidic conditions make it act as a p-type semiconductor by protonating its nitrogen atoms. This finding might provide a strategy for controlling both the type and intensity of the photocurrent of the electrodes for not only photoelectrochemical water splitting but also other photo-active devices.

Other molecules or ions with desirable functions can also be introduced into the spaces between the nanosheets to tailor their properties. One example related to photocatalysis is flocculated $Ti_{0.91}O_2$ nanosheets with iodine molecules in the interlayer spaces, which show an extraordinary band-to-band redshift of the absorption edge to 2.38 eV compared to 3.29 eV for flocculated nanosheets without the iodine molecules as shown in **Figure 9**.[167] The origin of the observed redshift is the upward shift of the valence band maximum at a high iodine concentration. The resultant nanosheets have the ability to photocatalytically decompose Rhodamine B under visible light. In principle, this strategy of using the strong adsorption of the negatively charged nanosheets towards nonpolar iodine molecules is generic for the realization of the effective coupling of various charged nanosheets of metal oxides with functional molecules to extend the absorption range of metal oxides that usually have too large bandgap to capture visible light. In addition, this strategy might be applicable to further increase the light absorption capability of the hybrids of the charged 2D materials.[168-172] It should be noted that the separation of photogenerated charge carriers in 2D light absorbers mainly origins from their structure anisotropies along different crystallographic orientations. While the separation of photo-generated charge carriers in 2D nanosheet hybrids is mainly induced by the energy difference between the band alignments of two or multiple components.

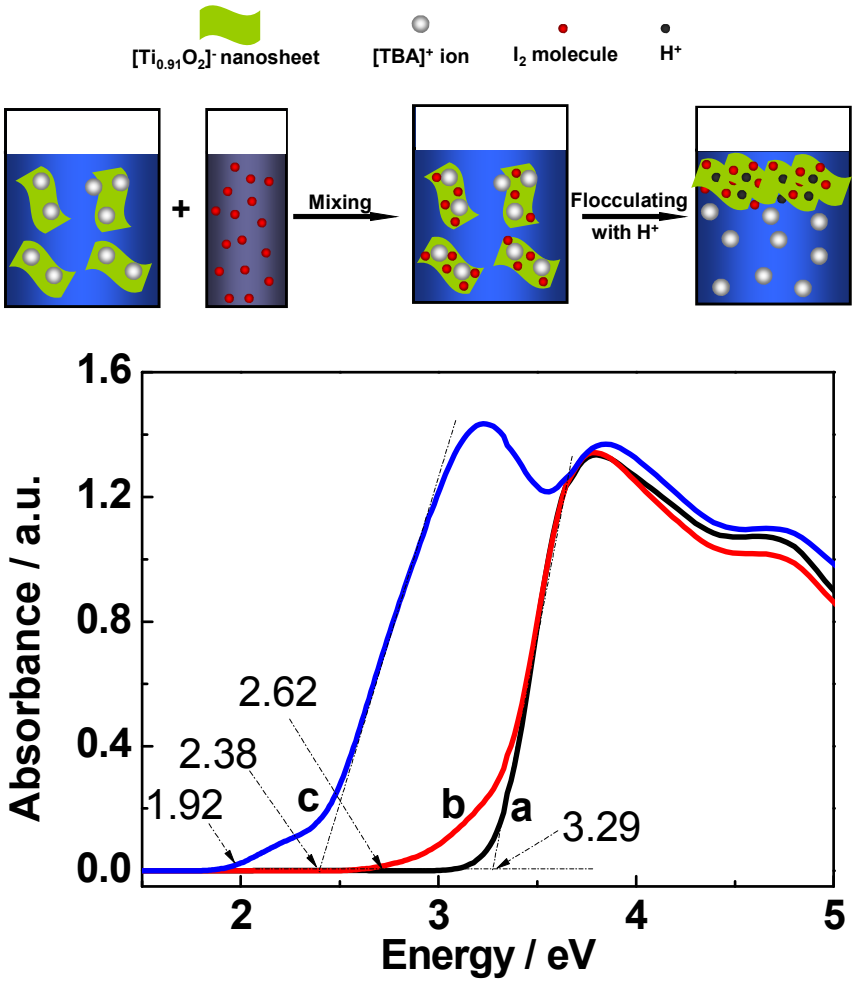

Figure 9. Schematic of the coupling of $Ti_{0.91}O_2$ nanosheets with I_2 molecules. Plots of the transformed Kubelka-Munk function versus the energy of the light recorded from the flocculated (X%) I_2-$Ti_{091}O_2$ sheets with different amounts of I_2 dopant: a, X = 0; b, X = 0.4; c, X = 1.2. Reproduced with permission from ref. 167. Copyright 2011, Royal Society of Chemistry.

Loading co-catalysts is almost indispensable for the construction of photocatalysts for solar fuel generation[173, 174]. Compared to bulk or even nanosized particles, nanosheets with a large surface have the advantage of being able to host co-catalysts

and studies have shown the feasibility of doing this for molecular and even single-atom co-catalysts. For instance, Bi *et al.* used $K_4Nb_6O_{17}$ nanosheets with a lateral size ranging from 100 to 500 nm and a thickness of several nanometers to host trifluoroacetic acid (TFA), by virtue of its reversible redox couple TFA•/TFA^-, as a homogeneous co-catalyst for photocatalytic hydrogen generation, as shown in **Figure 10**.[73] As a result of the greatly promoted transfer of holes from the nanosheets to the molecular co-catalysts and the maximized contact areas between the co-catalysts and reactants, the nanosheets have an increased photocatalytic hydrogen production rate 32 times that of the bare nanosheets.

Single atom catalysts supported on different substrates have emerged as an attractive class of new catalysts for various catalysis reactions[175]. The concept of single atom catalysis has also been introduced to produce photocatalysis by loading noble metal atoms on a light absorber to maximize their efficiency. The effective anchoring of a high concentration of co-catalyst single atoms on a light absorber usually requires it to have a large surface area, which is one of the features of 2D materials. Isolated single Pt atoms as a new co-catalyst for the hydrogen evolution reaction have been embedded in sub-nanopores of 2D g-C_3N_4[92] and result in a photocatalytic H_2 generation which is 8.6 times higher than that of Pt nanoparticles on a per Pt atom basis. The single-atom Pt is determined to be located on top of the five-membered rings of g-C_3N_4 where it forms Pt-C/N bonds. The synergy of the prolonged lifetime of photo-generated electrons and changed surface trap states produced by the introduced single-atom Pt atoms in the g-C_3N_4 framework is

proposed to be responsible for the higher photocatalyst activity. Another example by Li *et al.* also demonstrated the significance of forming Pt-N bonds in the framework of g-C_3N_4 by producing visible-near-infrared photocatalytic hydrogen generation[176]. In addition, single atoms of palladium and platinum supported on graphitic carbon nitride acting as photocatalysts for CO_2 reduction have been investigated by density functional theory calculations[177].

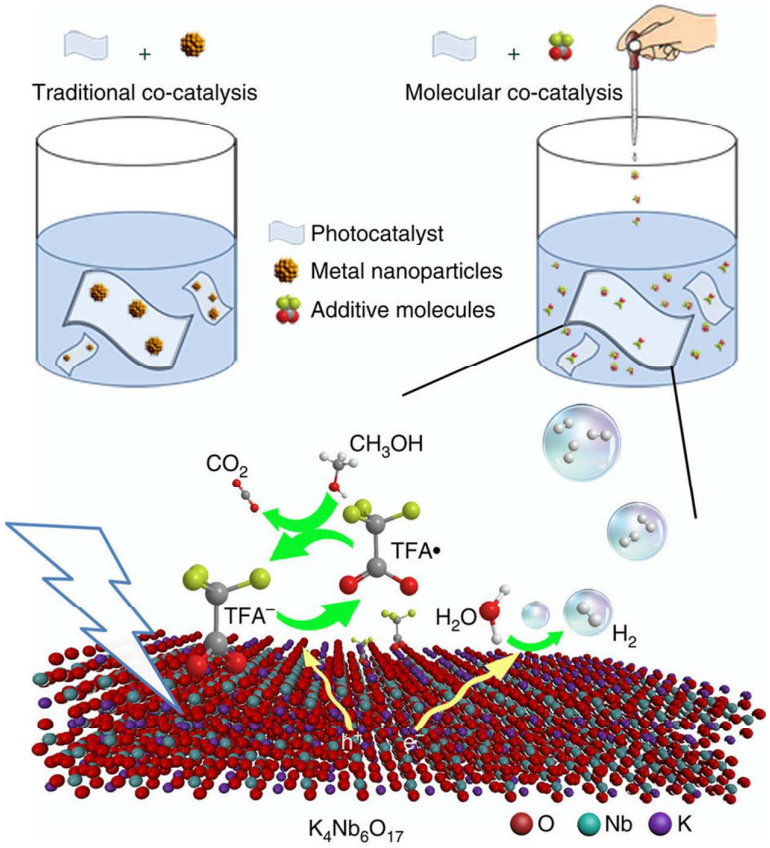

Figure 10. Schematic of the molecular co-catalyst strategy for accelerating hole transfer. Homogeneous molecular co-catalysts use reversible redox couple and highly active free radical reactions to promote hole transport, unlike supported heterogeneous co-catalysts, which are constrained by the finite contact areas between co-catalysts and reactants. Purple, cyan and red spheres denote K, Nb and O atoms,

respectively. Reproduced with permission from ref. 73. Copyright 2015, Springer Nature.

3.5. Strain-modulated band structures

Band structure engineering of semiconductors has long been pursued in order to fully capture solar light and change the redox ability of photogenerated charge carriers for efficient solar-driven photocatalysis. The introduction of elastic strain as a continuous variable is considered a highly desirable way of changing the physical and chemical properties of a material without changing its chemical compositions. However, there is usually little opportunity for producing a homogeneous elastic strain in three-dimensional bulk materials which intrinsically limits the use of this effect. The emergence of 2D monolayers that can withstand a very high elastic strain provides a new opportunity to use elastic strain engineering to modify the electronic structures.

An interesting example is that a monolayer of molybdenum disulphide (MoS_2) can withstand an effective in-plane strain of up to 11%[178], which is high enough to cause a substantial change to its band structure. A systematic investigation of the dependence of band structure of a MoS_2 monolayer on biaxial strain up to 9% has been theoretically and computationally gived[179]. The results shown in **Figure 11** clearly demonstrate that both the direct and indirect bandgaps of a MoS_2 monolayer continuously decrease with increasing strain. The excitation energy correspondingly decreases from 2.0 eV at zero strain to 1.1 eV at a 9% biaxial strain. Conley *et al*. showed that the bandgap decrease of MoS_2 that is nearly linear with strain, and ~45

meV/% strain for monolayer MoS_2 and ~120 meV/% strain for bilayer MoS_2 has been determined by photoluminescence spectroscopy[180]. Moreover, a pronounced strain-induced decrease in the photoluminescence intensity of monolayer MoS_2 at an applied strain of ~1% that is attributed to a direct-to-indirect transition of the character of the optical band gap. Elastic strain engineering is a general method for changing the band structure of other 2D materials as demonstrated in phosphorene[68, 181-183]. All these results strongly indicate that there are many possibilities for changing the band structure of 2D semiconductors using elastic strain in order to obtain desired optical properties, particularly a smaller bandgap for the wider solar light absorption.

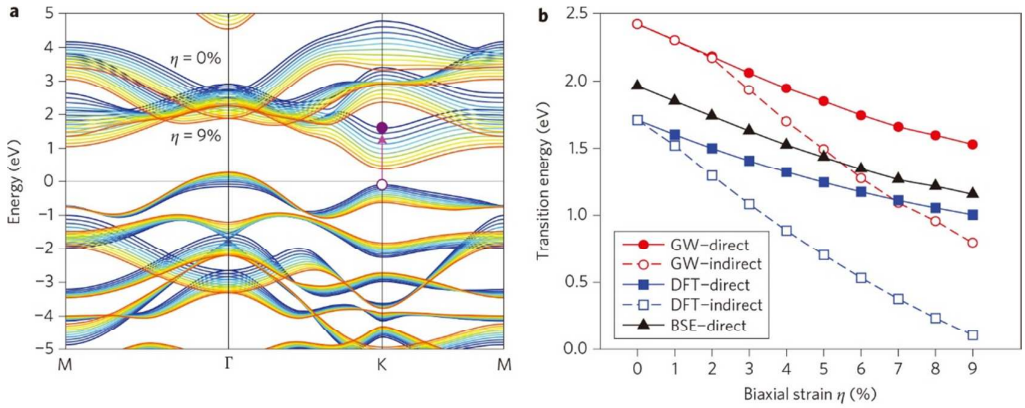

Figure 11. Strain-dependent electronic and optical properties of a MoS_2 monolayer. **a**, Electronic DFT band structure under different biaxial strains from 0% (blue line) to 9% (red line). **b**, Direct and indirect bandgaps under different biaxial strains calculated using DFT and GW. The GW direct bandgap refers to the minimum direct transition energy. It is located at the K points of the hexagonal Brillouin zone, indicated by an arrow in a. The corresponding lowest optical excitation energy (black triangles) is calculated by BSE on top of GW quasiparticle energies with electron–hole Coulomb

interaction included. Reproduced with permission from ref. 183. Copyright 2012, Springer Nature

Elastic strain engineering has also been used to modulate the band structure of 2D photocatalysts and has demonstrated its effectiveness in increasing visible light absorption by narrowing the bandgap. Freestanding lepidocrocite 2D TiO_2 with a bandgap of 1.84 eV that can absorb all visible light and a portion of the near infrared light (**Figure 12a**) was synthesized by a one-step solvothermal method[184]. The presence of large non-uniform strain in the freestanding monolayer with a thickness of around 1 nm and crumpled morphology has shown to be the origin of the much smaller bandgap than that of its flat counterpart (4.7 eV). The effects on the bandgap of lattice distortions (4% and 20% compressive strain along the a and b axes, respectively, together with a distortion in the angle between the a and b axes, from 90° to 116° in **Figure 12b**) shown by an STEM image of a nanosheet have been theoretically investigated as shown in **Figure 12c**. The strained TiO_2 monolayer has a much smaller bandgap than that of an unstrained monolayer. These highly strained 2D nanosheets exhibit obvious photocatalytic activity under light irradiation with wavelengths of higher than 700 nm.

All ultrathin, particularly unit-cell thin nanosheets actually tend to be crumpled in order to improve their stability. The concomitant structural distortions cause additional visible light absorption by allowing some originally prohibited excitation processes and/or promoting the separation of photogenerated charge carriers. Compared to flat nanosheets, crumpled g-C_3N_4 nanosheets[185, 186] were shown

experimentally and theoretically to have an extended visible light range because of n→π* excitation caused by the structural distortion[187]. It was also demonstrated that the photocatalytic activity of g-C_3N_4 with structural distortion increases with the degree of distortion in the crystal[188]. These studies suggests the significant role of strain engineering for designing and understanding nanosheets-based photocatalysts.

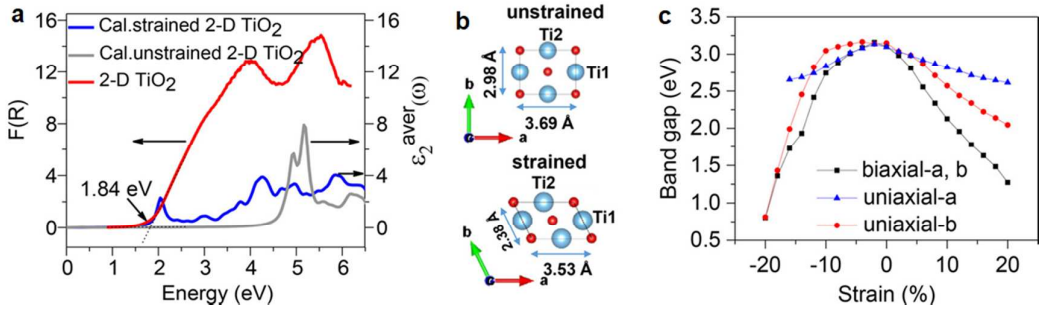

Figure 12. (a) Left vertical axis: The Kubelka−Munk functions plotted for the estimation of the optical band gap (R, the reflectance tested on the sample). The optical band gap was obtained by extending the slopes of the curve, to intercept the energy axis. Right vertical axis: Optical absorption (as a function of energy) computed from GW-BSE calculations for unstrained and strained lepidocrocite monolayer ($\varepsilon_2^{aver} = (\varepsilon_2^{xx} + \varepsilon_2^{yy})/2$); the strained lattice is taken from an STM image. Atomic and electronic structure of strained lepidocrocite TiO_2 monolayer. **(b)** Top views of the atomic structures for a one-layer 2-D lepidocrocite phase TiO_2. **(c)** Calculated DFT LDA band gap as a function of different uniaxial and biaxial strains for the lepidocrocite TiO_2 monolayer. Reproduced with permission from ref. 184. Copyright 2017, American Chemical Society.

4. Use of 2D light absorbers in photocatalysis

The 2D structures of oxides, hydroxides, oxyhalides, nitrides and dichalcogenides of many transition metals, and metal-free compounds and elements have been intensively investigated as light absorbers[11, 43, 85, 102, 105-108, 110-113, 116, 117, 189-193]. Considering the requirements of long-term stability and low-cost for light absorbers for solar fuels, representative results from the oxide family, which normally have very good chemical stability and long lifttime for photocatalysis reactions, will be mainly discussed as model systems to demonstrate the unusual photocatalytic properties of 2D materials.

4.1. Non-porous 2D light absorbers

Among a variety of transition metal oxide based photocatalysts, there is no doubt that titanium oxide is the most important model photocatalyst and it has been intensively studied[128]. The first example of a 2D titanium oxide material are probably the $Ti_{1-\delta}O_2^{4\delta-}$($\delta$ = 0.09–0.13) nanosheets with a theoretical thickness of 0.75 nm shown in **Figure 13a** that were produced by the delamination of lepidocrocite-type protonated titanate by reacting with tetrabutyl ammonium (TBA^+) ions[194-196]. Depending on the particle size of the protonated titanate used, the lateral size of the $Ti_{1-\delta}O_2^{4\delta-}$ sheets varies from several nanometers to tens of microns. An aqueous suspension of these macromolecule-like negatively charged sheets that are charge-compensated and stabilized by TBA^+ ions can stably exist for several months and even years at room temperature. The nature of the negatively charged surface and the high stability of these ultrathin sheets makes them promising building blocks for the construction of

various photocatalysts. As a light absorber, the first feature to be concerned with is its band structure that determines the absorption range, energies of photo-generated electrons and holes, and the mobility of charge carriers. On the basis of a combination of electrochemical (Mott-Schottky method) and optical absorption measurements, the bandgap of the $Ti_{0.91}O_2^{0.36-}$ nanosheets was determined to be 3.84 eV, which is consistent with the 3.82 eV determined by measuring the photoelectrochemical response range of a photoanode of $Ti_{0.91}O_2^{0.36-}$ nanosheets. Their bandgap is much larger than that of the anatase (3.2 eV) and rutile TiO_2 (3 eV) polymorphs. The reason for the larger bandgap of the nanosheets is the obvious quantum size effect associated with their small thickness. Compared with anatase TiO_2, the edges of the conduction and valence bands of the nanosheets were determined to be negatively and positively shifted by 0.12 and 0.48 eV, respectively. This unequal shift was attributed to the large difference in the effective mass of electrons and holes. A comparison of the total densities of electronic states of single layer TiO_2, bulk anatase and rutile TiO_2 (**Figure 13b)** consistently shows a larger bandgap of single layer TiO_2 than anatase and rutile TiO_2[197]. Moreover, the density of total states of the single layer is quite different from that of rutile, but is similar to that of anatase TiO_2 except for the bandgap probably because of their similar atomic arrangements. This is also indicated by the easy topotactic transformation from the lepidocrocite-type titanates or their single layers to anatase TiO_2 particles.

Despite the theoretically similar densities of states of the nanosheets and anataase, the former have a remarkably different optical absorption band with a sharp peak at

around 260 nm, as shown in **Figure 13c**[196]. This peak is related to the exciton absorption, which is commonly observed in the optical absorption bands of materials with strong exciton binding energies (for example, semiconductor quantum dots). The absorbance of this sharp peak increases almost linearly with an increase of the concentration of the nanosheet colloid or an increase in the number of layers in the nanosheet films (**Figure 13d**)[35], indicating the high dispersion with no obvious interactions between single nanosheet. This property is theoretically supported by the unchanged bandgap of stacked layers separated by a 1 nm thick vacuum slab compared with that of a single layer (**Figure 13b**)[197].

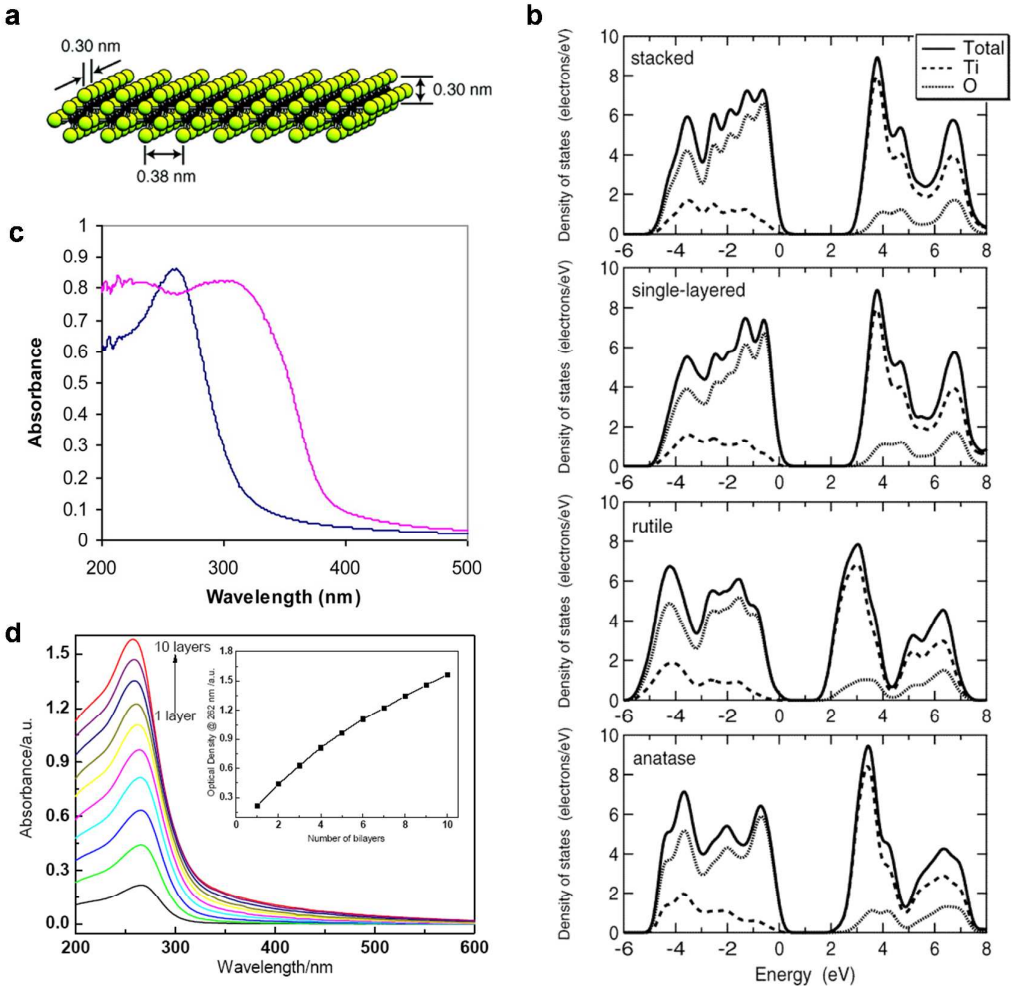

Figure 13. (a) Atomic structure of the nanosheet crystallites of $Ti_{1-\delta}O_2^{4\delta-}$. Red and yellow circles represent Ti and O atoms, respectively. Reproduced with permission from ref. 195. Copyright 2004, American Chemical Society. (b) Total and partial density of states for a stacked TiO_2, a single-layer TiO_2, rutile and anatase TiO_2. Reproduced with permission from ref. 197. Copyright 2003, American Chemical Society. (c) UV−vis absorption spectra of exfoliated $Ti_{0.91}O_2^{0.36\square}$ nanosheets (blue) and anatase TiO_2 nanoparticles (pink). Reproduced with permission from ref. 196. Copyright 2003, American Chemical Society. (d) UV-visible absorption spectra for multilayer films of (PEI/ $Ti_{0.91}O_2$)n on a quartz glass substrate. The inserted figure is the dependence of peak absorbance at 262 nm on the number of deposition cycles. Reproduced with permission from ref. 35. Copyright 2009, Royal Society of Chemistry.

Due to the coexistence of TBA^+ ions as the stabilizer and charge-compensator for the $Ti_{1-\delta}O_2^{4\delta-}$ nanosheets, an exact evaluation of the photocatalytic activity of the nanosheets is hard to make. So far, most studies on the photocatalytic properties of nanosheets of various metal oxides, produced by exfoliation using the insertion of ions, used restacked particles or nanostructures of the nanosheets and assembled films obtained by many methods including freeze-drying, spray-drying, flocculation, electrostatic sequential deposition and Langmuir-Blodgett deposition. The early study by Sakai *et al.*[195] demonstrated that the photoelectrochemical (PEC) properties of photoanode films composed of *n* layer pairs of $Ti_{0.91}O_2^{0.36-}$ nanosheets and

poly(diallydimethylammonium) (PDDA) polymer binder (exactly, ITO/PEI/nanosheet/(PDDA/nanosheet)$_{n-1}$) depended on the number of layers. Two related features were derived from the PEC and optical absorption results obtained from the films. One is the unchanged bandgap energy for nanosheet photoanodes with different numbers of layers, suggesting that a nanosheet is electronically isolated in multilayer assemblies without affecting the electronic state of neighboring nanosheets. The other is that the incident photon conversion efficiency (IPCE) of photoanodes with different numbers of layers (n) shows a far from linear increase with n (IPCE is only doubled when n increases from 2 to 10). This can be easily understood because the diffusion of the photogenerated electrons and holes in the photoanodes towards the ITO current collector and electrode-electrolyte interface, respectively, is greatly limited by the large potential barrier between the electronically isolated nanosheets. This challenge also exists in particulate photocatalysts with a layer structure, where the interaction between unit layers is weak. These two features provide a very important guide for the design of efficient layer heterostructures and understanding their photocatalytic properties.

Among a number of metal oxide nanosheets exfoliated from their bulk counterparts, nanosheets of niobium- and tantalum-based oxides (some of their structures are shown in **Figure 14**)[198] are promising light absorbers for photocatalytic hydrogen generation, in particular overall water splitting. Compared with the titania nanosheets, these nanosheets have similar properties including a negatively charged surface, electronically isolated layer-by-layer assembly, quantum size effects, and the spatial

separation of the photogenerated charge carriers. Based on electrochemical and photoelectrochemical measurements of the niobium-based oxide nanosheets, the electronic band alignments and band edges are important electronic parameters that control photocatalytic activity, and vary somewhat with a change of composition, For instance, $Ca_2Nb_3O_{10}^-$ nanosheets have the smallest bandgap of 3.44 eV, and the bandgaps of the $TiNbO_5^-$, $Ti_2NbO_7^-$ and $Ti_5NbO_{14}^{3-}$ nanosheets are also smaller than that of the $Ti_{0.91}O_2^{0.36-}$ nanosheets, as shown in **Figure 15**.[199] Mott-Schottky analysis of the layer-by-layer assembled films of perovskite nanosheets with the general formula $A_2B_3O_{10}$ including $Sr_2Nb_3O_{10}$, $Ca_2Nb_3O_{10}$, $Ca_2Nb_{2.25}Ta_{0.75}O_{10}$, and $Ca_2Nb_{1.5}Ta_{1.5}O_{10}$ suggests a pH dependence of their flatband potentials close to −59 mV per pH.[200] Nanosheets with tunable band edge potentials and well-controlled other parameters (for example, comparable thickness, high crystallinity, and a very low concentration of defects) provide good candidates to help understand the band structure-dependent photocatalytic activity at the nanoscale. Moreover, the band edge potentials of all these nanosheets are suitable for water splitting to release hydrogen and oxygen. Equally important, surface atomic configurations and arrangements of these metal oxide nanosheets can be considered the same as that of their mother layer materials, so that it is reasonable to state that changes in the photocatalytic properties of the nanosheets can be exclusively attributed to effects related to their ultrathin thickness.

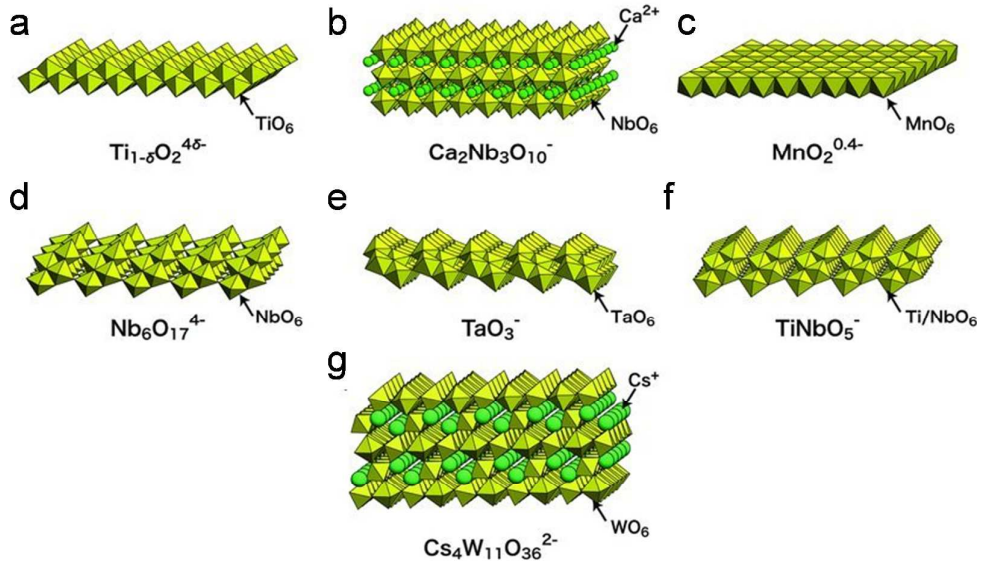

Figure 14. Structure of typical oxide nanosheets. a) titanium oxide; b) calcium niobium oxide; c) manganese oxide; d) niobium oxide; e) tantalum oxide; f) titanium niobium oxide; g) cesium tungsten oxide. Reproduced with permission from ref. 198. Copyright 2010, John Wiley and Sons.

Wide bandgap calcium niobate nanosheets as photocatalysts have exhibited promising photocatalytic water splitting activity under UV light irradiation, as shown by an early study by Ebina *et al.*[164] They demonstrated that photocatalytic hydrogen generation from an aqueous methanol solution with restacked $Ca_2Nb_3O_{10}$ nanosheets by use of K^+ ions is increased from a value of 63 μmol h^{-1} for their parent material $KCa_2Nb_3O_{10}$ to 550 μmol h^{-1} at an optimal loading (0.1 wt%) of Pt co-catalyst. The 8.7-fold increase seems to be rationalized simply by the 9-time surface area increase caused by exfoliation-restacking. However, restacking the 0.1 wt% Pt-loaded nanosheets with Na^+ ions leads to a 15.7x increase in hydrogen generation. This increase is attributed to the more rapid migration of the photogenerated electrons to

the nearby Pt for proton reduction because the Pt nanoparticles are located not only on the surface of the restacked agglomerates but also in the interlayer spaces. Increasing the Pt loading to 3 wt% causes the activity of the restacked Pt-loaded nanosheets to rapidly decrease from 900 to around 200 μmol h^{-1} possibly because the higher loading results in larger Pt particles (~1 nm versus 10 nm) that may have a lower catalytic activity. A large number of studies have confirmed the much superior catalytic activity of nanoclusters and single atoms of noble metals compared to their nanoparticles.

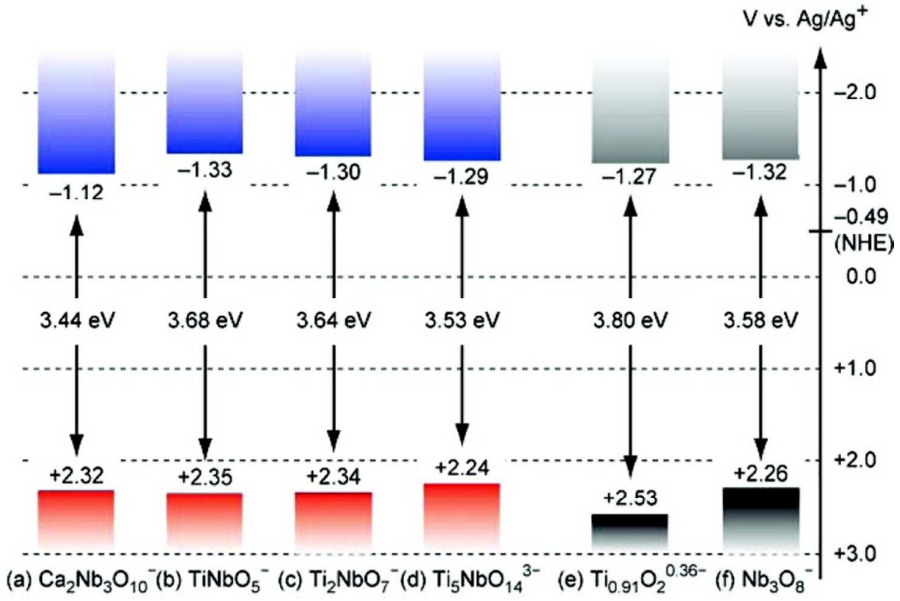

Figure 15. Energy diagram depicting the conduction-band edges, valence-band edges, and bandgap energy for (a) $Ca_2Nb_3O_{10}^-$, (b) $TiNbO_5^-$, (c) $Ti_2NbO_7^-$, (d) $Ti_5NbO_{14}^{3-}$, (e) $Ti_{0.91}O_2^{0.36-}$, (f) $Nb_3O_8^-$ nanosheets. Reproduced with permission from ref. 199. Copyright 2012, American Chemical Society.

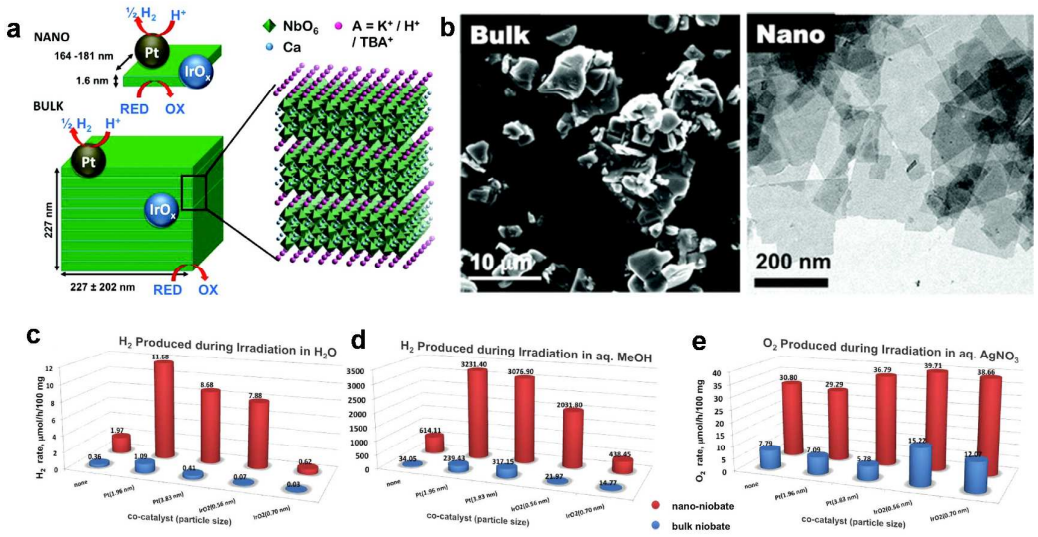

Figure 16. (a) Bulk niobate $KCa_2Nb_3O_{10}$ consists of sheets of corner-shared NbO_6 octahedra with intercalated Ca^{2+} ions that are held together by the layers of K^+ ions. Exfoliation with TBA^+ (tetrabutylammonium) produces the nanoniobate as individual nanosheets. Both niobates are functionalized with photodeposited Pt or IrO_x nanoparticles to serve as active sites for H_2 and O_2 production, respectively. (b) SEM and TEM micrographs of bulk and nanoniobate. (c) H_2 evolution rates from catalysts in H_2O, (d) H_2 evolution rates in aqueous MeOH, and (e) O_2 evolution rates in aqueous $AgNO_3$. Reproduced with permission from ref. 201. Copyright 2012, American Chemical Society.

Comprehensive studies of photocatalytic properties under various conditions are always important for the rational design of 2D photocatalysts. A detailed study into the effects of nanoscaling, sacrificial charge donors, co-catalysts, and co-catalyst deposition conditions on the photocatalytic hydrogen and oxygen generation activity of TBA-supported $HCa_2Nb_3O_{10}$ nanosheets together with their parent phase $KCa_2Nb_3O_{10}$ (structure and morphology shown in **Figure 16a** and **b**) was conducted

by Sabio *et al*.[201] Under all conditions with and without a co-catalyst and sacrificial agents, the nanosheets exhibited a much higher activity in generating hydrogen or oxygen than the bulk, as shown in **Figure 16c-e**. The kinetic model suggests that the superior activity of the nanosheet is due to shortened transport paths for electrons and holes to the reactive surface, which reduce lattice recombination. This effect outweighs the increase in surface recombination because of the increased specific surface area. It is concluded that both the kinetics of the redox reactions and the rate of charge transport to the water−catalyst interface instead of mass transport and surface recombination are dominant in controlling the activity of the nanosheets.

The dependence of photocatalytic activity on the band edge potentials of the nanosheets has been demonstrated by comparing the photocatalytic hydrogen evolution from a mixture of methanol and water with a group of eight restacked perovskite nanosheets of $HCa_{2-x}Sr_xNb_3O_{10}$ and $HCa_2Nb_{3-y}Ta_yO_{10}$ with tunable conduction band-edge potentials[67]. It was found that three types of nanosheets containing tantalum atoms greatly outperform other five kinds of nanosheets without tantalum atoms due to their much larger bandgaps and more negative conduction band potentials in the former materials. The most active sample $HCa_2Nb_2TaO_{10}$ with 0.5 wt% Pt co-catalyst gives a maximum AQY of 80%, which is the highest value reported for nanosheet-based photocatalysts. This is attributed to the nanosized thickness which enables prompt migration of the photogenerated charge carriers to the surface and a sufficiently negative conduction band edge potential which provides a strong driving force for proton reduction.

Overall water splitting for photocatalytic solar energy conversion that releases hydrogen and oxygen in a stoichiometry of 2:1 must be achieved without any sacrificial agents, but only a very limited number of semiconductor photocatalysts can do this. Several studies have focused on the splitting of water using niobate-based nanosheets as photocatalysts without adding sacrificial agents. $Ca_2Nb_3O_{10}$ nanosheets with and without co-catalyst Pt have the ability to induce photocatalytic hydrogen evolution from pure water, but no oxygen evolution is obtained[163]. The highest quantum efficiency of 3.49% is observed for a structure with Pt directly grown onto the nanosheets. The adsorption of oxygen on the photocatalyst surface is proposed to be the reason for the absence of oxygen evolution[202]. A further study by Compton *et al.* showed that TBA-stabilized $Ca_2Nb_3O_{10}$ nanosheets photocatalytically split water into hydrogen and hydrogen peroxide stoichiometrically. The H_2O_2 molecules formed are adsorbed on the nanosheet surface by coordinating as a side-on ligand with the surface Nb^{5+} ions[203]. The high stability of the Nb-peroxide bond seems to be the reason for the inability of the nanosheets to evolve O_2 under UV light irradiation. However, other possible reasons that need to be carefully investigated are the presence of some residual TBA^+ ions attached to the nanosheets as a sacrificial agent that consume the photogenerated holes and the bi-directional catalysis role of Pt in inducing the reduction of oxygen.

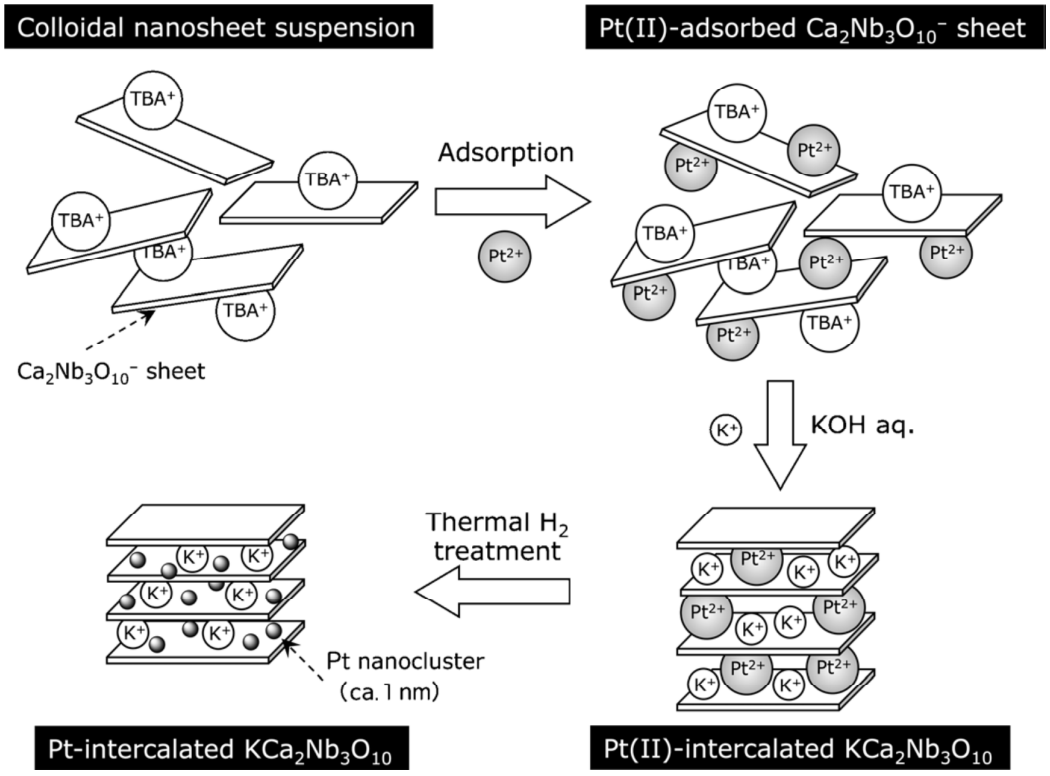

Figure 17. Preparation of Pt-intercalated $KCa_2Nb_3O_{10}$ nanosheets through electrostatic attraction between a cationic complex and anionic nanosheets [TBA^+ indicates tetra(n-butyl)ammonium cation]. Reproduced with permission from ref. 200. Copyright 2015, John Wiley and Sons.

It is encouraging that aggregates of RuO_x-loaded $Ca_2Nb_3O_{10}$ restacked with K^+ and Na^+ showed the ability of overall water splitting[204]. In contrast, bulk $KCa_2Nb_3O_{10}$ loaded with RuO_x by a conventional impregnation procedure showed only H_2 but no O_2 evolution. The high dispersion of RuO_x nanoparticles in the restacked agglomerates is considered to be responsible for the overall stoichiometric water splitting. A high dependence of overall water splitting on the alkali metal ions used to restack the nanosheets has been observed. Na^+-based agglomerates exhibit a higher activity than do K^+-based agglomerates (118 versus 96 μmol h^{-1} of H_2 generation)

while the molar ratio (23:7.7) of H_2 to O_2 for Li^+-based agglomerates is far from the stoichiometric ratio. A lower hydration tendency has been proposed to be the possible reason for this. A further study by Oshima *et al.* demonstrated an 8x higher photocatalytic overall water splitting activity for exfoliated and restacked $KCa_2Nb_3O_{10}$ modified with Pt clusters smaller than 1 nm diameter in their interlayer spaces than that modified with RuO_x particles[205]. The introduction of electron-deficient Pt nanoclusters, that are considered to play a role in collecting the photogenerated electrons, was realized by the electrostatic interaction between a cationic metal complex $[Pt(NH_3)_4]Cl_2$ and a negatively charged two-dimensional $Ca_2Nb_3O_{10}^-$ nanosheet and subsequent restacking and thermal hydrogen treatment, as shown in **Figure 17**. Although these clusters tend to aggregate in a long-term photocatalytic water splitting test of 30 h, no activity degradation was observed. The AQY in the steady-state was estimated to be about 3% at 300 nm, which was reported to be the highest efficiency for nanosheet-based photocatalysts. These results demonstrate the great significance of the exfoliation-restacking processes of layered metal oxides in constructing efficient photocatalysts for overall water splitting by dispersing suitable ultra-small nanoparticle co-catalysts in the interlayer spaces of the agglomerates.

In addition to the metal oxide nanosheets exfoliated from layer materials discussed above (the top-down strategy), nanosheets of many materials including binary oxides (i.e., ZnO,[72] WO_3,[61] SnO[63]) and ternary oxides (i.e., $Ba_5Nb_4O_{15}$,[82] $La_2Ti_2O_7$,[33] Bi_2WO_6,[44, 88] $FeVO_4$,[71] $ZnGa_2O_4$[65]) have also been synthesized by the bottom-up

strategy. The combination of these two strategies leads to a huge number of 2D materials of semiconducting oxides. One early representative sample of the bottom-up synthesis of 2D photocatalysts is the hydrothermal synthesis (the most widely used method for 2D materials) of the monomolecular-layer perovskite $Ba_5Ta_4O_{15}$ nanosheets with hexagonal structure[206]. The nanosheets have a dominant thickness of 1.08 nm, which is very close to the *c*-axis lattice parameter (c = 1.3 nm). It is surprising that the bandgap of the nanosheets is smaller than that of the bulk of $Ba_5Ta_4O_{15}$ (3.75 versus 4.1 eV), which is contrary to the usual bandgap enlargement resulting from the quantum size effect. These 2D nanosheets show good separation of photo-generated charge carriers and have abundant reactive sites resulting in a much superior activity in photocatalytically decomposing Rhodamine B than the bulk photocatalyst. Recent progress of other oxide nanosheets consistently shows the result of the much superior photocatalytic activity of the nanosheets than the bulk.

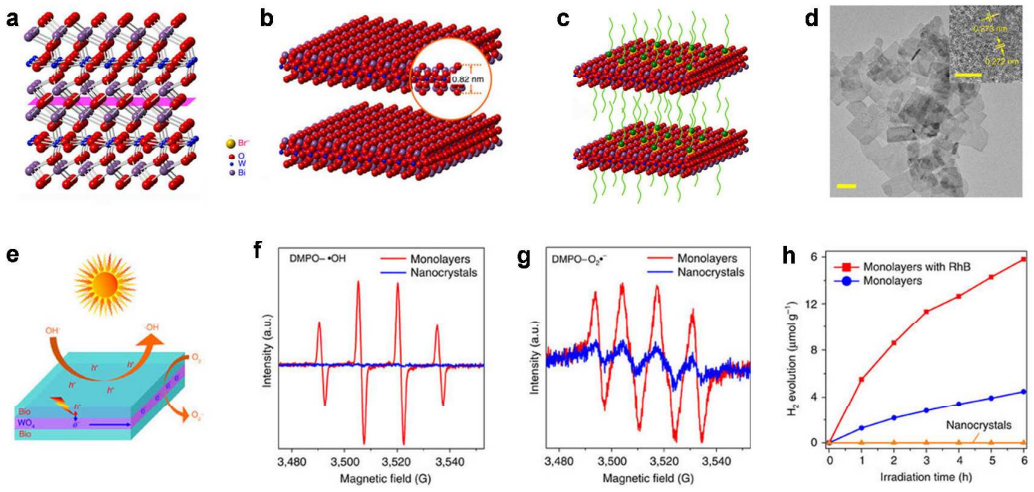

Figure 18. Synthesis of monolayer Bi_2WO_6. (a) Crystal structure of Bi_2WO_6. (b)

Structure of pristine monolayer Bi_2WO_6. (c) Formation mechanism of monolayer Bi_2WO_6 with CTAB assistance. (d) TEM image of the synthesized Bi_2WO_6 with Br- ions assistance; inset is the corresponding HRTEM image. Photocatalytic performances of Bi_2WO_6 samples. (e) Schematic illustration of photocatalytic mechanism over the monolayer Bi_2WO_6. (f, g) Electron spin resonance signals of DMPO-•OH^- adducts and DMPO-O_2•$^-$ adducts produced by Bi_2WO_6 samples under visible light irradiation ($\lambda \geq 420$ nm). (h) Visible-light-driven photocatalytic H_2 evolution over nanocrystals, monolayers and RhB sensitized monolayers ($\lambda \geq 420$ nm); 0.3 wt% of Pt was loaded. Reproduced with permission from ref. 88. Copyright 2015, Springer Nature

Compared to oxides with a bandgap of > 3 eV, which are responsive only to UV light, the oxides with a smaller bandgap allow visible light absorption. Monolayer Bi_2WO_6 with a sandwich substructure of $[BiO]^+$–$[WO_4]^{2-}$–$[BiO]^+$, which may also be considered as a layered heterojunction with different monolayer oxides as indicated in **Figure 18a** and **b**, was prepared by a cetyltrimethylammonium bromide (CTAB)-assisted hydrothermal bottom-up route[88]. The strong adsorption of Br^- ions from CTAB on the monolayers surfaces makes the monolayers negatively charged, which effectively blocks their stacking by Coulombic repulsion forces and the hydrophobic chains of CTA^+ ions (**Figure 18c**). The synthesized monolayer has a thickness of around 0.8 nm, which is close to that of a monolayer Bi_2WO_6 sheet along [001] direction. Remarkably, the adsorbed Br^- ions can produce a smaller bandgap of 2.7 eV by elevating the valence band so that a wider visible light absorption range can

be utilized. Equally important, the $[BiO]^+$–$[WO_4]^{2-}$–$[BiO]^+$ sandwich substructure of monolayer Bi_2WO_6 simulates a heterojunction interface with a space charge that promotes the spatial separation of the photogenerated electrons and holes in the interface, as shown in **Figure 18e**. Thanks to the broader visible light absorption, promoted charge separation, and abundant surface reactive sites, monolayer Bi_2WO_6 used as a photocatalyst shows a remarkably improved photocatalytic activity in generating •OH radicals and O_2^-, and hydrogen from an aqueous solution containing ethylenediamine tetraacetic acid as a sacrificial reagent under visible light (**Figure 18f-h)**. Other visible light responsive oxide nanosheets include $SnNb_2O_6$[100], SnO[63], $BiVO_4$[34], Cu_2O[59], and WO_3[61].

4.2. Porous 2D light absorbers

Mesoporous single crystal particles provide both a highly accessible surface and long-range electronic connectivity and structural coherence that are required in many applications. Such particles of oxide and nitride based photocatalysts can be prepared by seed-template and template free routes. For example, Crossland *et al.* developed a new method to grow semiconductor mesoporous single crystals of anatase TiO_2 using seeded nucleation and growth inside a mesoporous template immersed in a dilute reaction solution[207]. The porous single crystal films produced had mobility values over an order of magnitude higher than those of nanoparticle films over a broad range of charge densities. This synthesis method has been used to produce mesoporous single crystals of several metal oxides including rutile TiO_2,[208, 209] and Fe_2O_3,[210] for photo(electro)catalysis applications. In contrast to the seeded-template synthesis

routes, template-free routes have the merits of scalability and low cost. Volume shrinkage of the materials after the phase transition can lead to the formation of abundant pores throughout crystals. Typical examples include the formation of porous single crystalline $LaTiO_2N$ plates from solid $La_2Ti_2O_7$ plates in a flux of gaseous ammonia at 950 ^oC[211], and porous perovskite $PbTiO_3$ fibers from solid pre-perovskite $PbTiO_3$ fibers in air at 600 ^oC[212]. Some unique strategies have also been developed to produce porous photocatalysts. Based on the stability difference of different bonds (chemical interactions) in a material, the selective breaking of weaker bonds by thermal treatment can be used to induce the formation of pores. A typical example is the formation of porous g-C_3N_4 by selectively breaking hydrogen bonds of bulk g-C_3N_4[138]. All these porous bulk photocatalysts exhibit a higher photocatalytic activity than their non-porous counterparts. These strategies developed to produce porous bulk material can also be used to produce porous 2D materials for photocatalysts.

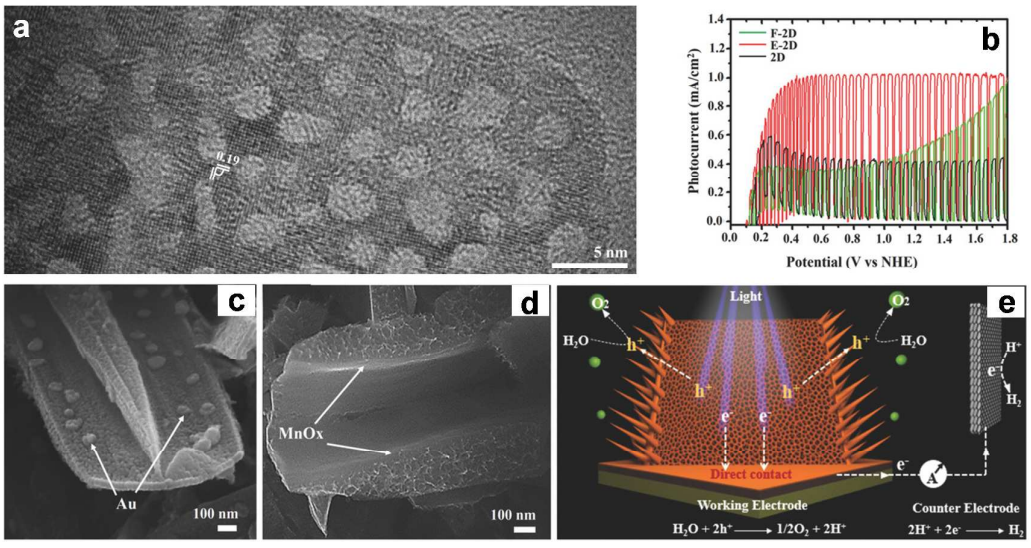

Figure 19. (a), HRTEM images of a branch and backbone plate of anatase TiO_2; **(b)**,

Photocurrent density versus applied potential curves for 2D, E-2D, and F-2D films. **(c, d)** Active site distribution in the non-branched 2D single-crystal structure indicated by the location of photodeposited Au and MnO_x particles. **(e)** Diagram illustrating the working mechanism of E-2D photoelectrode–based PEC water splitting. Reproduced with permission from ref. 213. Copyright 2018, John Wiley and Sons.

The introduction of pores in 2D nanosheets is very attractive because they increase the exposure of atoms to reactants and shorten the diffusion length of the photo-excited charge carriers to reach the surface. Moreover, the porous 2D structure can cause the increase of the edges or corners that are usually catalytically active sites. These advantages of porous nanosheets as active light absorbing materials for solar water splitting, which not only limit to powder formed photocatalsis, but also thin film photoelectrocatalytic process, are evident from the following representative results. Butburee *et al.* prepared porous single crystal array films of anatase TiO_2 (**Figure 19a**) on FTO substrates, using a one-pot hydrothermal reaction and subsequent ion exchange/thermal dehydration–induced pore-forming processes[213]. The resultant nano-branched 2D porous backbone plate was used as photoanode for photoelectrochemical water oxidation and delivered a photocurrent of 1.02 mA cm^{-2} at a very low potential of 0.4 V versus a reversible hydrogen electrode (RHE), close to the theoretical value of TiO_2 (1.12 mA cm^{-2}). Moreover, the current–potential curve has a small potential window from 0.1 to 0.4 V versus RHE under one-sun illumination, and has the near-ideal shape predicted by the Gartner Model. The excellent performance is attributed to the efficient spatial separation of

photogenerated electrons and holes between the basal planes and edges of the plates and a surface reaction, as indicated in **Figure 19c-e**. The synthesis strategy developed in this study might be applicable to the formation of porous single crystals of other metal oxides from their protonated metal oxides.

Porous nanosheets of some other metal oxides have also been developed. For example, single-crystal ZnO porous nanosheets with {0001} polar facets, prepared by a templating method, can not only accelerate the hole-electron separation and electron transport because of their being single-crystals, but can also enhance the selective adsorption of organic molecules owing to the porous structure and the exposed {0001} polar facets with more O-termination (000-1) surfaces[214]. In addition to the obvious role of nanopores in promoting charge separation and providing abundant reactive sites, the pores in the nanosheets can also modify the optical absorption range. Wang *et al.* found that Bi_3NbO_7 nanosheets with pores have a smaller bandgap than those without pores[94]. It was proposed that the different edges, angles and facets of the pores compared to single crystal nanosheets without pores are responsible for the wider absorption spectra. Another example is BN porous sheets with a large number of exposed (002) plane edges (functionalized with hydroxyl groups) exhibit wide-spectrum light absorption in both the UV and visible light ranges. Theory shows that the narrower HOMO–LUMO band-gaps of –OH edge-terminated BN nanoribbons than those of h-BN and –H terminated analogs[215] is the reason for the visible light absorption in the yellow region. Moreover, the coupling of porous BN sheets with TiO_2 nanoparticles leads to a strong visible light absorption band of the

BN/TiO_2 hybrid,[216] which shows photocatalytic activity under visible light irradiation. A number of possible reasons have been proposed to explain the increased visible light absorption in porous nanosheets, including defects and strains, which can also be produced during the formation of the pores.

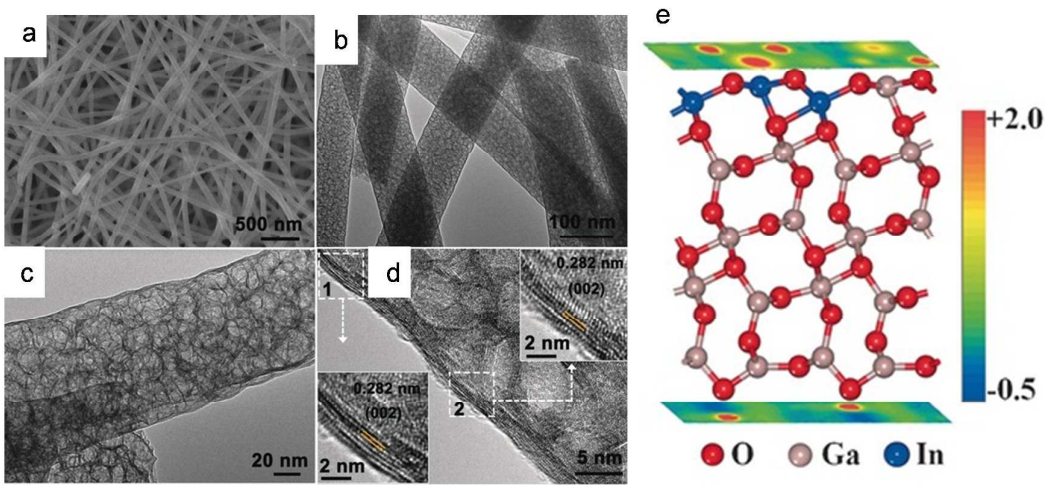

Figure 20. a) SEM image, b), c) TEM images, and d) HRTEM images of $Ga_{1.7}In_{0.3}O_3$. e) Electrostatic potentials of the top and bottom surfaces of b-$Ga_{1.7}In_{0.3}O_3$. Reproduced with permission from ref. 217. Copyright 2016, John Wiley and Sons.

Different from the 2D binary oxide nanosheets considered above, the porous Ga-In oxide nanofibers with atomically thin pore walls in **Figures 20a-d** were prepared by electrospinning followed by thermal treatment[217]. It was theoretically shown that these nanofibers have an unprecedented electronic structure arising from their ultrathin walls, so that the conduction band bottom and the valence band top are on two opposite surfaces separated with a small electrostatic potential difference, as indicated in **Figure 20e**. This feature not only shortens the distance of the photogenerated charge carriers from the reactive sites, but also promotes their spatial

charge separation in the nanofibers. As a consequence, these nanofibers with no additional HER co-catalyst have a multifold increase in photocatalytic hydrogen generation from the mixture of aqueous solution of methanol compared to their bulk counterpart, suggesting the great potential of using atomically thin porous nanosheets to construct efficient photocatalysts.

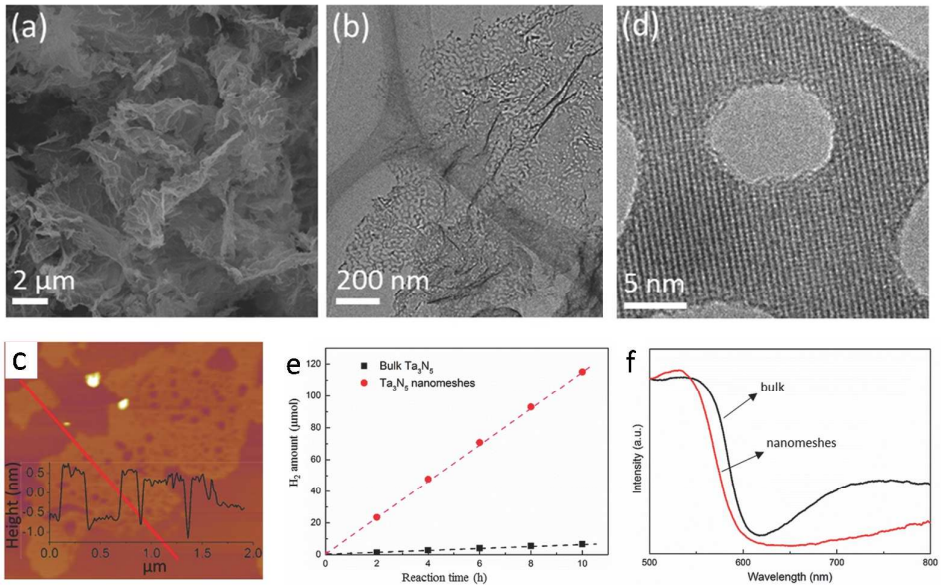

Figure 21. a, b, d) SEM, TEM, and HR-TEM images of ultrathin Ta_3N_5 nanomeshes. f) AFM image and height profile of the Ta_3N_5 nanomeshes. e) Photocatalytic H_2 evolution activity of bulk Ta_3N_5 and Ta_3N_5 nanomeshes under simulated sunlight irradiation (AM 1.5G, 100 mW cm^{-2}). 0.02 g of photocatalysts were loaded with 1 wt% Pt in 10 vol% methanol aqueous solution. b) UV–visible light absorption spectra. Reproduced with permission from ref. 218. Copyright 2017, John Wiley and Sons.

Due to the higher energy level of N 2p than O 2p states, nitride semiconductors usually have a smaller bandgap than their oxide counterparts. Among them, tantalum nitride Ta_3N_5 with a bandgap of ~2 eV has been considered to be an efficient light

absorber for photocatalytic water splitting because it has excellent light harvesting and appropriate band edges for water splitting. However, the material always suffers from serious drawbacks of low carrier mobility (1.3–4.4 cm^2 V^{-1} s^{-1}) and fast carrier recombination (<10 ps), as a result its activity is extremely low. The 2D structure addresses these problems. An innovative strategy using graphene oxide as a template was developed by Xiao *et al.*[218] to synthesize ultrathin Ta_3N_5 single crystal nanosheets with a thickness of around 2 nm, specific surface area of 284.6 m^2 g^{-1} and pores of 2-5 nm diameter, as shown in **Figure 21a-d**. The hydrogen evolution rate of Ta_3N_5 nanomeshes with Pt as a co-catalyst under AM 1.5G simulated sunlight is 10x higher than that of bulk Ta_3N_5 (**Figure 21e**). The apparent quantum efficiency of the Ta_3N_5 nanomeshes under 450 nm light irradiation was estimated to be 0.53%. The photodeposition of Pt on them shows a uniform distribution of Pt nanoparticles on the whole surface and also the edges, suggesting abundant reactive sites for the HER reaction. Equally important, compared to the bulk, the blue-shift of the absorption edge of the nanomeshs caused by quantum size effects (**Figure 21f)** means an enlarged bandgap for the stronger redox energy of electrons and holes.

4.3. Heteroatom & defect modified 2D light absorbers

As discussed, most metal oxides with suitable band structures for photocatalytic water splitting are only UV active due having bandgaps > 3 eV. As a result of the quantum size effect their 2D structures have an even narrower light response range. On the other hand, many materials even with 2D structures are photocatalytically

inactive due to their unfavorable intrinsic atomic structures. Introducing heteroatoms and/or defects is the most commonly used method to address the challenge by changing the electronic band structures and surface atomic structures. In some cases, the heteroatoms and defects themselves (or their local regions) convert the materials into co-catalyst-free photocatalysts for solar fuel generation. Despite the abundant information obtained from heteroatom/defect-modified bulk photocatalysts, our understanding of the phenomenon is still in its infancy. One of the most distinct differences between the modifications of bulk and 2D structures by heteroatoms/defects might be that the heteroatoms/defects exert a stronger influence on the ultrathin 2D structure because most of its atoms are exposed. In contrast, the extent to which they can exert their influence in a bulk material is highly dependent on their spatial distribution.

As shown in Section 4.1, the exfoliated 2D nanosheets of most metal oxides have a large bandgap > 3 eV. And introducing suitable anion dopants, particularly nitrogen, is an effective way of modifying their band structures. Thanks to the layer structure of their parent materials, which can be homogeneously doped with anions, homogeneous anion-doped metal oxide nanosheets can be easily produced. The first study on this topic was conducted by Liu *et al*. Homogeneous nitrogen doping in layer-structure cesium titanate leads to an extraordinary band-to-band redshift of the absorption edge from 356 to 472 nm (**Figure 22a)** as a result of the bandgap narrowing[132]. The exfoliation of the homogeneously nitrogen doped protonated titanate produces nitrogen-doped titania ($Ti_{0.91}O_{2-x}N_x$) nanosheets with a yellow color[35]. In contrast to

the band-to-band visible light absorption spectrum of the nitrogen-doped titanate, only a shoulder-like visible light absorption band up to 450 nm (**Figure 22b**) occurs in the $Ti_{0.91}O_{2-x}N_x$ nanosheets, indicating that the bandgap is not really narrowed but that some nitrogen dopant-related states are formed in the bandgap. Based on XPS data, the amount of the substitutional nitrogen in the nanosheets is comparable to that in the parent titanate so homogeneous nitrogen doping occurs in both the titanate particles and nanosheets. The substantial change of the optical absorption of the doped titanate before and after exfoliation must be caused by the disruption of long-rang interactions between nitrogen atoms in the titania layers of the parent material. This is validated by the fact that nitrogen doping in H-restacked Nb-O based nanosheets (the substitutional nitrogen content is about 3% of all O atoms) can only cause a shoulder-like absorption band in the visible light region[36]. In addition, the photo-nitrogen doping process developed in this study is unique. The photogenerated charge carriers in H-restacked Nb-O nanosheets containing TBA in the absence of oxygen leads to the decomposition of TBA to induce nitrogen doping in the randomly stacked nanosheets. It is recognized that the sufficiently high conduction band edge of the Nb-O nanosheets plays an essential role in enabling nitrogen doping by generating electrons with a sufficiently strong reductive power. The photo-nitrogen doping process is not possible for Ti-O nanosheets with a conduction band edge that is not high enough.

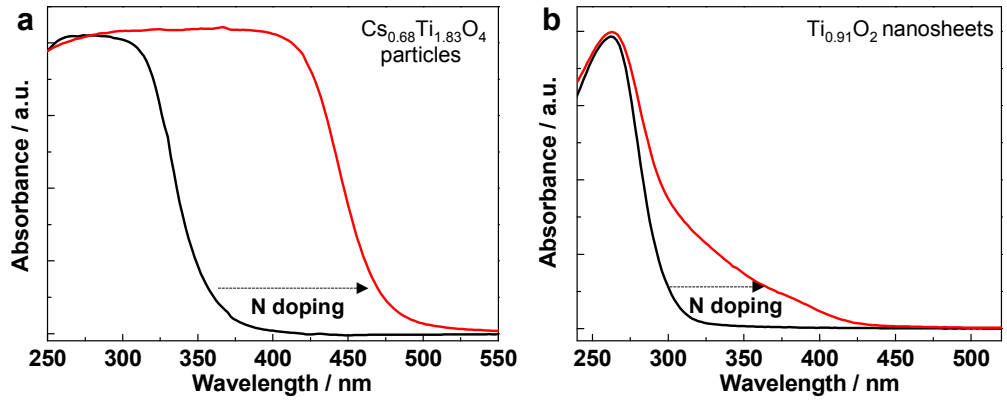

Figure 22. (a), UV-visible absorption spectra of $Cs_{0.68}Ti_{1.83}O_4$ particles before and after homogeneous nitrogen doping. Reproduced with permission from ref. 132. Copyright 2009, American Chemical Society. **(b)** UV-visible absorption spectra of $Ti_{0.91}O_2$ nanosheets exfoliated from protonated $Cs_{0.68}Ti_{1.83}O_4$ particles with and without homogeneous nitrogen doping. Reproduced with permission from ref. 35. Copyright 2009, Royal Society of Chemistry

Nitrogen-doped nanosheets of calcium tantalum oxynitride $[Ca_2Ta_3O_{9.7}N_{0.2}]^-$, prepared by exfoliating a layered perovskite oxynitride ($CsCa_2Ta_3O_{9.7}N_{0.2}$) by proton exchange and two-step intercalation, show some interesting optical properties and photocatalytic activities[38]. Compared to the strong visible light absorption band of their layer-structure parent oxynitride, the nanosheet suspension has a much lower absorbance in the visible light region due to the lower concentration of the nanosheets than in the bulk material. The nanosheets obtained by drying the suspension have an increased absorbance in the visible light region that is still lower than that of the bulk material. Note that the absorbance of the nanosheet suspension and dried nanosheet powder in the UV region below 300 nm, which is the excitation of the O 2*p* orbital to

the Ta 5*d* orbital, is very close to that of their parent material. This again suggests the lack of a long range interaction of nitrogen dopant atoms in the nanosheets so that only a narrow sub-band consisting of N 2p states is formed in the bandgap to enable low absorbance in the visible light region. Because of their small thickness and anisotropy, the nanosheets have photocatalytic activity for H_2 evolution from water under visible light irradiation. In contrast, $CsCa_2Ta_3O_{9.7}N_{0.2}$ exhibits a very low photocatalytic activity for H_2 evolution under visible light, even with methanol as a sacrificial agent. However, when these same nanosheets are loaded with Rh and H-restacked, after a 42 h UV-light exposure to remove surface organic species, they show photocatalytic activity for H_2 and O_2 evolution from pure water under UV-light irradiation, although the ratio of evolved H_2/O_2 is around 3 (probably because of the side reactions, including the decomposition of organic species). However, no visible light photocatalytic H_2 and O_2 evolution from pure water was seen, probably because of the lack of band-to-band visible light absorption in the restacked nanosheets[38]. In addition, black $Ca_2Nb_3O_{10-x}N_y$ nanosheets were obtained by exfoliating the parent layer-structure $KCa_2Nb_3O_{10-x}N_y$[47], and ultrathin nitrogen-doped perovskite nanosheets $LaTa_2O_{6.77}N_{0.15}$[-] with strong visible light absorption were prepared by exfoliating Dion−Jacobson-type layered perovskite $RbLaTa_2O_{6.77}N_{0.15}$[219].

The doping of some free-standing nanosheets also leads to an expansion of the light absorption range. Typical examples are as follows. Approximately 15 nm thick single crystal nanosheets of $La_2Ti_2O_7$ with the perovskite structure showed a band-to-band redshift of the absorption edge from 378 to 495 nm after nitrogenation,[39]

demonstrating the advantage of using ultrathin nanosheets for the doping. Based on sub-nanopore engineering using molecular titanium-oxide incorporation, as shown in **Figure 23a**, the electronic band structure of 2D graphitic carbon nitride nanosheets with a thickness of 3-3.3 nm (**Figure 23b**) can be tuned to produce increased visible light absorption (**Figure 23c**). The resultant material showed improved separation and migration rates of the photo-excited charge carriers, leading to a significantly improved photocatalytic activity under visible light irradiation [93]. Note that only an additional shoulder-like absorption band is formed by incorporating different amounts of molecular titanium-oxide in the nanosheets. The possible reason for this may be the lack of the long-rang interaction of Ti atoms perpendicular to the nanosheets. Similarly, iodine-doped graphitic carbon nitride nanosheets with a thickness of around 2 nm, where the iodine atoms replace nitrogen atoms, also have an additional shoulder-like absorption band between 450 and 650 nm[220]. Boron is an effective dopant for modifying the electronic structure of photocatalysts, including carbon nitride. The replacement of a small number of carbon atoms with boron atoms causes a slight decrease of the bandgap by 0.05 eV, but greatly increases the absorbance, which enhances visible light photocatalytic hydrogen generation[49]. Carbon-doped carbon nitride nanosheets can also be produced by the copolymerization of dicyandiamide with barbituric acid (BA) and by increasing the amount of BA in the precursor mixture, the absorption edge of the carbon nitride gradually shifts from 470 to 750 nm as a result of the respective shifts of the conduction and valance bands down and up. This study strongly indicates the importance of controlling intrinsic

defects (or self-doping) of the nanosheets to achieve high performance[221].

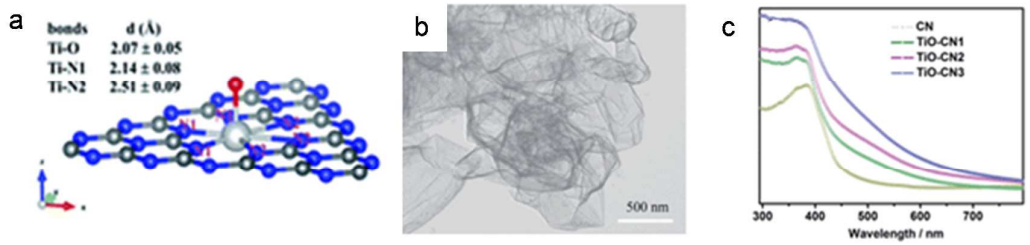

Figure 23. a), Details of the TiO–CN structure. **b)**, TEM image of a TiO–CN_2 nanosheet. **c),** UV-visible absorption spectra of 2D CN and TiO–CN. Reproduced with permission from ref. 220. Copyright 2016, Royal Society of Chemistry.

Beside carbon nitride nanosheets, Huang *et al.* have developed polycrystalline carbon doped boron nitride (BCN) nanosheets with a thickness of around 3-4 nm (**Figures 24a-c**)[75]. The ternary nanosheets have a highly delocalized 2D electron system with sp^2 carbon incorporated in the *h*-BN lattice, where the bandgap can be adjusted by the amount of the incorporated carbon to produce unique features (**Figures 24d** and **e**). The incorporation of carbon in the h-BN layers smears out the Raman signals of h-BN due to the distortion of the layer symmetry (**Figure 24f**). These BCN nanosheets have the ability to induce photocatalytic hydrogen generation under visible light ($\lambda > 420$ nm) without an additional co-catalyst. With the assistance of a Ni-Co layered double hydroxide, the BCN nanosheets induce water oxidation to release oxygen under visible light. Moreover, the nanosheets also showed the ability to photocatalytically reduce CO_2 to CO using visible light, which was confirmed by isotopic experiments. This new metal-free 2D

photocatalyst with tunable optical and surface properties may find potential uses in many areas, from artificial photosynthesis to organocatalysis by further optimizing their local structures.

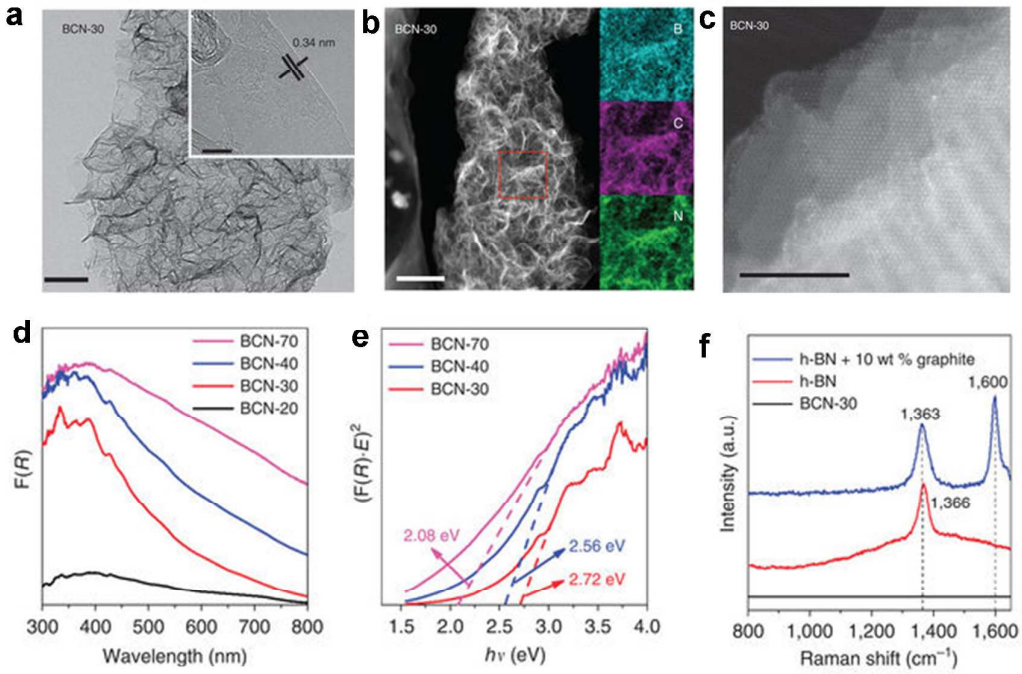

Figure 24. (a) HRTEM image of the BCN-30 sample. Scale bar, 100 nm, inset scale bars, 5 nm. (b) Typical TEM dark-field image of BCN-30 sample and the elemental mapping images of B, C and N of the enlargement of selected-area in the picture. Scale bar, 300 nm. (c) High-resolution STEM of the BCN-30 sample along (002) facet. Scale bar, 5 nm. (d) ultraviolet–visible diffuse reflectance spectra (UV–vis DRS) of the BCN-*x* samples and (e) bandgap determination of the BCN-*x* samples from the $(F(R)\cdot E)^n$ versus *E* plots. (f)**,** Raman spectra of h-BN, BCN-30 and a physical mixture of h-BN and graphite. Reproduced with permission from ref. 75. Copyright 2015, Springer Nature.

As well demonstrated in bulk photocatalysts, heteroatoms can affect the charge separation of 2D photocatalysts because the entire ultrathin nanosheet with an extremely large surface area can be substantially changed. Despite a slight change in the bandgap, the replacement of sulfur with oxygen (4.4 at%) in $ZnIn_2S_4$ nanosheets causes an upward shift of the edges of the conduction and valence bands. As a result, the photo-generated electrons have increased power for proton reduction[98] and the increased density of states at the valence band maximum guarantees more photogenerated charge carriers and their longer average recovery lifetime to promote their separation thus favoring efficient photocatalysis. As a result of these features, the oxygen-doped nanosheets with no additional co-catalyst exhibit a stable and enhanced photocatalytic activity with a hydrogen-evolution rate of 2120 μmol h^{-1} g^{-1}, which is 4.5x higher than that of undoped nanosheets under the same conditions. Co-doping in three atomic layer In_2S_3 also results in similar positive effects by increasing the charge carrier concentration by a factor of 3 and the average recovery lifetime by 25x compared to non-doped layers[77]. A photoanode of Co-doped nanosheets has a one order magnitude higher photocurrent than that of undoped nanosheets under visible light.

Intentionally introducing suitable cation heteroatoms in the nanosheets to create reactive centers at the atomic scale is highly promising in terms of both improving catalysis activity and lowering the amount of noble metal co-catalyst used. A combination of pre-doping with such heteroatoms and subsequent exfoliation leads to the formation of cation-doped nanosheets. The merits of this route include the high

crystallinity of the resulting doped nanosheets with an atomic dispersion of dopant. By exfoliating $KCa_2Nb_{3-x}Rh_xO_{10-\delta}$, Rh-doped calcium niobate, nanosheets with a tunable amount of Rh up to x = 0.15 were obtained[37]. The replacement of Nb^{5+} with Rh^{3+} in the Rh-doped Ca-Nb-O nanosheets is confirmed by a binding energy shift of the Rh $3d^{5/2}$ and lattice expansion of the nanosheets. Further TEM observation reveals an atomic dispersion of Rh in the Rh-doped Ca-Nb-O nanosheets. In contrast, many fine particles, 2-5 nm in diameter, were deposited on 1 wt% Rh_2O_3-loaded nanosheets. The superiority of Rh doped Ca-Nb-O nanosheets for photocatalytic water splitting is clearly demonstrated in **Figure 25b**. The apparent quantum efficiency at 300 nm is as high as 65%. The proposed mechanism for this is given in **Figure 25a**, where the RhO_6 units in the top layer of the nanosheets act as the sites for proton reduction. The Rh-doped Ca-Nb-O nanosheets can be considered a photocatalyst containing a single atom Rh cocatalyst. This concept is generic and is also demonstrated by a study showing that isolated single-atom Rh dopants in titanium oxide nanosheets act as co-catalyst to promote photocatalytic hydrogen evolution from a methanol aqueous solution[37]. The hydrogen evolution rate of the Rh-doped nanosheets is around 1.5-fold of that of the RhO_x loaded nanosheets at their respective optimal concentrations of Rh (1.4 *versus* 4.6 for Rh/(Rh+Ti)). The isolated Rh atoms in the nanosheets instead of RhO_x clusters are confirmed by the brighter images of Rh atoms at Ti lattice sites in **Figures 26a** and **b** due to the much larger atom number of Rh than Ti. Based on the XANES and EXAFS data in **Figure 26d**, one can conclude that the chemical environments of the Rh species in both Rh-doped nanosheets and RhO_x-loaded

nanosheets are similar to that in Rh_2O_3 but Rh is slightly more oxidized in the Rh-doped case. Three vacancy-like defects are present in the Rh-containing region in **Figure 26c** probably because of the oxidation state difference between Rh^{3+} and Ti^{4+}. In addition, theoretical simulations suggest different surface adsorption behaviors of water on pristine and doped nanosheets.[222]

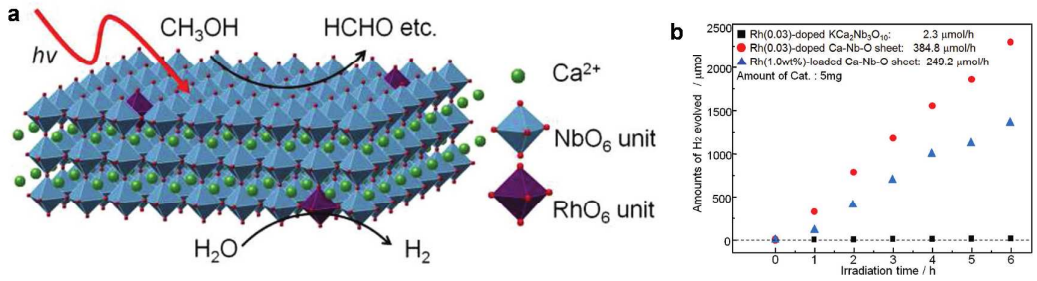

Figure 25. (a) Crystal structure of a Rh-doped calcium niobate nanosheet prepared by exfoliation of $KCa_2Nb_{3-x}Rh_xO_{10-\delta}$ and a model of the photocatalytic reaction in water/methanol. **(b),** Hydrogen evolution versus time over Rh(3.0 wt%)-doped Ca-Nb-O sheets, Rh(3.0 wt%)-doped $KCa_2Nb_3O_{10}$, and Rh(1.0 wt%)-loaded Ca-Nb-O sheet. Reaction conditions: 5 mg of catalyst, 150 cm^3 of aqueous 10 vol% methanol solution, 500 W Xe lamp. Reproduced with permission from ref. 37. Copyright 2013, American Chemical Society.

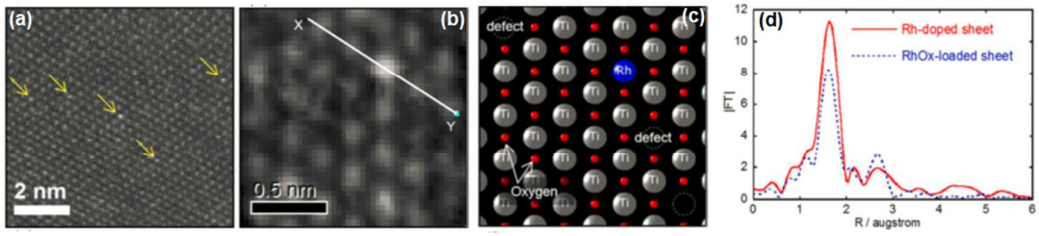

Figure 26. (a) HAADF-STEM (200 kV) image of a Rh (x = 0.026)-doped $Ti_{1.82-x}Rh_xO_4$ nanosheet, (b) magnified HAADF-STEM image (80 kV) of a Rh (x = 0.026)-doped nanosheet, (c) model of the structure expected from panel (b), (d)

Fourier transforms of Rh K-edge k^3-weighted EXAFS for Rh (x = 0.026)-doped and RhO_x-loaded titania nanosheets. Reproduced with permission from ref. 222. Copyright 2015, American Chemical Society.

Defects can play an equally important role in extending the absorption range and/or promoting the separation of photogenerated charge carriers in the nanosheets[223]. Oxygen vacancies can induce some localized states in the bandgap to capture photons with lower energies that are difficult to capture by the bandgap of pure semiconductors. They can also alter reaction kinetics by changing reaction barriers. A series of the oxide nanosheets with a large number of oxygen vacancies have been developed to boost photocatalytic activity. Taking advantage of an artificial hexagonal mesostructured In-oleate complex, Lei *et al.* synthesized In_2O_3 nanosheets containing oxygen vacancies with a thickness of around 0.9 nm that corresponds to the thickness of 5-atoms[62]. The vacancies produce a new donor level and an increased density of states for the nanosheets so that both the absorption range and separation of the charge carriers are improved. As a result, compared to a nanosheet-based photoanode containing few oxygen vacancies, that of one with many oxygen vacancies has a 2.5x increase in photocurrent density of 1.73 mA cm^{-2} under visible light. Oxygen vacancy-related levels are located 0.64 eV below the conduction band minimum. Excitation from the valence band to the defect levels or from the defect levels to the conduction band is responsible for the increased visible light absorption of nanosheets containing oxygen vacancies. Oxygen vacancies introduced in ~2 nm thick $K_4Nb_6O_{17}$ nanosheets without a co-catalyst significantly improve stable photocatalytic hydrogen

generation with a rate of 1616 μmol g^{-1} h^{-1} from a methanol/water mixture[224]. Although the important role of anion vacancies in improving photocatalysis activities of metal oxide nanosheets has been demonstrated, the fundamental understanding on local structures of anion vacancies is still rare in the literature and needs to be explored in much more details in further studies.

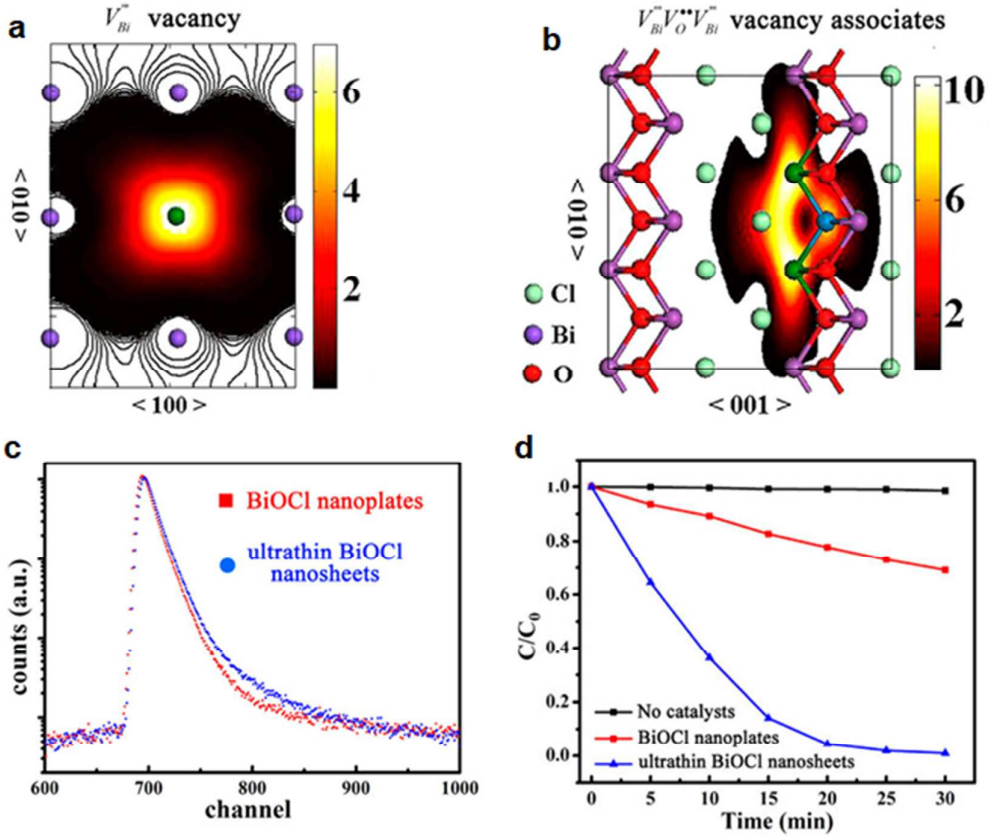

Figure 27. Positron annihilation spectroscopy of ultrathin BiOCl nanosheets and BiOCl nanoplates. (**a, b**) Schematic of trapped positrons for (a) a $V_{Bi}^{'''}$ defect and (b) $V_{Bi}^{'''}V_O^{\bullet\bullet}V_{Bi}^{'''}$ vacancy associates. **(c)** Positron lifetime spectrum of ultrathin BiOCl nanosheets and BiOCl nanoplates. **(d)** Comparison of the photodecomposition of Rhodamine B with ultrathin BiOCl nanosheets and BiOCl nanoplates under the

simulated solar irradiation. Reproduced with permission from ref. 45. Copyright 2013, American Chemical Society.

It is rare to have cation vacancies in most bulk n-type metal oxides, but several recent studies have reported their formation in ultrathin nanosheets. For example, the concentration of vanadium vacancies (V_V) in freestanding gram-scale single-unit-cell orthorhombic-$BiVO_4$ layers with an average 1.28 nm thickness can be changed by controlling the hydrothermal temperature[101]. A temperature of 160 ^oC leads to nanosheets with a large number of V_V's while a temperature of 120 ^oC leads to few V_V's. A combination of advanced characterization techniques as well as theoretical investigations consistently reveals increased photo-absorption, electronic conduction, and separation of the photogenerated charge carriers. Because of this, nanosheets with a large number of V_V's but without co-catalysts show an impressively stable activity of 98.3 μmol g^{-1} h^{-1} in reducing CO_2 to methanol under AM 1.5G simulated sunlight. An apparent quantum efficiency of 5.96% at 350 nm is reached. It is interesting to see how the type of Bi vacancy depends on the nanosheet thickness of BiOCl. As the thickness of nanosheets with a large percentage of exposed reactive {001} facets is reduced from about 30 nm to the atomic scale (around 2.7 nm), the bismuth vacancies evolve from isolated defects $V_{Bi}^{'''}$ to triple vacancy associates $V_{Bi}^{'''}V_O^{\cdot\cdot}V_{Bi}^{'''}$ (**Figures 27a and b**)[45]. As a result of the enhanced adsorption capability, effective separation of the photo-generated electron−hole pairs (**Figure 27c**) and more reductive photo-excited electrons resulting from the triple vacancy associates, the ultrathin

nanosheets have significantly improved photocatalytic activity under both UV and visible light irradiation (**Figure 27d**). Such cation defects in ultrathin nanosheets may open up new ways to develop highly efficient solar-driven photocatalysts. Further studies on the reason for the formation of the cation defects in ultrathin nanosheets are needed.

4.4. Hybrid 2D based light absorbers

The formation of heterostructures is also one of the most widely used strategies for increasing light absorption, and promoting the separation and directional transfer of photo-generated charge carriers. Besides the appropriate band alignments thermodynamically required in heterostructures, the interface between the components is critically important for the smooth transfer of the photo-generated charge carriers. Among the many heterostructure configurations, those formed by the face-to-face stacking of 2D materials clearly have the largest interfacial contact area. Moreover, the quality of the interfaces can be controlled by the crystallinity of the 2D materials used and the properties of the interface may be changed because of the many possible different properties of the available materials. Because of the large number of 2D materials already developed, the construction of a huge variety of hybrid layer structures,[91, 112, 225-234] particularly those held together by van der Waals (vdW) bonds, with unique functions is feasible, as illustrated in **Figure 28**[235]. Although the majority of 2D heterostructures has been constructed for condensed physics studies, recent work has shown their great potential for solar-driven photocatalysis applications. Some representative progress is highlighted below.

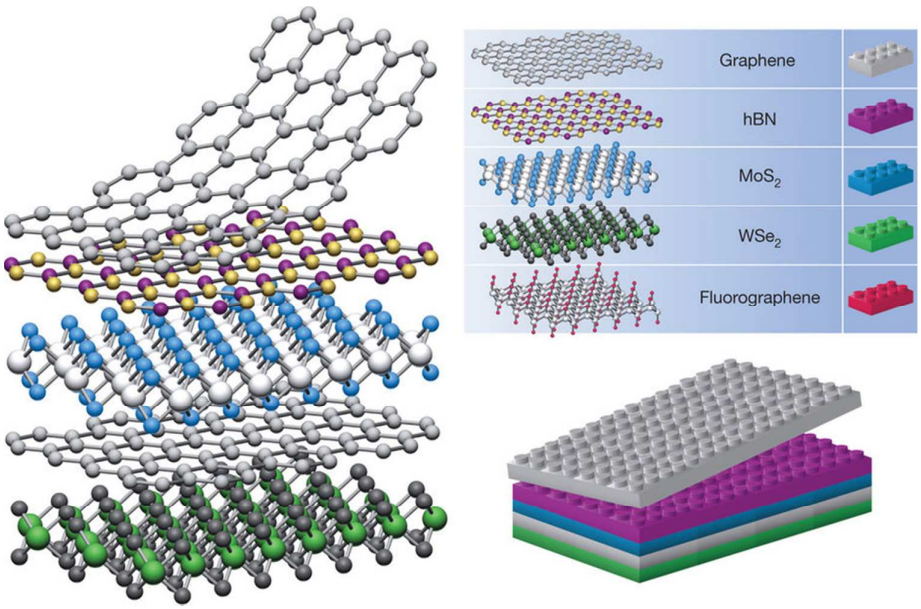

Figure 28. Building van der Waals heterostructures. If one considers 2D crystals to be analogous to Lego blocks (right panel), the construction of a huge variety of layered structures becomes possible. Conceptually, this atomic-scale Lego resembles molecular beam epitaxy but employs different 'construction' rules and a distinct set of materials. Reproduced with permission from ref. 235. Copyright 2013, Springer Nature.

Theoretical studies have predicted some very interesting features of vdW 2D heterostructures consisting of two monolayers as photocatalysts for water splitting. On the basis of the ~ 2% lattice mismatch between AlN (or GaN) and MoS_2 monolayers with the same hexagonal crystal structure, the formation of high-quality and intimate heterostructures is possible. Liao *et al.* predicted that a bilayer of MoS_2/AlN (or GaN) can separately produce hydrogen and oxygen at opposite surfaces, where photo-excited electrons transfer from AlN (or GaN) to MoS_2 during

photocatalysis, as shown in **Figure 29a**[236]. The calculated optical absorption spectra show significantly increased visible light absorption because the formation of the vdW heterostructure reduces the bandgap. Specifically, the bandgap of the MoS_2/AlN heterostructure is smaller than that of two separate monolayers (1.62 eV versus 1.92 eV for MoS_2 and 3.39 eV for AlN). Moreover, the negative formation energies indicate that MoS_2/AlN and MoS_2/GaN heterostructures are energetically favorable and should be easily obtained experimentally. Similar effects are also confirmed in other vdW heterostructures including the strained h-BN/ZrS_2 and g-C_3N_4/ZrS_2 heterostructures[231]. In addition, a bilayer of g-C_3N_4 is theoretically predicted to have a 0.8 eV smaller optical absorption threshold than the monolayer[237].

A surface-functionalized hexagonal boron-nitride bilayer (AB stacking) (**Figure 29b)**, whose two surfaces have been modified, one with fluorine and the other with hydrogen atoms, has been theoretically found to be active in inducing water splitting under near-infrared light[238]. This activity is attributed to the unique electronic structure of the modified bilayer, where the valence and conduction bands are located on the two opposite surfaces (F-BN and BN-H) with a large electrostatic potential difference produced by the intrinsic dipole of the bilayer. This surface potential difference effectively reduces the band gap required for water splitting in the infrared region. The good spatial dispersion of valence and conduction bands between the lower and upper BN layers facilitates the separation of photo-generated electrons and holes in the bilayer. The high thermal stability of the modified F-BNBN-H bilayer with its nearly perfect AB stacking interface makes preparation of the bilayer

experimentally possible.

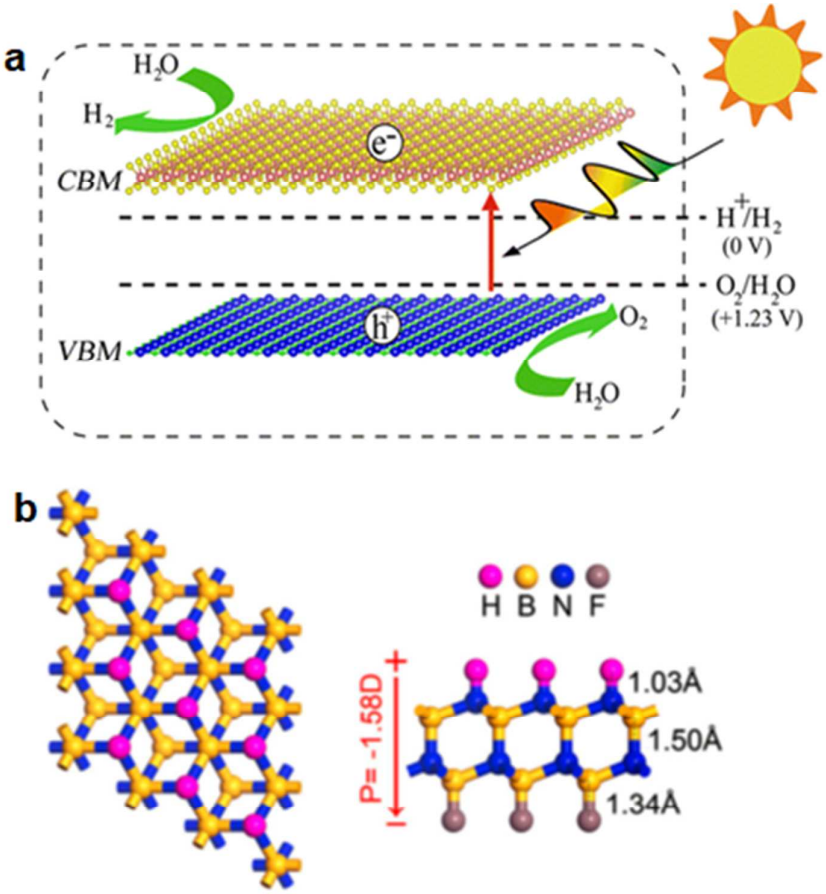

Figure 29. (a), Schematic of MoS_2/AlN(GaN) vdW heterostructures used as photocatalysts for water splitting, where VBM is the valence band maximum and CBM is the conduction band minimum. Reproduced with permission from ref. 236. Copyright 2014, American Chemical Society. (b). The optimized structure of F-BNBNH, top (left) and side (right) views. Reproduced with permission from ref. 238. Copyright 2014, American Physical Society.

As discussed above, a solid state Z-scheme heterostructure, consisting of two light absorbers and one electrically conductive mediator, has the outstanding merit of both utilizing the energetic photo-generated charge carriers and promoting their spatial

separation. Compared to photocatalysts consisting of a single light absorber, these heterostructures have the ability to achieve high-efficiency water splitting. However, the construction of such heterostructures remains challenging and only a limited number of such structures have been produced. 2D materials with good flexibility are excellent for constructing these heterostructures because not only do they make large interfacial contact possible but they also minimize lattice mismatch at the interfaces. A recent theoretical study[239] shows that graphene can be a good intermediate for the formation of a $MoSe_2$/graphene/HfS_2 heterostructure, where the $MoSe_2$ and HfS_2 monolayers act as the photocatalysts for HER and OER, respectively. The replacement of graphene with N-doped graphene produces the even more efficient $MoSe_2$/N-graphene/HfS_2. This is because the increased Fermi level of graphene after nitrogen doping reduces its work function from 4.35 to 3.61 eV and increases the density of states of electrons near the Fermi level, which promotes electron migration.

Compared to the conventional three-component Z-scheme heterostructures, a Z-scheme heterostructure without the use of a redox mediator was reported in ZnO-CdS heterostructure in 2009[240]. Formally named as a direct Z-scheme in 2010[129], the new design is easy to construct with two components. Due to the clean and controllable interface, 2D vdW heterostructures are promising candidates for direct Z-scheme photocatalysts. On the basis of the relative position of the partitioned band edges of the $MoSe_2$ and HfS_2 monolayers to the redox potential of H^+/H_2 and H_2O/O_2, the $MoSe_2$/HfS_2 heterostructure with a predicted strong internal electric field has proved to be an active direct Z-scheme photocatalyst for water splitting[239].

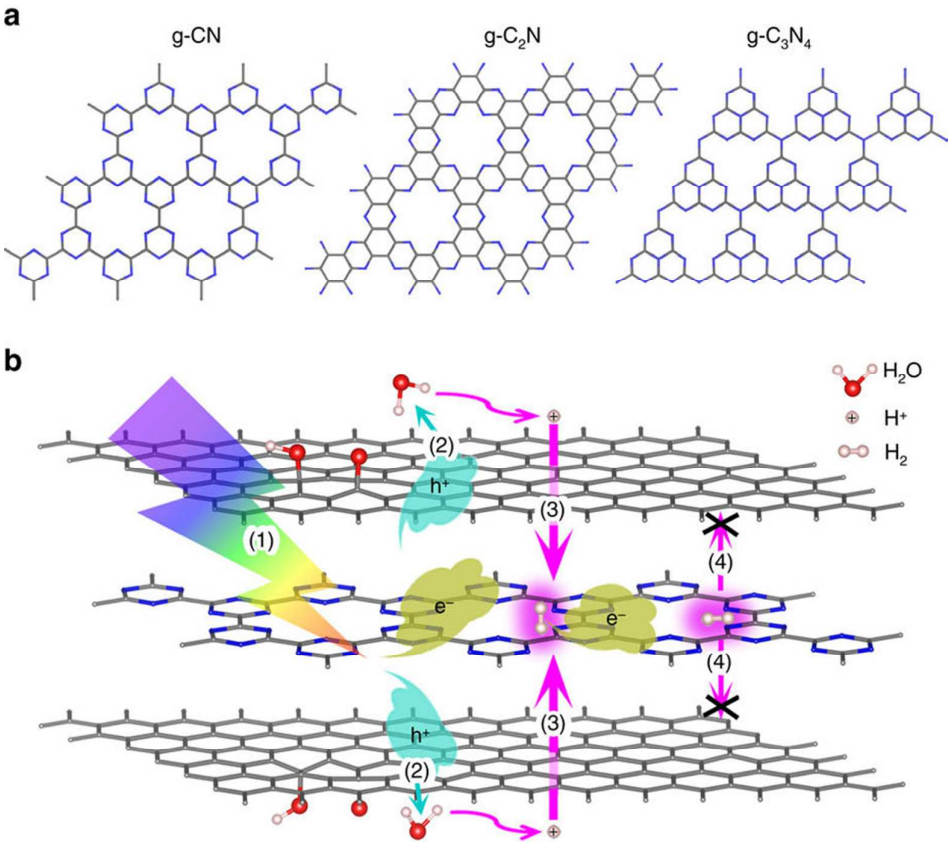

Figure 30. Scheme of water splitting and hydrogen capsuling scheme. (a) Models of graphitic carbon nitrides CN, C_2N, C_3N_4. (b) The photocatalytic (water splitting) hydrogen generation and capsule storage scheme: (1) photo-generated electrons (e^-) and holes (h^+) separating; (2) water splitting to produce protons (H^+) under attacking of holes (h^+); (3) protons (H^+) penetrating the GO and producing H_2 molecules; (4) H_2 molecules are prohibited from moving out of the sandwich. Here GO–CN–GO is used as an example. Blue, grey, pink and red beads respectively represent N, C, H (H^+) and O atoms, the yellow and light blue clouds are respectively photo-generated electrons (e^-) and holes (h^+), and the blue and magenta arrows indicate the migration of corresponding particles. Reproduced with permission from ref. 241. Copyright 2016, Springer Nature.

Different from the construction the vdW heterostructures of two monolayers for only photocatalysis, Yang *et al.*[241] proposed a dual function multi-layer structure, where carbon nitride is sandwiched between two graphene sheets modified by different functional groups (hydroxyl and epoxy groups), as shown in **Figure 30**. It was theoretically shown that this system can harvest light and deliver photo-generated holes from the inner carbon nitride layer to the outer graphene-based sheets for water splitting and proton generation. Driven by electrostatic attraction, protons penetrate the graphene to react with electrons on the inner carbon nitride to generate a hydrogen molecule, which is then stored at a high-density within the sandwich. Moreover, the bandgap of carbon nitride is also narrowed for wider visible light absorption, as a result of the interaction between carbon nitride and graphene. The spatial separation of the reductive and oxidative sites between the inner and outer layers suppresses the recombination of the photo-generated electrons and holes. The ability to integrate photocatalytic hydrogen generation and safe storage has made the sandwich system an exciting candidate for practical solar and hydrogen energy utilization. This study provides a new viewpoint in the development of highly efficient systems for the solar-driven generation and utilization of hydrogen.

Inspired by exciting theoretical predictions, increasing experimental effort has focused on 2D-based hybrid photocatalysts. One of the early studies is on layer-by-layer ordered nanohybrids prepared by self-assembly between oppositely charged nanosheets of a Zn-Cr-layered double hydroxide (Zn-Cr-LDH) and titanium oxide nanosheets[225]. The resultant nanohybrids consist of alternate Zn-Cr-LDH and

titanium oxide nanosheets as shown in **Figure 31**. The hybridization has a negligible influence on the crystal structure and electronic structure of the Zn-Cr-LDH. The transfer of photogenerated electrons from the Zn-Cr-LDH nanosheets to the neighboring titanium oxide nanosheets leads to the spatial separation of electrons and holes between them so that their recombination probability is greatly reduced. As a photocatalyst, the hybrid shows almost double the photocatalytic oxygen generation under visible light compared to the LDH layer. Considering the large number of charged metal oxide nanosheets that are available, there are many possibilities of producing layer heterostructures to increase photocatalytic activity.

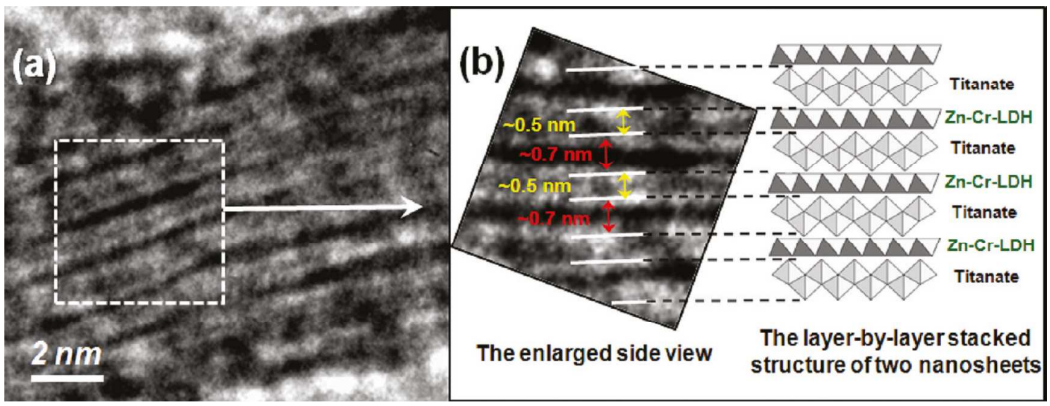

Figure 31. (a) Cross-sectional HR-TEM image of the ZCT-1 nanohybrid and (b) an enlarged view and structural model. Reproduced with permission from ref. 225. Copyright 2011, American Chemical Society.

Many 2D/2D vdW heterostructures containing graphitic carbon nitride nanosheets, with a high conduction band edge, and another 2D component (phosphorene, $Bi_4O_5I_2$,[227] LDH[234] and Fe_2O_3[103]) have been developed to control the transfer direction of the photo-generated charge carriers and their spatial separation between different

layers. The traditional transfer of the photogenerated electrons (holes) from a higher conduction (lower valence) band edge to a lower conduction (higher valence) band edge is proposed in the 2D/2D vdW heterostructures of SnS_2/g-C_3N_4,[242] g-C_3N_4/$Bi_4O_5I_2$[243], MoS_2/g-C_3N_4[226] and phosphorene or black P/g-C_3N_4[244, 245]. All these heterostructures show a higher photocatalytic activity than their individual components due to the increased charge separation. Different from common vdW heterostructures with weak interactions between the layers, Li *et al.* formed a novel bilayer junction by assembling metallic MoS_2 monolayers on the oxygen-deficient end-faces ($Bi_{12}O_{17}$) of $Bi_{12}O_{17}Cl_2$ semiconductor monolayers using oxygen-vacancy chemistry[91]. The bilayer has a photocatalytic hydrogen generation rate 38x that of the $Bi_{12}O_{17}Cl_2$ monolayers in an ascorbic acid solution under visible light. A good quantum efficiency of 36% at 420 nm was achieved on the bilayer sample. The Bi-S bonds formed between the $Bi_{12}O_{17}Cl_2$ monolayer with oxygen vacancies and the MoS_2 monolayer were shown to be the "high-speed" path for the transfer of photo-generated electrons from the former to the latter (**Figure 32**). The directional separation of the charge carriers between the layers is responsible for the greatly enhanced photocatalytic activity. The findings in this study can help us understand the commonly observed activity increase in the various reported 2D/2D heterostructures, where vacancies seem to be always present in the monolayers.

It is very encouraging to see recent progress on the formation of direct Z-scheme 2D/2D heterostructures for overall water splitting. For instance, She *et al.* demonstrated that a (0.1%) RuO_2/α-Fe_2O_3/g-C_3N_4/Pt (3%) Z-Scheme photocatalyst

consisting of ~15 nm thick Fe_2O_3 nanosheets and 1.1-1.4 nm thick g-C_3N_4 nanosheets has the ability to induce overall water splitting under visible light[103]. The tight interface between the nanosheets together with their appropriate band alignments is proposed to play a key role in causing the direct Z-scheme (**Figure 33a** and **b**). Polymer-based vdW heterostructures using aza-fused microporous polymers (CMP) and C_2N ultrathin nanosheets as HER and OER catalysts, respectively, have been designed as metal-free Z-scheme photocatalytic systems, to produce photocatalytic overall water splitting under visible light (**Figure 33c-e**)[246]. The heterostructure has an optimal STH conversion efficiency of 0.23%, which can be increased to 0.40% by using graphene as a solid intermediate to facilitate interfacial charge-transfer process. These two examples indicate the great potential of using polymers with a good flexibility to construct Z-scheme 2D heterostructures. A Z-scheme photocatalyst based on black phosphorus (BP)/$BiVO_4$ has also developed for visible light water splitting[233]. Using this material with a Co_3O_4 cocatalyst produces a molar ratio of hydrogen to oxygen evolved from pure water that depends on the ratio of phosphorous to $BiVO_4$. When the amount of BP reaches 40 wt%, a nearly stoichiometric H_2/O_2 ratio can be detected. The presence of the charge transfer path from the conduction band of BP to the valence band of $BiVO_4$ is confirmed by the shorter lifetime of the charge carriers in the heterostructure. All these results demonstrate the great potential of using 2D materials to construct direct Z-scheme heterostructures for overall water splitting. Besides the large tight interfacial contact between the materials, some other underlying factors like defects and local surface

structure changes may play an important role in inducing the Z-scheme and the important role of defects has been demonstrated in bulk heterostructures.

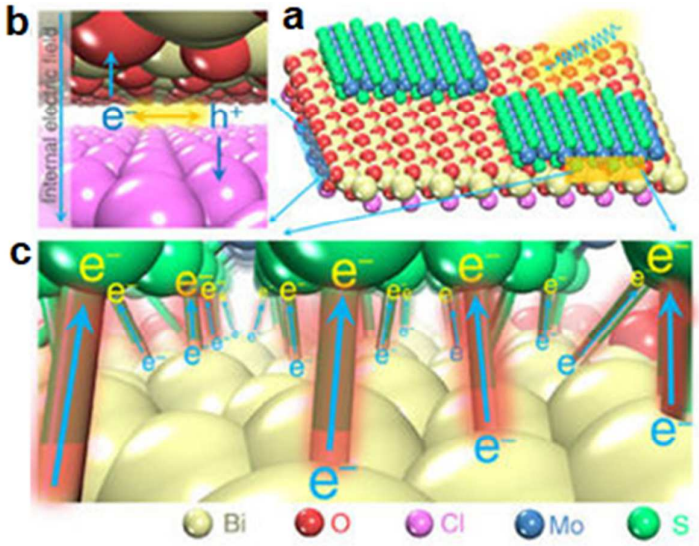

Figure 32. (a) Schematic of the crystal structure of $Bi_{12}O_{17}Cl_2$-MoS_2 (BOC-MS) and (b) of the charge flow processes within BOC-MS, including the electron–hole separation within 1L-BOC and (c) the interfacial electron transfer from 1L-BOC to 1L-MS along the Bi–S bonds. Reproduced with permission from ref. 91. Copyright 2016, Springer Nature.

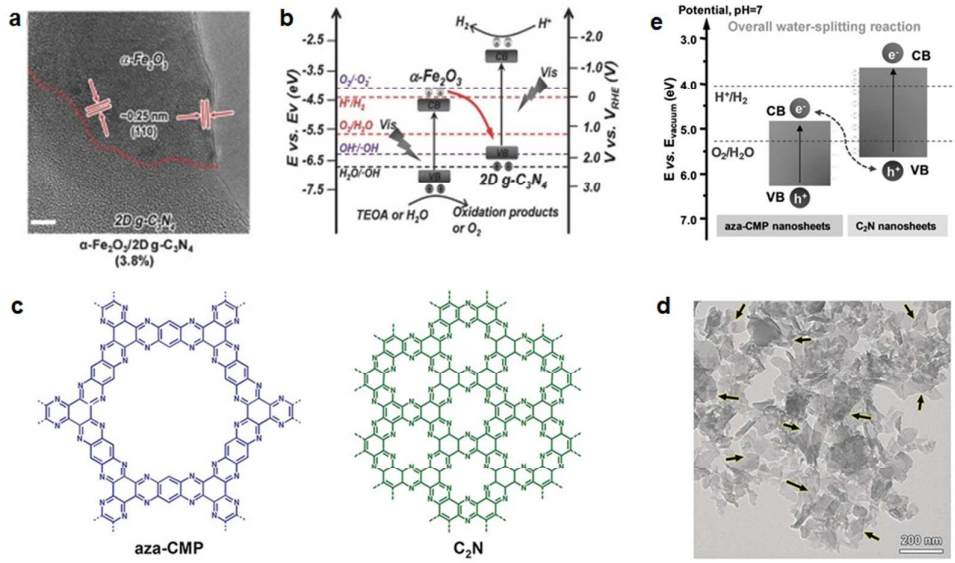

Figure 33. (a), HRTEM image of α-Fe_2O_3/2D g-C_3N_4 (3.8%) hybrid. Scale bar: 5 nm.

(b), Energy band diagram of the Z-scheme mechanism in α-Fe_2O_3/2D g-C_3N_4 (3.8%) hybrids at pH = 0. Reproduced with permission from ref. 103. Copyright 2017, John Wiley and Sons. **(c)**, Chemical structures of both aza-CMP and C_2N. **(d)**, TEM image of aza-CMP/C_2N heterostructures. Arrows indicate overlapping interfaces. **(e)**, Illustration of the electronic band structures of aza-CMP and C_2N nanosheets, resulting in a Z-scheme structure. Key: ① C_2N nanosheets, ② aza-CMP nanosheets. Reproduced with permission from ref. 246. Copyright 2018, John Wiley and Sons.

5. Concluding remarks and perspective

With the development of a huge number of 2D materials over the past decade, 2D material-based photocatalysts have attracted increasing attention with exciting new opportunities in the rational design and construction of highly efficient solar-driven photocatalysts. So far, most traditional bulk photocatalysts have been explored in the form of their 2D counterparts. Compared to the bulk photocatalysts, the 2D materials for solar fuel generation have exhibited many unusual physicochemical properties. Because of their large lateral size and ultrathin thickness they are considered as macromolecule-like photocatalysts and therefore bridge the gap between homogeneous molecular catalysts and heterogeneous photocatalysts, to some extent. The results obtained from 2D photocatalysts certainly provide valuable new understanding of the photocatalytic processes and reaction mechanisms, which should lead to innovative strategies and guidelines for the development of a new generation of photocatalysts. We believe that this might be more important than the 2D photocatalysts themselves. Nevertheless, there are still key issues about 2D

photocatalysts to be addressed.

What is the optimum thickness of the nanosheets for maximum photocatalytic activity? Apart from the noticeable success in synthesizing 2D photocatalysts with considerably improved photocatalytic activities, there is a trend to pursue 2D structural engineering to achieve a material that is as thin as possible. The apparently favorable features associated with such a thickness reduction include significantly increased specific surface areas for abundant reactive sites, a shorter diffusion length of photo-generated charge carriers from the inside to the surface, and an enlarged bandgap for higher energies of photogenerated charge carriers. However, the quantum confinement effect in ultrathin nanosheets can also narrow the light absorption range and probably increase the recombination of the photogenerated charge carriers because of the high binding energy of excitons. It is clear that there is a strong trade-off between the favorable and unfavorable features caused by a 2D structure. The question then arises as to whether the photocatalytic activity of 2D photocatalysts reaches an optimum at a certain thickness? Finding the answer to this question requires further exploration of a series of 2D materials with different thicknesses, which remains a challenge.

What is the underlying role of the strong interaction between 2D light absorbers and co-catalysts in affecting photocatalysis? As a result of the geometric features of ultrathin structures, the loading of co-catalysts on 2D nanosheets becomes much easier than on bulk or other shaped light absorbers. These co-catalysts usually have a particle size of several nanometers and can even be single atoms. The tight

interfacial contact between the co-catalysts and light absorber nanosheets normally facilitates charge transfer. For a bulk light absorber with a small surface-area to volume ratio, the influence of a surface co-catalyst on the electronic structure should be negligible. In contrast, the strong interaction between the co-catalyst and nanosheets with a large surface-area to volume ratio is so strong that the electronic structure of the nanosheets is modified. This is indicated by a recent study that some localized states have been introduced in the band gap of metal oxides by coating with an ultrathin amorphous boron oxynitride layer on the surface[136]. An understanding of this interaction might provide some useful guidelines for co-catalyst-modified 2D light absorbers.

Can we understand the correlation between structural changes in the nanosheets and their photocatalysis performance? The high flexibility of ultrathin nanosheets inevitably causes structural changes, including elastic strain as indicated by the crumpled morphology of free-standing nanosheets[184]. Strain-induced modification of electronic structures has been demonstrated experimentally and theoretically in some monolayer nanosheets. Intentionally using and even increasing this effect is desirable and may generate unanticipated photocatalytic activity increases. Although a strain-induced band structure modification has been recognized, its underlying role in changing the bonding structure to modulate the sorption of molecules/ions deserves further investigation.

How to rationally control the abundant defects of the nanosheets to boost the photocatalytic performance? The fabrication of artificial layer structures with the

ultrathin nanosheets of different materials as building blocks may open up a new door of creating some extraordinary properties. Many monolayer nanosheets have their surface atoms with the saturated coordination so that the interaction between the layers might be too weak to cause long-range interaction along the direction perpendicular to the nanosheets. Some reports have preliminarily demonstrated the feasibility of using surface defects to strengthen the interaction between layers by forming additional strong bonds in the layer galleries[91]. Controlling the defects of the nanosheets therefore represents an important aspect for fine-tuning the properties of 2D photocatalysts. Equally important, the rotation between layers in the restacked nanosheets might exert the influence on electronic structure of the resultant hybrid structures.

Being 2D cannot solve all the challenges that photocatalysis faces, but does provide new opportunities for understanding the principles or mechanisms of photocatalysis, and strengthens the ability to manipulate or change photocatalysts at the atomic level. Thanks to the ever increasing number of 2D materials available and their applications in many sectors including energy, the environment and bioengineering, we are confident that more exciting progress will be achieved in the photocatalytic solar energy conversion field in the near future.

Acknowledgements

Some studies covered in this paper are financially supported by the Major Basic Research Program, Ministry of Science and Technology of China (2014CB239401),

National Natural Science Foundation of China (Nos. 51572266, 51629201, 51422210, 51521091), and the Key Research Program of Frontier Sciences CAS (QYZDB-SSW-JSC039). G. L. is grateful for the award of a Newton Advanced Fellowship. Financial support from the Australian Research Council through its discovery and linkage project is also appreciated.

References

1. J. L. White, M. F. Baruch, J. E. Pander, III, Y. Hu, I. C. Fortmeyer, J. E. Park, T. Zhang, K. Liao, J. Gu, Y. Yan, T. W. Shaw, E. Abelev and A. B. Bocarsly, *Chem. Rev.*, 2015, **115**, 12888-12935.
2. A. Fujishima and K. Honda, *Nature*, 1972, **238**, 37-38.
3. Z. B. Chen, T. F. Jaramillo, T. G. Deutsch, A. Kleiman-Shwarsctein, A. J. Forman, N. Gaillard, R. Garland, K. Takanabe, C. Heske, M. Sunkara, E. W. McFarland, K. Domen, E. L. Miller, J. A. Turner, H. N. Dinh, *J. Mater. Res.*, 2010, **25**, 3-16.
4. Q. Wang, T. Hisatomi, Q. Jia, H. Tokudome, M. Zhong, C. Wang, Z. Pan, T. Takata, M. Nakabayashi, N. Shibata, Y. Li, I. D. Sharp, A. Kudo, T. Yamada and K. Domen, *Nat. Mater.*, 2016, **15**, 611-615.
5. Y. Sakata, T. Hayashi, R. Yasunaga, N. Yanaga and H. Imamura, *Chem. Commun.*, 2015, **51**, 12935-12938.
6. C. Pan, T. Takata, M. Nakabayashi, T. Matsumoto, N. Shibata, Y. Ikuhara and K. Domen, *Angew. Chem. Int. Ed.*, 2015, **54**, 2955-2959.
7. S. Chen, T. Takata and K. Domen, *Nat. Rev. Mater.*, 2017, **2**, 17050.
8. M. Xu, T. Liang, M. Shi and H. Chen, *Chem. Rev.*, 2013, **113**, 3766-3798.
9. C. Tan, X. Cao, X.-J. Wu, Q. He, J. Yang, X. Zhang, J. Chen, W. Zhao, S. Han, G.-H. Nam, M. Sindoro and H. Zhang, *Chem. Rev.*, 2017, **117**, 6225-6331.
10. M. Nasilowski, B. Mahler, E. Lhuillier, S. Ithurria and B. Dubertret, *Chem. Rev.*, 2016, **116**, 10934-10982.
11. Q. Wang and D. O'Hare, *Chem. Rev.*, 2012, **112**, 4124-4155.
12. M. Chhowalla, H. S. Shin, G. Eda, L.-J. Li, K. P. Loh and H. Zhang, *Nat. Chem.*, 2013, **5**, 263-275.
13. M. J. Kory, M. Woerle, T. Weber, P. Payamyar, S. W. van de Poll, J. Dshemuchadse, N. Trapp and A. D. Schlueter, *Nat. Chem.*, 2014, **6**, 779-784.

14. H. Duan, N. Yan, R. Yu, C.-R. Chang, G. Zhou, H.-S. Hu, H. Rong, Z. Niu, J. Mao, H. Asakura, T. Tanaka, P. J. Dyson, J. Li and Y. Li, *Nat. Commun.*, 2014, **5**, 3093.
15. F. Liu, L. You, K. L. Seyler, X. Li, P. Yu, J. Lin, X. Wang, J. Zhou, H. Wang, H. He, S. T. Pantelides, W. Zhou, P. Sharma, X. Xu, P. M. Ajayan, J. Wang and Z. Liu, *Nat. Commun.*, 2016, **7**, 12357.
16. A. J. Mannix, X.-F. Zhou, B. Kiraly, J. D. Wood, D. Alducin, B. D. Myers, X. Liu, B. L. Fisher, U. Santiago, J. R. Guest, M. J. Yacaman, A. Ponce, A. R. Oganov, M. C. Hersam and N. P. Guisinger, *Science*, 2015, **350**, 1513-1516.
17. V. Nicolosi, M. Chhowalla, M. G. Kanatzidis, M. S. Strano and J. N. Coleman, *Science*, 2013, **340**, 1420-1424.
18. S. Balendhran, S. Walia, H. Nili, S. Sriram and M. Bhaskaran, *Small*, 2015, **11**, 640-652.
19. A. Gupta, T. Sakthivel and S. Seal, *Prog. Mater. Sci.*, 2015, **73**, 44-126.
20. D. Deng, K. S. Novoselov, Q. Fu, N. Zheng, Z. Tian and X. Bao, *Nat. Nanotechnol.*, 2016, **11**, 218-230.
21. A. Pospischil, M. M. Furchi and T. Mueller, *Nat. Nanotechnol.*, 2014, **9**, 257-261.
22. F. Xia, H. Wang, D. Xiao, M. Dubey and A. Ramasubramaniam, *Nat. Photonics*, 2014, **8**, 899-907.
23. Z. A. Piazza, H.-S. Hu, W.-L. Li, Y.-F. Zhao, J. Li and L.-S. Wang, *Nat. Commun.*, 2014, **5**, 3113.
24. F. Song and X. Hu, *Nat. Commun.*, 2014, **5**, 4477.
25. Y. Sun, Q. Liu, S. Gao, H. Cheng, F. Lei, Z. Sun, Y. Jiang, H. Su, S. Wei and Y. Xie, *Nat. Commun.*, 2013, **4**, 2899.
26. M.-Q. Yang, Y.-J. Xu, W. Lu, K. Zeng, H. Zhu, Q.-H. Xu and G. W. Ho, *Nat. Commun.*, 2017, **8**, 14224.
27. J. Yao, K. J. Koski, W. Luo, J. J. Cha, L. Hu, D. Kong, V. K. Narasimhan, K. Huo and Y. Cui, *Nat. Commun.*, 2014, **5**, 5670.
28. F. Bonaccorso, L. Colombo, G. Yu, M. Stoller, V. Tozzini, A. C. Ferrari, R. S. Ruoff and V. Pellegrini, *Science*, 2015, **347**, 1246501.
29. M. P. Boneschanscher, W. H. Evers, J. J. Geuchies, T. Altantzis, B. Goris, F. T. Rabouw, S. A. P. van Rossum, H. S. J. van der Zant, L. D. A. Siebbeles, G. Van Tendeloo, I. Swart, J. Hilhorst, A. V. Petukhov, S. Bals and D. Vanmaekelbergh, *Science*, 2014, **344**, 1377-1380.
30. B. Hunt, J. D. Sanchez-Yamagishi, A. F. Young, M. Yankowitz, B. J. LeRoy, K. Watanabe, T. Taniguchi, P. Moon, M. Koshino, P. Jarillo-Herrero and R. C. Ashoori, *Science*, 2013, **340**, 1427-1430.
31. T. F. Jaramillo, K. P. Jorgensen, J. Bonde, J. H. Nielsen, S. Horch and I.

Chorkendorff, *Science*, 2007, **317**, 100-102.

32. Y. Li, Z. Li, C. Chi, H. Shan, L. Zheng and Z. Fang, *Adv. Sci.*, 2017, **4**, 1600430.
33. K. Li, Y. Wang, H. Wang, M. Zhu and H. Yan, *Nanotechnology*, 2006, **17**, 4863-4867.
34. L. Zhang, D. R. Chen and X. L. Jiao, *J. Phys. Chem. B*, 2006, **110**, 2668-2673.
35. G. Liu, L. Wang, C. Sun, Z. Chen, X. Yan, L. Cheng, H.-M. Cheng and G. Q. Lu, *Chem. Commun.*, 2009, 1383-1385.
36. Y. Matsumoto, M. Koinuma, Y. Iwanaga, T. Sato and S. Ida, *J. Am. Chem. Soc.*, 2009, **131**, 6644-6645.
37. Y. Okamoto, S. Ida, J. Hyodo, H. Hagiwara and T. Ishihara, *J. Am. Chem. Soc.*, 2011, **133**, 18034-18037.
38. S. Ida, Y. Okamoto, M. Matsuka, H. Hagiwara and T. Ishihara, *J. Am. Chem. Soc.*, 2012, **134**, 15773-15782.
39. F. Meng, Z. Hong, J. Arndt, M. Li, M. Zhi, F. Yang and N. Wu, *Nano Res.*, 2012, **5**, 213-221.
40. P. Niu, L. Zhang, G. Liu and H.-M. Cheng, *Adv. Funct. Mater.*, 2012, **22**, 4763-4770.
41. Y. Sun, H. Cheng, S. Gao, Z. Sun, Q. Liu, Q. Liu, F. Lei, T. Yao, J. He, S. Wei and Y. Xie, *Angew. Chem. Int. Ed.*, 2012, **51**, 8727-8731.
42. Y. Sun, Z. Sun, S. Gao, H. Cheng, Q. Liu, J. Piao, T. Yao, C. Wu, S. Hu, S. Wei and Y. Xie, *Nat. Commun.*, 2012, **3**, 1057.
43. M. R. Waller, T. K. Townsend, J. Zhao, E. M. Sabio, R. L. Chamousis, N. D. Browning and F. E. Osterloh, *Chem. Mater.*, 2012, **24**, 698-704.
44. Y. Fu, C. Chang, P. Chen, X. Chu and L. Zhu, *J. Hazard. Mater.*, 2013, **254**, 185-192.
45. M. Guan, C. Xiao, J. Zhang, S. Fan, R. An, Q. Cheng, J. Xie, M. Zhou, B. Ye and Y. Xie, *J. Am. Chem. Soc.*, 2013, **135**, 10411-10417.
46. Y. Hou, Z. Wen, S. Cui, X. Guo and J. Chen, *Adv. Mater.*, 2013, **25**, 6291-6297.
47. S. Ida, Y. Okamoto, S. Koga, H. Hagiwara and T. Ishihara, *RSC Adv.*, 2013, **3**, 11521-11524.
48. Y. Li, Y.-L. Li, C. M. Araujo, W. Luo and R. Ahuja, *Catal. Sci. Technol.*, 2013, **3**, 2214-2220.
49. Z. Lin and X. Wang, *Angew. Chem. Int. Ed.*, 2013, **52**, 1735-1738.
50. M. Sun, S. Xiong, X. Wu, C. He, T. Li and P. K. Chu, *Adv. Mater.*, 2013, **25**, 2035-2039.
51. Y. Wang, J. Hong, W. Zhang and R. Xu, *Catal. Sci. Technol.*, 2013, **3**, 1703-1711.

52. Q. Xiang and J. Yu, *J. Phys. Chem. Lett.*, 2013, **4**, 753-759.
53. J. Xu, L. Zhang, R. Shi and Y. Zhu, *J. Mater. Chem. A*, 2013, **1**, 14766-14772.
54. Y. Xu, W. Zhao, R. Xu, Y. Shi and B. Zhang, *Chem. Commun.*, 2013, **49**, 9803-9805.
55. S. Yang, Y. Gong, J. Zhang, L. Zhan, L. Ma, Z. Fang, R. Vajtai, X. Wang and P. M. Ajayan, *Adv. Mater.*, 2013, **25**, 2452-2456.
56. J. Zhu, Z. Yin, D. Yang, T. Sun, H. Yu, H. E. Hoster, H. H. Hng, H. Zhang and Q. Yan, *Energy Environ. Sci.*, 2013, **6**, 987-993.
57. F. Chang, C. Li, J. Chen, J. Wang, P. Luo, Y. Xie, B. Deng and X. Hu, *Superlattice Microst.*, 2014, **76**, 90-104.
58. J. Chen, M. Guan, W. Cai, J. Guo, C. Xiao and G. Zhang, *Phys. Chem. Chem.Phys.*, 2014, **16**, 20909-20914.
59. S. Gao, Y. Sun, F. Lei, J. Liu, L. Liang, T. Li, B. Pan, J. Zhou and Y. Xie, *Nano Energy*, 2014, **8**, 205-213.
60. J. Hong, S. Yin, Y. Pan, J. Han, T. Zhou and R. Xu, *Nanoscale*, 2014, **6**, 14984-14990.
61. Y. Hou, F. Zuo, A. P. Dagg, J. Liu and P. Feng, *Adv. Mater.*, 2014, **26**, 5043-5049.
62. F. Lei, Y. Sun, K. Liu, S. Gao, L. Liang, B. Pan and Y. Xie, *J. Am. Chem. Soc.*, 2014, **136**, 6826-6829.
63. L. Liang, Y. Sun, F. Lei, S. Gao and Y. Xie, *J.Mater. Chem. A*, 2014, **2**, 10647-10653.
64. J. Liu, X.-B. Li, D. Wang, H. Liu, P. Peng and L.-M. Liu, *J. Mater. Chem. A*, 2014, **2**, 6755-6761.
65. Q. Liu, D. Wu, Y. Zhou, H. Su, R. Wang, C. Zhang, S. Yan, M. Xiao and Z. Zou, *ACS Appl. Mater. Interfaces*, 2014, **6**, 2356-2361.
66. J. Low, S. Cao, J. Yu and S. Wageh, *Chem. Commun.*, 2014, **50**, 10768-10777.
67. K. Maeda, M. Eguchi and T. Oshima, *Angew. Chem. Int. Ed.*, 2014, **53**, 13164-13168.
68. B. Sa, Y.-L. Li, J. Qi, R. Ahuja and Z. Sun, *J. Phys. Chem. C*, 2014, **118**, 26560-26568.
69. K. Schwinghammer, M. B. Mesch, V. Duppel, C. Ziegler, J. Senker and B. V. Lotsch, *J. Am. Chem. Soc.*, 2014, **136**, 1730-1733.
70. Y. Sun, Z. Sun, S. Gao, H. Cheng, Q. Liu, F. Lei, S. Wei and Y. Xie, *Adv. Energy Mater.*, 2014, **4**, 1300611.
71. Y. Zhao, K. Yao, Q. Cai, Z. Shi, M. Sheng, H. Lin and M. Shao, *Crystengcomm*, 2014, **16**, 270-276.
72. D. Liu, Y. Lv, M. Zhang, Y. Liu, Y. Zhu, R. Zong and Y. Zhu, *J. Mater. Chem. A*, 2014, **2**, 15377-15388.

73. W. Bi, X. Li, L. Zhang, T. Jin, L. Zhang, Q. Zhang, Y. Luo, C. Wu and Y. Xie, *Nat. Commun.*, 2015, **6**, 8647.
74. X. Dang, X. Zhang, W. Zhang, X. Dong, G. Wang, C. Ma, X. Zhang, H. Ma and M. Xue, *RSC Adv.*, 2015, **5**, 15052-15058.
75. C. Huang, C. Chen, M. Zhang, L. Lin, X. Ye, S. Lin, M. Antonietti and X. Wang, *Nat. Commun.*, 2015, **6**, 7698.
76. Y. Ji, W. Guo, H. Chen, L. Zhang, S. Chen, M. Hua, Y. Long and Z. Chen, *J. Phys. Chem. C*, 2015, **119**, 27053-27059.
77. F. Lei, L. Zhang, Y. Sun, L. Liang, K. Liu, J. Xu, Q. Zhang, B. Pan, Y. Luo and Y. Xie, *Angew. Chem. Int. Ed.*, 2015, **54**, 9266-9270.
78. Q. Liang, Z. Li, Z.-H. Huang, F. Kang and Q.-H. Yang, *Adv. Funct. Mater.*, 2015, **25**, 6885-6892.
79. Q. Lin, L. Li, S. Liang, M. Liu, J. Bi and L. Wu, *Applied Catal. B: Environ.*, 2015, **163**, 135-142.
80. Y. Liu, J. Xiong, S. Luo, R. Liang, N. Qin, S. Liang and L. Wu, *Chem. Commun.*, 2015, **51**, 15125-15128.
81. Y. Lu, D. Chu, M. Zhu, Y. Du and P. Yang, *Phys. Chem. Chem.Phys.*, 2015, **17**, 17355-17361.
82. S. Park, H. J. Song, C. W. Lee, S. W. Hwang and I. S. Cho, *ACS Appl. Mater. Interfaces*, 2015, **7**, 21860-21867.
83. J. Ran, T. Y. Ma, G. Gao, X.-W. Du and S. Z. Qiao, *Energy Environ. Sci.*, 2015, **8**, 3708-3717.
84. Y. Xu, X. Yin, Y. Huang, P. Du and B. Zhang, *Chem. Eur. J.*, 2015, **21**, 4571-4575.
85. J. Zhang, Y. Chen and X. Wang, *Energy Environ. Sci.*, 2015, **8**, 3092-3108.
86. Z. Zhang, J. Huang, M. Zhang, L. Yuan and B. Dong, *Applied Catal. B: Environ.*, 2015, **163**, 298-305.
87. Y. Zheng, G. Chen, Y. Yu, Y. Hu, Y. Feng and J. Sun, *J. Mater. Sci.*, 2015, **50**, 8111-8119.
88. Y. Zhou, Y. Zhang, M. Lin, J. Long, Z. Zhang, H. Lin, J. C. S. Wu and X. Wang, *Nat. Commun.*, 2015, **6**, 8340.
89. M. Zhukovskyi, P. Tongying, H. Yashan, Y. Wang and M. Kuno, *ACS Catal.*, 2015, **5**, 6615-6623.
90. Y. Bai, T. Chen, P. Wang, L. Wang and L. Ye, *Chem. Eng. J.*, 2016, **304**, 454-460.
91. J. Li, G. Zhan, Y. Yu and L. Zhang, *Nat. Commun.*, 2016, **7**, 11480.
92. X. Li, W. Bi, L. Zhang, S. Tao, W. Chu, Q. Zhang, Y. Luo, C. Wu and Y. Xie, *Adv. Mater.*, 2016, **28**, 2427-2431.
93. X. Lu, K. Xu, S. Tao, Z. Shao, X. Peng, W. Bi, P. Chen, H. Ding, W. Chu, C.

Wu and Y. Xie, *Chem. Sci.*, 2016, **7**, 1462-1467.
94. Q. Wang, L. Yuan, M. Dun, X. Yang, H. Chen, J. Li and J. Hu, *Applied Catal. B: Environ.*, 2016, **196**, 127-134.
95. J. Xia, M. Ji, J. Di, B. Wang, S. Yin, Q. Zhang, M. He and H. Li, *Applied Catal. B: Environ.*, 2016, **191**, 235-245.
96. J. Xiong, Y. Liu, S. Liang, S. Zhang, Y. Li and L. Wu, *J. Catal.*, 2016, **342**, 98-104.
97. J. Yang, Y.-L. Jiang, L.-J. Li, E. Muhire and M.-Z. Gao, *Nanoscale*, 2016, **8**, 8170-8177.
98. W. Yang, L. Zhang, J. Xie, X. Zhang, Q. Liu, T. Yao, S. Wei, Q. Zhang and Y. Xie, *Angew. Chem. Int. Ed.*, 2016, **55**, 6716-6720.
99. L. Ye, X. Jin, C. Liu, C. Ding, H. Xie, K. H. Chu and P. K. Wong, *Applied Catal. B: Environ.* 2016, **187**, 281-290.
100. C. Zhou, Y. Zhao, L. Shang, R. Shi, L.-Z. Wu, C.-H. Tung and T. Zhang, *Chem. Commun.*, 2016, **52**, 8239-8242.
101. S. Gao, B. Gu, X. Jiao, Y. Sun, X. Zu, F. Yang, W. Zhu, C. Wang, Z. Feng, B. Ye and Y. Xie, *J. Am. Chem. Soc.*, 2017, **139**, 3438-3445.
102. Y. Li, Y.-L. Li, B. Sa and R. Ahuja, *Catal. Sci. Technol.*, 2017, **7**, 545-559.
103. X. She, J. Wu, H. Xu, J. Zhong, Y. Wang, Y. Song, K. Nie, Y. Liu, Y. Yang, M.-T. F. Rodrigues, R. Vajtai, J. Lou, D. Du, H. Li and P. M. Ajayan, *Adv. Energy Mater.*, 2017, **7**, 1700025.
104. J. Xia, M. Ji, J. Di, B. Wang, S. Yin, M. He, Q. Zhang and H. Li, *J. Alloy Compd.*, 2017, **695**, 922-930.
105. M. Zhou, X. W. Lou and Y. Xie, *Nano Today*, 2013, **8**, 598-618.
106. X. Dong and F. Cheng, *J. Mater. Chem. A*, 2015, **3**, 23642-23652.
107. B. Peng, P. K. Ang and K. P. Loh, *Nano Today*, 2015, **10**, 128-137.
108. B. Luo, G. Liu and L. Wang, *Nanoscale*, 2016, **8**, 6904-6920.
109. L. Mohapatra and K. Parida, *J. Mater. Chem. A*, 2016, **4**, 10744-10766.
110. Y. Zhang, L. Xie, Y. Zhou and L. Yin, *Prog. Chem.*, 2016, **28**, 1528-1540.
111. Y. Chen, G. Jia, Y. Hu, G. Fan, Y. H. Tsang, Z. Li and Z. Zou, *Sustainable Energy Fuels*, 2017, **1**, 1875-1898.
112. J. Di, J. Xia, H. Li and Z. Liu, *Nano Energy*, 2017, **35**, 79-91.
113. J. Li, H. Li, G. Zhan and L. Zhang, *Acc. Chem. Res.*, 2017, **50**, 112-121.
114. W.-J. Ong, *Front. Mater.*, 2017, **4**, 11.
115. W. Peng, Y. Li, F. Zhang, G. Zhang and X. Fan, *Ind. Eng. Chem. Res.*, 2017, **56**, 4611-4626.
116. J. Di, J. Xiong, H. Li and Z. Liu, *Adv. Mater.*, 2018, **30**, 1704740.
117. M. J. Wu, J. Z. Wu, J. Zhang, H. Chen, J. Z. Zhou, G. R. Qian, Z. P. Xu, Z. Du and Q. L. Rao, *Catal. Sci. Technol.*, 2018, **8**, 1207-1228.

118. A. L. Linsebigler, G. Q. Lu and J. T. Yates, *Chem. Rev.*, 1995, **95**, 735-758.
119. M. R. Hoffmann, S. T. Martin, W. Y. Choi and D. W. Bahnemann, *Chem. Rev.*, 1995, **95**, 69-96.
120. J. Kou, C. Lu, J. Wang, Y. Chen, Z. Xu and R. S. Varma, *Chem. Rev.*, 2017, **117**, 1445-1514.
121. Y. Ma, X. Wang, Y. Jia, X. Chen, H. Han and C. Li, *Chem. Rev.*, 2014, **114**, 9987-10043.
122. J. Schneider, M. Matsuoka, M. Takeuchi, J. Zhang, Y. Horiuchi, M. Anpo and D. W. Bahnemann, *Chem. Rev.*, 2014, **114**, 9919-9986.
123. X. Lang, X. Chen and J. Zhao, *Chem. Soc. Rev.*, 2014, **43**, 473-486.
124. G. Liu, P. Niu, L. Wang, G. Q. Lu and H.-M. Cheng, *Catal. Sci. Technol.*, 2011, **1**, 222-225.
125. G. Hautier, A. Miglio, G. Ceder, G. M. Rignanese and X. Gonze, *Nat. Commun.*, 2013, **4**, 2292.
126. Y. Q. Yang, G. Liu, J. TS Irvine and H. M. Cheng, *Adv. Mater.*, 2016, **28**, 5850-5856.
127. R. Li, F. Zhang, D. Wang, J. Yang, M. Li, J. Zhu, X. Zhou, H. Han and C. Li, *Nat. Commun.*, 2013, **4**, 1432.
128. R. Asahi, T. Morikawa, H. Irie and T. Ohwaki, *Chem. Rev.*, 2014, **114**, 9824-9852.
129. G. Liu, L. Wang, H. G. Yang, H.-M. Cheng and G. Q. Lu, *J. Mater. Chem.*, 2010, **20**, 831-843.
130. Z. G. Zou, J. H. Ye, K. Sayama and H. Arakawa, *Nature*, 2001, **414**, 625-627.
131. X. Chen, L. Liu, P. Y. Yu and S. S. Mao, *Science*, 2011, **331**, 746-750.
132. G. Liu, L. Wang, C. Sun, X. Yan, X. Wang, Z. Chen, S. C. Smith, H.-M. Cheng and G. Q. Lu, *Chem. Mater.*, 2009, **21**, 1266-1274.
133. G. Liu, P. Niu, C. H. Sun, S. C. Smith, Z. G. Chen, G. Q. Lu and H. M. Cheng, *J. Am. Chem. Soc.*, 2010, **132**, 11642-11648.
134. P. Niu, L. C. Yin, Y. Q. Yang, G. Liu and H. M. Cheng, *Adv. Mater.*, 2014, **26**, 8046-8052.
135. Y. Kang, Y. Yang, L. C. Yin, X. Kang, G. Liu and H. M. Cheng, *Adv. Mater.*, 2015, **27**, 4572-4577.
136. Z. B. Yu, X. Q. Chen, X. D. Kang, Y. P. Xie, H. Z. Zhu, S. L. Wang, S. Ullah, H. Ma, L. Z. Wang, G. Liu, X. L. Ma and H. M. Cheng, *Adv. Mater.*, 2018, **30**, 1706259.
137. A. Mukherji, R. Marschall, A. Tanksale, C. Sun, S. C. Smith, G. Q. Lu and L. Wang, *Adv. Funct. Mater.*, 2011, **21**, 126-132.
138. Y. Y. Kang, Y. Q. Yang, L. C. Yin, X. D. Kang, L. Z. Wang, G. Liu and H. M. Cheng, *Adv. Mater.*, 2016, **28**, 6471-6477.

139. H. Tada, T. Mitsui, T. Kiyonaga, T. Akita and K. Tanaka, *Nat. Mater.*, 2006, **5**, 782-786.
140. L. Thulin and J. Guerra, *Phys. Rev. B*, 2008, **77**, 195112.
141. G. Giorgi, J. I. Fujisawa, H. Segawa and K. Yamashita, *J. Phys. Chem. Lett.* 2013, **4**, 4213-4216.
142. Z. Zhang and J. T. Yates, Jr., *Chem. Rev.*, 2012, **112**, 5520-5551.
143. G. Liu, H. G. Yang, J. Pan, Y. Q. Yang, G. Q. Lu and H.-M. Cheng, *Chem. Rev.*, 2014, **114**, 9559-9612.
144. L. C. Mu, Y. Zhao, A. L. Li, S. Y. Wang, Z. L. Wang, J. X. Yang, Y. Wang, T. F. Liu, R. T. Chen, J. Zhu, F. T. Fan, R. G. Li and C. Li, *Energy Environ. Sci*., 2016, **9**, 2463.
145. C. Zhen, J. C. Yu, G. Liu and H. M. Cheng, *Chem. Commun.*, 2014, **50**, 10416-10419.
146. Y. Matsumoto, S. Ida and T. Inoue, *J. Phys. Chem. C*, 2008, **112**, 11614-11616.
147. H. G. Yang, C. H. Sun, S. Z. Qiao, J. Zou, G. Liu, S. C. Smith, H. M. Cheng and G. Q. Lu, *Nature*, 2008, **453**, 638-641.
148. R. Dingle, *Festkörperprobleme*, 1975, **15**, 21-48.
149. A. D. Yoffe, *Adv. Phys*., 1993, **42**, 173-262
150. P.G. Harper and J.A. Hilder, *Phys. Stat. Sol.,*1968*,* **26**, 69-76.
151. V.B. Sandomirskii.*Soy.Phys. JETP*, 1967, **25**, 101.
152. W. E. Buhro and V. L. Colvin, *Nat. Mater.* 2003, 2, 138-139.
153. S. Ithurria, M. D. Tessier, B. Mahler, R. P. S. M. Lobo, B. Dubertret and A. L. Efros, *Nat. Mater.*, 2011, **10**, 936-941.
154. F. A. Frame and F. E. Osterloh, *J. Phys. Chem. C,* 2010, **114**, 10628-10633.
155. J. Zhao, M. A. Holmes and F. E. Osterloh, *ACS Nano*, 2013, **7**, 4316-4325.
156. K. F. Mak, C. Lee, J. Hone, J. Shan and T. F. Heinz, *Phys. Rev. Lett.*, 2010, **105**. 136805.
157. A. Splendiani, L. Sun, Y. B. Zhang, T. S. Li, J. Kim, C. Y. Chim, G. Galli and F. Wang, *Nano Lett*., 2010, **10**, 1271-1275.
158. Y. Sun, H. Cheng, S. Gao, Z. Sun, Q. Liu, Q. Liu, F. Lei, T. Yao, J. He, S. Wei and Y. Xie, *Angew. Chem., Int. Ed*., 2012, **51**, 8727-8731.
159. Y. Sun, Z. Sun, S. Gao, H. Cheng, Q. Liu, J. Piao, T. Yao, C. Wu, S. Hu, S. Wei and Y. Xie, *Nat. Commun.*, 2012, **3**, 1057.
160. X. D. Zhang, X. Xie, H. Wang, J. J. Zhang, B. C. Pan, and Y. Xie, *J. Am. Chem. Soc.*, 2013, **135**, 18-21.
161. L. Liang, F. Lei, S. Gao, Y. Sun, X. Jiao, J. Wu, S. Qamar and Y. Xie, *Angew. Chem., Int. Ed.*, 2015, **54**, 13971-13974.
162. H. Fang, H. A. Bechtel, E. Plis, M. C. Martin, S. Krishna, E. Yablonovitch and A. Javey, *Proc. Natl. Acad. Sci. U S A*, 2013, **110**, 11688-11691.

163. O. C. Compton, E. C. Carroll, J. Y. Kim, D. S. Larsen and F. E. Osterloh, *J. Phys. Chem. C*, 2007, **111**, 14589-14592.
164. Y. Ebina, T. Sasaki, M. Harada and M. Watanabe, *Chem. Mater.*, 2002, **14**, 4390-4395.
165. X. Wang, K. Maeda, A. Thomas, K. Takanabe, G. Xin, J. M. Carlsson, K. Domen and M. Antonietti, *Nat. Mater.*, 2009, **8**, 76-80.
166. B. Seger, J. McCray, A. Mukherji, X. Zong, Z. Xing and L. Wang, *Angew. Chem., Int. Ed.*, 2013, **52**, 6400-6403.
167. G. Liu, C. Sun, L. Wang, S. C. Smith, G. Q. Lu and H.-M. Cheng, *J. Mater. Chem.*, 2011, **21**, 14672-14679.
168. Q. H. Weng, Y. Ide, X. B. Wang, X. Wang, C. Zhang, X. F. Jiang, Y. M. Xue, P. C. Dai, K. Komaguchi, Y. Bando and D. Golberg, *Nano Energy*, 2015, **16**, 19-27.
169. J. M. Lee, H. B. Jin, I. Y. Kim, Y. K. Jo, J.-W. Hwang, K.-K. Wang, M. G. Kim, Y.-R. Kim, and S.-J. Hwang, *Small*, 2015, **11**, 5771-5780.
170. I. Y. Kim, J. M. Lee, T. W. Kim, H. N. Kim, H.-I. Kim, W. Choi, and S.-J Hwang, Small, 2012, 8, 1038-1048.
171. S. Park, J. M. Lee, Y. K. Jo, I. Y. Kim and S.-J. Hwang, *Dalton Trans*., 2014, **43**, 10566–10573.
172. J. M. Lee, E. K. Mok, S. Lee, N.-S. Lee, L. Debbichi, H. Kim, and S.-J. Hwang, *Angew. Chem. Int. Ed.*, 2016, **55**, 8546 –8550.
173. J. Yang, D. Wang, H. Han and C. Li, *Acc. Chem. Res.*, 2013, **46**, 1900-1909.
174. J. Ran, J. Zhang, J. Yu, M. Jaroniec and S. Z. Qiao, *Chem. Soc. Rev.*, 2014, **43**, 7787-7812.
175. B. Qiao, A. Wang, X. Yang, L. F. Allard, Z. Jiang, Y. Cui, J. Liu, J. Li and T. Zhang, *Nat. Chem.*, 2011, **3**, 634-641.
176. Y. Li, Z. Wang, T. Xia, H. Ju, K. Zhang, R. Long, Q. Xu, C. Wang, L. Song, J. Zhu, J. Jiang and Y. Xiong, *Adv. Mater.*, 2016, **28**, 6959-6965.
177. G. Gao, Y. Jiao, E. R. Waclawik and A. Du, *J. Am. Chem. Soc.*, 2016, **138**, 6292-6297.
178. S. Bertolazzi, J. Brivio and A. Kis, *ACS Nano* 2011, **5**, 9703–9709.
179. J. Feng, X. Qian, C.-W. Huang and J. Li, *Nat. Photonics*, 2012, **6**, 865-871.
180. H. J. Conley, B. Wang, J. I. Ziegler, R. F. Haglund, Jr., S. T. Pantelides and K. I. Bolotin, *Nano Lett.*, 2013, **13**, 3626-3630.
181. A. S. Rodin, A. Carvalho and A. H. Castro Neto, *Phys. Rev. Lett.*, 2014, **112**, 176801.
182. X. Peng, Q. Wei and A. Copple, *Phys. Rev. B*, 2014, **90**, 085402.
183. M. Elahi, K. Khaliji, S. M. Tabatabaei, M. Pourfath and R. Asgari, *Phys. Rev. B*, 2015, **91**, 115412.

184. S. L. Wang, X. Luo, X. Zhou, Y. Zhu, X. Chi, W. Chen, K. Wu, Z. Liu, S. Y. Quek and G. Q. Xu. *J. Am. Chem. Soc.* 2017, **139**, 15414−15419.
185. W.-J. Ong, L.-L. Tan, Y. H. Ng, S.-T. Yong and S.-P. Chai, *Chem. Rev.*, 2016, **116**, 7159-7329.
186. Y. Zheng, L. Lin, B. Wang and X. Wang, *Angew. Chem., Int. Ed.*, 2015, **54**, 12868-12884.
187. Y. Chen, B. Wang, S. Lin, Y. Zhang and X. Wang, *J. Phys. Chem. C*, 2014, **118**, 29981-29989.
188. H. Wang, X. Zhang, J. Xie, J. Zhang, P. Ma, B. Pan and Y. Xie, *Nanoscale*, 2015, **7**, 5152-5156.
189. H. Yin and Z. Tang, *Chem. Soc. Rev.*, 2016, **45**, 4873-4891.
190. Y. Sun, S. Gao, F. Lei and Y. Xie, *Chem. Soc. Rev.*, 2015, **44**, 623-636.
191. Y. Zhao, B. Li, Q. Wang, W. Gao, C. J. Wang, M. Wei, D. G. Evans, X. Duan and D. O'Hare, *Chem. Sci.*, 2014, **5**, 951-958.
192. S. Ida, *Bull. Chem. Soc. Jpn*, 2015, **88**, 1619-1628.
193. L. Wang and M. Zhou, *New Chem. Mater.*, 2017, **45**, 30-32.
194. T. Sasaki, M. Watanabe, H. Hashizume, H. Yamada and H. Nakazawa, *J. .Am. Chem. Soc.*, 1996, **118**, 8329-8335.
195. N. Sakai, Y. Ebina, K. Takada and T. Sasaki, *J. .Am. Chem. Soc.*, 2004, **126**, 5851-5858.
196. L. Wang and T. Sasaki, *Chem. Rev.*, 2014, **114**, 9455-9486.
197. H. Sato, K. Ono, T. Sasaki and A. Yamagishi, *J. Phys. Chem. B*, 2003, **107**, 9824-9828.
198. R. Ma and T. Sasaki, *Adv. Mater.*, 2010, **22**, 5082-5104.
199. K. Akatsuka, G. Takanashi, Y. Ebina, M. Haga, and T. Sasaki, *J. Phys. Chem. C,* 2012, **116**, 12426-12433.
200. P. T. Xu, T. J. Milstein and T. E. Mallouk, *ACS Appl. Mater. Interfaces,* 2016, **8**, 11539−11547.
201. E. M. Sabio, R. L. Chamousis, N. D. Browning and F. E. Osterloh, *J. Phys. Chem. C* 2012, **116**, 3161−3170.
202. O. C. Compton, C. H. Mullet, S. Chiang and F. E. Osterloh, *J. Phys. Chem. C* 2008, **112***,* 6202-6208.
203. O. C. Compton and F. E. Osterloh, *J. Phys. Chem. C*, 2009, **113**, 479-485.
204. Y. Ebina, N. Sakai and T. Sasaki, *J. Phys. Chem. B* 2005, **109**, 17212-17216.
205. T. Oshima, D. Lu, O. Ishitani and K. Maeda, *Angew. Chem. Int. Ed.*, 2015, **54**, 2698-2702.
206. T. G. Xu, C. Zhang, X. Shao, K. Wu and Y. F. Zhu, *Adv. Funct. Mater.*, 2006, **16**, 1599–1607.
207. E. J. W. Crossland, N. Noel, V. Sivaram, T. Leijtens, J. A. Alexander-Webber

and H. J. Snaith, *Nature*, 2013, **495**, 215-219.

208. T. T. Wu, X. D. Kang, M. W. Kadi, I. Ismail, G. Liu and H. M. Cheng, *Chin. J. Catal.*, 2015, **36**, 2103–2108.
209. C. Zhen, T. T. Wu, M. W. Kadi, I. Ismail, G. Liu, H. M. Cheng, *Chin. J. Catal.*, 2015, **36**, 2171–2177.
210. C. W. Wang, S. Yang, W. Q. Fang, P. Liu, H. J. Zhao and H. G. Yang, *Nano Lett.*, 2016, **16**, 427-433.
211. F. X. Zhang, A. Yamakata, K. Maeda, Y. Moriya, T. Takata, J. Kubota, K. Teshima, S. Oishi and K. Domen, *J. Am. Chem. Soc.*, 2012, **134**, 8348–8351.
212. Z. H. Ren, R. Y. Zhao, X. Chen, M. Li, X. Li, H. Tian, Z. Zhang and G. R. Han, *Nat. Commun.* 2018, **9**, 1638.
213. T. Butburee, Y. Bai, H. J. Wang, H. J. Chen, Z. L. Wang, G. Liu, J. Zou, P. Khemthong, G. Q. Lu and L. Z. Wang, *Adv. Mater.*, 2018, **30**, 1705666.
214. J. Liu, Z. Y. Hu, Y. Peng, H. W. Huang, Y. Li, M. Wu, X. X. Ke, G. V. Tendeloo and B.-L. Su, *Applied Catal. B: Environ*., 2016, **181**, 138–145.
215. D. Krepel, L. Kalikhman-Razvozov and O. Hod, *J. Phys. Chem. C* 2014, **118**, 21110-21118.
216. D. Liu, M.W. Zhang, W.J. Xie, L Sun, Y Chen, W. W. Lei, *Applied Catal. B: Environ*., 2017, **207**, 72-78.
217. H. Chen, G. Yu, G. D. Li, T. F. Xie, Y Sun, J. Liu, H. Li, X. Huang, D. J. Wang, T. Asefa, W. Chen and X. X. Zou, *Angew. Chem. Int. Ed.*, 2016, **55**, 11442-11446.
218. M. Xiao, B. Luo, M. Q. Lyu, S. C. Wang and L. Z. Wang, *Adv. Energy Mater.*, 2018, **8**, 1701605.
219. M. L. Lv, X. Q. Sun, S. H. Wei, C. Shen, Y. L. Mi and X. X. Xu, *ACS Nano*, 2017, **11**, 11441-11448.
220. Q. Han, C. Hu, F. Zhao, Z. Zhang, N. Chen and L. Qu, *J. Mater. Chem. A*, 2015, **3**, 4612-4619.
221. J. Zhang, X. Chen, K. Takanabe, K. Maeda, K. Domen, J. D. Epping, X. Fu, M. Antonietti and X. Wang, *Angew. Chem. Int. Ed.*, 2010, **49**, 441-444.
222. S. Ida, N. Kim, E. Ertekin, S. Takenaka and T. Ishihara, *J. Am. Chem. Soc.*, 2015, **137**, 239-244.
223. J. Xie, H. Zhang, S. Li, R. Wang, X. Sun, M. Zhou, J. Zhou, X. W. Lou and Y. Xie, *Adv. Mater.*, 2013, **25**, 5807-5813.
224. W. Bi, C. Ye, C. Xiao, W. Tong, X. Zhang, W. Shao and Y. Xie, *Small*, 2014, **10**, 2820-2825.
225. J. L. Gunjakar, T. W. Kim, H. N. Kim, I. Y. Kim and S. J. Hwang, *J. Am. Chem. Soc.*, 2011, **133**, 14998-15007.
226. Y. Hou, A. B. Laursen, J. Zhang, G. Zhang, Y. Zhu, X. Wang, S. Dahl and I.

Chorkendorff, *Angew. Chem. Int. Ed.*, 2013, **52**, 3621-3625.

227. N. Tian, Y. Zhang, C. Liu, S. Yu, M. Li and H. Huang, *RSC Adv.*, 2016, **6**, 10895-10903.
228. J. Yan, Z. Chen, H. Ji, Z. Liu, X. Wang, Y. Xu, X. She, L. Huang, L. Xu, H. Xu and H. Li, *Chem. Eur. J.*, 2016, **22**, 4764-4773.
229. D. Yuan, L. Huang, Y. Li, Y. Xu, H. Xu, S. Huang, J. Yan, M. He and H. Li, *RSC Adv.*, 2016, **6**, 41204-41213.
230. Y. J. Yuan, Z.-J. Ye, H.-W. Lu, B. Hu, Y. H. Li, D.-Q. Chen, J.-S. Zhong, Z.-T. Yu and Z.-G. Zou, *ACS Catal.*, 2016, **6**, 532-541.
231. X. Zhang, Z. Meng, D. Rao, Y. Wang, Q. Shi, Y. Liu, H. Wu, K. Deng, H. Liu and R. Lu, *Energy Environ. Sci.*, 2016, **9**, 841-849.
232. Z. Zhang, K. Liu, Z. Feng, Y. Bao and B. Dong, *Scientific Reports*, 2016, **6,** 19221.
233. M. Zhu, Z. Sun, M. Fujitsuka and T. Majima, *Angew. Chem. Int. Ed.*, 2018, 57, 2160-2164.
234. S. Tonda, S. Kumar, M. Bhardwaj, P. Yadav and S. Ogale, *ACS Appl. Mater. Interfaces*, 2018, 10, 2667-2678.
235. A. K. Geim and I. V. Grigorieva, *Nature*, 2013, **499**, 419-425.
236. J. Liao, B. Sa, J. Zhou, R. Ahuja and Z. Sun, *J. Phys. Chem. C*, 2014, **118**, 17594-17599.
237. F. Wu, Y. Liu, G. Yu, D. Shen, Y. Wang and E. Kan, *J. Phys. Chem. Lett.*, 2012, **3**, 3330-3334.
238. X. X. Li, Z. Y. Li and J. L. Yang, *Phys. Rev. Lett.*, 2014, **112**, 018301.
239. C. F. Fu, Q. Q. Luo, X. X. Li and J. L. Yang, *J. Mater. Chem. A* 2016, **4**, 18892-18898.
240. X. W. Wang, G. Liu, Z. G. Chen, F. Li, L. Z. Wang, G. Q. Lu and H. M. Cheng, *Chem. Commun.,* 2009, 3452-3454.
241. L. Yang, X. Y. Li, G. Z. Zhang, P. Cui, X. J. Wang, X. Jiang, J. Zhao, Y. Luo and J. Jiang, *Nat. Commun.*, 2018, 8, 16049.
242. Z. Zhang, J. Huang, M. Zhang, Q. Yuan and B. Dong, *Applied Catal. B: Environ.*, 2015, **163**, 298-305.
243. Y. Bai, L. Ye, L. Wang, X. Shi, P. Wang, W. Bai and P. K. Wong, *Applied Catal. B: Environ.*, 2016, **194**, 98-104.
244. J. Ran, W. W. Guo, H. L. Wang, B. Zhu, J. Yu and S. Z. Qiao, *Adv. Mater.*, 2018, **30**, 1800128.
245. M. Zhu, S. Kim, L. Mao, M. Fujitsuka, J. Zhang, X. C. Wang and T. Majima, *J. Am. Chem. Soc.* 2017, **139**, 13234−13242.
246. L. Wang, X. S. Zheng, L. Chen, Y. J. Xiong and H. X. Xu, *Angew. Chem. Int. Ed.*, 2018, **57**, 3454-3458.

Authors' short bios

Gang Liu received his Bachelor degree in Materials Physics in Jilin University in 2003. He obtained his PhD degree in Materials Science at Institute of Metal Research (IMR), Chinese Academy of Sciences (CAS) in 2009. During his Ph. D study, he worked at Prof. G. Q. Max Lu's laboratory for one and half years in Australia. He was the recipient of the T.S. Kê RESEARCH FELLOPSHIP founded by Shenyang National Laboratory for Materials Science, IMR CAS. Now he is a professor of materials science in IMR. His main research interests focus on solar-driven photocatalyitc materials for renewable energy.

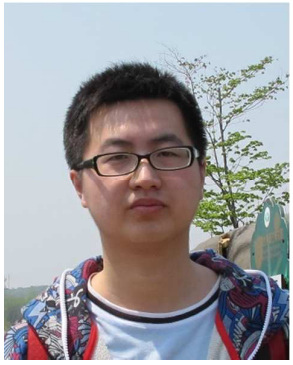

Chao Zhen received his Bachelor degree in Materials Physics from Jilin University in 2007. He obtained his PhD degree in Materials Science from Institute of Metal Research (IMR), Chinese Academy of Sciences in 2013. He worked as an assistant professor of materials in IMR between 2013 and 2015, and now he is an associate professor of materials science in IMR. His current research interest is developing efficient solar energy conversion devices including photoelectrochemical water splitting cells and new types of photovoltaic cells.

Yuyang Kang received his Bachelor degree in Materials Chemistry from Liaoning University in 2013. Now he is a Ph.D. candidate in Institute of Metal Research, Chinese Academy of Sciences. His research is focusing on layered photocatalysts for water splitting under the supervision of Professor Gang Liu and Professor Hui-Ming Cheng.

Lianzhou Wang is Professor at School of Chemical Engineering and Director of Nanomaterials Centre, the University of Queensland (UQ), Australia. He received his PhD degree from Chinese Academy of Sciences in 1999. Before joining UQ in 2004, he has worked at two national institutes (NIMS and AIST) of Japan for five years. Wang's research interests include the design and application of semiconducting nanomaterials in renewable energy conversion/storage systems, including photocatalysts and photoelectrochemical devices.

Hui-Ming Cheng is Professor and Director of the Advanced Carbon Research Division of Shenyang National Laboratory for Materials Science, Institute of Metal

Research, CAS, and the Low-Dimensional Material and Device Laboratory of the Tsinghua-Berkeley Shenzhen Institute, Tsinghua University. His research focuses on carbon nanotubes, graphene, two-dimensional materials, energy storage materials, photocatalytic semiconducting materials, and bulk carbon materials. He is a Highly Cited Researcher in materials science and chemistry fields. He is now the founding Editor-in-Chief of Energy Storage Materials and Associate Editor of Science China Materials. He was elected a member of CAS and a fellow of TWAS.